Mesoscale Assemblies of Inorganic Nanoparticles for Theranostic Applications

UNIVERSITÀ DEGLI STUDI
DI GENOVA

Sahitya Kumar Avugadda

ISTITUTO ITALIANO DI TECNOLOGIA

UNIVERSITÀ DEGLI STUDI DI GENOVA

Mesoscale Assemblies of Inorganic Nanoparticles for Theranostic Applications

Sahitya Kumar Avugadda
University of Genova
Italian Institute of Technology

Supervisor
Dr. Teresa Pellegrino
Italian Institute of Technology
Co-supervisor
Prof. Orietta.Monticelli
University of Genova

Submitted to fulfill the requirement for the Degree of Doctor of Philosophy in curricula, Nanochemistry, the school of Sciences and Technologies of Chemistry and Materials, University of Genova.

Doctorate Thesis 2020

Declaration

This dissertation is the result of my own work and includes nothing, which is the outcome of work done in collaboration except where specifically indicated in the text. It has not been submitted, in part or completely, to any university or institution of any degree, diploma, or other qualification.

DATE:

19th of March 2020

Sahitya Kumar Avugadda

Thesis Abstract

During the three years of my Ph.D, Ph.D cycle XXXII (2016-2019), at the Fondazione Istituto Italiano di Tecnologia, under the supervision of Dr.Teresa Pellegrino and the co-supervision of Prof.Orietta Monticelli (University of Genova), my focus was mainly on developing colloidally stable nanoclusters assembled at well-defined geometries produced from benchmark iron oxide nanocubes. These nanoclusters were designed, exploited and characterized for their potential use in theranostic applications comprising their exploitation in Magnetic Hyperthermia, Magnetic Resonance Imaging (MRI) and Magnetic Nanoparticles Imaging.

As the first aim, my focus was on building a two-dimensional nanoplatform based on highly efficient iron oxide nanocubes enwrapped with a bacteria extracted, biodegradable and biocompatible polyhydroxyalkanoate copolymer. Moreover, these magnetic polymeric clusters exhibit the unique feature to disassemble upon exposure to an intracellular rich lytic enzyme solution thus providing a gradual change in the cluster configuration accompanied by a gradual increase of magnetic heat performances in comparison to the initial 2D-clusters and to the individual iron oxide nanocubes used as building blocks for the cluster preparation. Indeed, comparing magnetic heat properties of the 2D assemblies with three dimensional centro-symmetrical assemblies (3D-MNBs) or single iron oxide nanocubes from same batch of cubes, emphasize how the initial 2D-assembly of iron oxide nanocubes s (2D-MNBs) dispersed in water are more advanced than the 3D-assemblies, but worse with respect to individual nanocubes. In addition, the heat abilities of these 2D clusters progressively increased when incubated in presence of esterase enzyme under physiological temperature, after 3 hours of incubation the specific absorption rate values, a measure of the heat-ability of the nanoparticles under a radio frequency were almost double than that of single cubes. Such an increase corresponds to disassembling of 2D-MNBs into short chain-like clusters of few nanocubes. Remarkably, our 2D-MNBs did not exhibit any variations in heat performance even after inducing an intentional aggregation. This is not the case for individual nanocubes. Magnetophoresis measurements suggest a faster response of 3D and 2D clusters to external magnets (0.3T) than that of individual nanocubes. This feature is desirable for the physical accumulation of magnetic materials under external magnetic field gradients. To the best of our knowledge, this is the first example of a

nanoplatform, which combined enzymatic cleavable properties to a clear enhancement of the magnetic heat losses. In addition to this cluster study, I have also contributed to characterize other chain-like assemblies, named Dimer/Trimer obtained by assembling low interacting core-shell of wustite/magnetite iron oxide nanocubes into an amphiphilic copolymer, poly(styrene-co-maleic anhydride) cumene-terminated. Interestingly, by modulating the amount of polymer to nanoparticle surface ratio, the geometry of the same clusters could be modulated from a single structure to Dimer/Trimer to centrosymmetric structures. The short chains of nanocubes exhibit even in this case an enhanced specific absorption rate value with respect to single cubes and centrosymmetric clusters. Overall these studies reveal the significance of particle arrangement as a means to improve magnetic heating performances of the same building blocks, the nanocubes in our case.

According to our second aim, the above nanoclusters (developed for magnetic hyperthermia mentioned) were investigated as magnetic tracers, to unveil their diagnostic features for, recently emerging magnetic nanoparticles imaging (MPI) and for Magnetic resonance imaging (MRI). The multimodal imaging models with combined MPI and MRI properties could assist in real-time mapping of tissues that expected to improve the diagnostic accuracy. We found that the 2D-MNBs based on high interacting Iron oxide nanocubes exhibit poor MPI signal than that of standard Resovist. However, this signal of 2D-MNBs underwent a progressive increase upon incubation with esterase enzyme under physiological temperature (almost doubled) starting from their initial state, which attributes to the splitting of 2D beads into a small chain-like configuration. These results show a similar trend to the enzymatic triggered increase in heat performance, as mentioned above. Moreover, the 2D-MNBs possess a remarkable transverse relaxation rate (r_2), indicating an efficient negative contrast of 2D-MNBs as agents for MRI. This value reduced by half upon exposure to lytic enzyme providing a significant T_2-signal change upon to a stimulus triggered change (the enzymatic degradation). On the other side, among the nanoclusters based on core-shell iron oxide nanocubes; single structure, Dimer/Trimer to centrosymmetric structures, Dimer/Trimer exhibit a very remarkable MPI signal in comparison to the nanocube assemblies and to the individual nanoparticles and with respect to Resovist the most accepted FDA approved standard. Complementing the signal dominance in short chains of 2D-MNBs, the increase of MPI signal in Dimer/Trimer can also corresponds to their short uniaxial configuration. In addition, they have given a very significant

transverse relaxation rate (r_2) than many other superparamagnetic iron oxide nanoparticles. This kind of nanovectors with multifunctional theranostic features of MRI, MPI and magnetic hyperthermia are beneficial to improve thermo-therapy treatment of cancerous tissues while offering at the same time a potential readable and changing signal for image mapping.

Finally, as reported in chapter 3, we aim to develop an assembled nanoplatform made of magnetic iron oxide nanocube-based clusters and gadolinium-based nanoparticles that make the assembly responsive to the tumor microenvironment. This will enable to track tumor accumulation and disassembly of the nanoplatform for efficient thermotherapy based on T_1 gadolinium-changing signal. For this purpose, we synthesize multicomponent nanostructures starting from iron oxide nanocubes embedded in a polymeric bead (MNBs) with a surface negative charge and decorated with Sodium gadolinium fluoride nanoparticles ($NaGdF_4$ NPs), placed in between enzyme-degradable polymer spacers. Our hybrid structure achieved desired heating abilities under an alternative magnetic field of biological relevance. In addition to prominent T_2 properties coming from MNBs, we demonstrated disassembling and detaching of polymer and $NaGdF_4$ NPs from the surface of the MNBs upon exposure to enzymes that in turn improved water accessibility to $NaGdF_4$ NP surface with a corresponding increase of T_1 signal. In this way, we tracked the morphological changes of the systems at different time points of incubation in the presence of an enzyme, by MRI changing signal. This data was also confirmed by observing structural changes using TEM imaging. The integration of diagnostic tools to benchmark therapeutic probes could be a smart approach that enables to track the nanoparticle accumulation through artifact-free diagnosis and improve the heat efficiency of the magnetic hyperthermia treatment at the tumor.

Contributor's statement

The thesis chapter 1, of studying MH properties of different geometric nanoclusters of iron oxide nanocubes is an integration of our recently published articles. Chapter 2 is the extension of the study carried out in chapter 1, in which we exploited the same nanoclusters to investigate MPI and MRI relaxometry properties of nanoclusters. The Chapter 3 is the development of another multifunctional clusters that aim to pursue theranostic application based on magnetic hyperthermia and MRI imaging exploiting T_1 to T_2 change signal.

Chapter 1 title: Colloidal stable assemblies of iron oxide nanocubes for magnetic hyperthermia: the role of geometries and dipolar interactions on heating performances.
Title: Esterase-Cleavable 2D Assemblies of Magnetic Iron Oxide Nanocubes: Exploiting Enzymatic Polymer Disassembling To Improve Magnetic Hyperthermia Heat Losses. Authors: Sahitya Kumar Avugadda, Maria Elena Materia, Rinat Nigmatullin, David Cabrera, Roberto Marotta, Tamara Fernandez Cabada, Elena Marcello, Simone Nitti, Emilio J. Artés-Ibañez, Pooja Basnett, Claire Wilhelm, Francisco J. Teran, Ipsita Roy, and Teresa Pellegrino. Article Status: Published in Chemistry of Materials (2019) 31(15) 5450-5463. DOI: 10.1021/acs.chemmater.9b00728.

Title: Asymmetric Assembling of Iron Oxide Nanocubes for Improving Magnetic Hyperthermia Performance. Authors: Dina Niculaes, Aidin Lak, George C. Anyfantis, Sergio Marras, Oliver Laslett, Sahitya K. Avugadda, Marco Cassani, David Serantes, Ondrej Hovorka, Roy Chantrell, and Teresa Pellegrino*. Article Status: Published in ACS Nano (2017) 11(12) 12121-12133. DOI: 10.1021/acsnano.7b05182.

Chapter 2 title: Multimodel imaging abilities of nanoclusters of iron oxide nanocubes; magnetic particle imaging/magnetic resonance imaging. Authors: Sahitya K. Avugadda, Sameera Wickramasinghe, Stella Minseon Ju, Anna Cristina S Samia (Case Western Reserve University), Teresa Pellegrino*. Istituto Italiano di Tecnologia, Genova, Italy and Dipartimento di Chimica e Chimica Industriale, Università di Genova, Genova, Italy and Case Western Reserve University. Article Status: The manuscript under preparation for submission.

Chapter 3 title: Enzymatic Responsive Nanoclusters for Theranostic Applications. Contributors: Sahitya K. Avugadda, Helena Gavilan Rubio, Emille Rodrigues, Teresa Pellegrino*. Status: Ongoing project.

Contents

1. Colloidal Stable Assemblies of Iron Oxide Nanocubes for Magnetic Hyperthermia: The Role of Geometries and Dipolar Interactions on Heating Performances

1.1 Introduction

The magnetic nanoparticles (MNPs), thanks to their ideal properties, are widely studied for different applications including electronic, magnetic storage,[1] water treatment[2–4] and biomedicine.[5–7] In recent years, the use of iron oxide nanoparticles (IONPs) for biomedical purposes was booming including magnetic cell sorting, magnetic drug targeting, magnetic resonance imaging (MRI),[8–10] iron deficiency[11] and magnetic hyperthermia (MH) and very recently for magnetic particle imaging (MPI)[12–15]. Mainly because of their biocompatibility and lack of toxicity, and of having chance to control their surface properties in such a way suitable for biological conditions.[16] It is important to note, U.S food and drug administration had approved the application of IONPs for treatment and diagnostic purposes.[17,18] In this thesis we will focus mainly on the applications of iron oxide nanoparticles assemblies in MH, MPI and MRI.

1.1.1 Magnetic hyperthermia (MH)

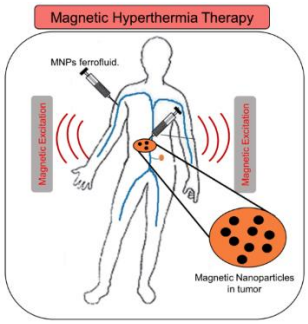

Figure 1.1. Scheme illustrates the general concept of magnetic nanoparticles mediated hyperthermia, where nanoparticles are injected at target site and subsequently excited using alternative magnetic fields to liberate heat. The same nanoparticles can be extended for MPI and MRI imaging.

Hyperthermia is a kind of medical treatment in which body tissue is exposed to temperatures higher than our body temperature in an effort to treat cancer. The term Hyperthermia derives from the two Greek words “hyper” and “thermé”, which means “rise” and “heat that denotes the basic principle of this treatment. The first evidence of hyperthermia treatment was seen when bacterial infection sarcoma disappeared under high feverish (40°C) conditions.[19,20] Similarly, cancer cells have shown to be vulnerable to temperatures above our body temperature (37 °C).[19] Thus, this treatment frequently uses a temperature raise between 40-45 °C would sufficient enough in order to sensitize/thermally ablate the cancerous cells.[21] The most conventional methodology for the treatment of hyperthermia was, the exposure of the whole body to high temperature (by placing the body in a hot water bath),[22] which was associated to side effects such as serious burns and discomfort to the patients.[23] In addition, such methodology is absolutely not localized, affecting to the whole body and not only the target tumor to be treated. Under such circumstances, MNPs caught scientific interest because of their featured ability of dissipating heat remotely, whenever necessary (“on and off” mechanism),[24,25] once in the target area, only under alternative magnetic fields (AMF) of certain field frequency and amplitude, which implies a localized therapy, rather than a therapy that affects all the surrounding healthy tissues.[26] Mostly, MNPs for this practice are well established in injectable forms. Such injected fluids are named “Magnetic nano ferrofluids”, as they are composed of iron oxide particles in the nanometers (nm) size-ranged were dispersed in a carrier liquid like water. The very first attempt to MNPs-based MH was given in 1957 by Gilchrist RK, treating metastasized lymph nodes cancer in dog.[27] Indeed, MH is a non-invasive therapy clinically approved in Europe to treat glioblastoma multiforme, an aggressive brain tumour[28] and under clinical trial for other solid tumors as well.[29,30]

Despite of its efficiency, MH suffers from few drawbacks mostly associated to the currently applied MNPs, which have poor heating dissipation performances, under AMF that are clinical practice, for instance, 110 kHz in frequency and 15 kA/m in magnetic field amplitude.[30] This means that in order to achieve a temperature increase of clinical relevance (42-45°C) the injection of high doses of magnetic material are mandatory in the (volumes of 0.5-12 mL of iron oxide fluid at an iron concentration of 112 mg/mL per treatment per patient). Injecting such high doses have several disadvantages. In particular, the possibility to use diagnostic tools, such as Magnetic resonance imaging (MRI) after MH, is being studied, as this imaging technique is routinely used for the investigations of certain organs (i.e. brain

in case of brain tumors), but so far such high doses MNPs used as heat agents do interference with the signal, as the dose of MNPs needed for MRI is several order of magnitude lower than that needed for MHT.[31] For this reason since last decade, numerous substantial efforts were dedicated to tune the size, shape, crystallinity and composition of MNPs with of the aim of achieving outstanding heating performance, making a second generation of iron-based nanoparticles for MH possible.[32,33] Despite current limitation of MH for translation into clinics, there is no doubt that Ferro fluids in coming future could emerge as new generation tracers not only for treatments but also for diagnosis. In this thesis we will focus on assemblies of MNPs for MH, MRI and MPI properties or, in addition, they could be combined with other inorganic materials to offer thernostic features.[34]

1.1.2 Physical principles of MNPs for hyperthermia

MH relies on the fact that when MNPs are exited with AMF of certain frequency and field amplitude, by generating hysteresis and relaxational losses and such magnetic energy is converted by the MNPs into heat. To understand these phenomena, one has to comprehend physical properties of magnets. When an external magnetic field is applied to a ferromagnetic material, such as iron oxide MNPs, the atomic spins in the nanocrystal align themselves with the external field and become magnetized when exposed to external fields applied, such magnetization of MNPs undergoes a closed loop during reversal of orientation: the hysteresis loop,[35] which is characterized by saturation magnetization M_s, remanent magnetization M_r, and coercivity H_c (Figure 1.2).

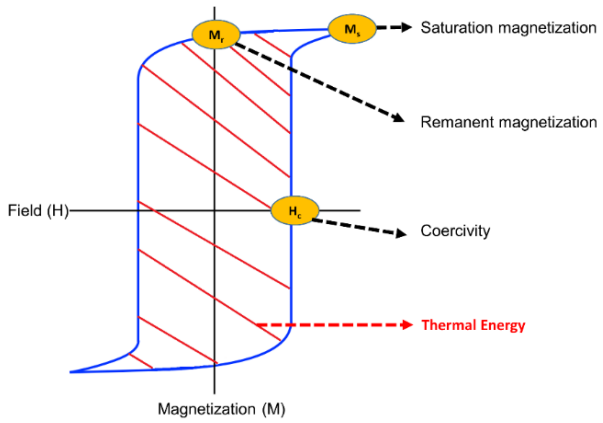

Figure 1.2. Saturation magnetization hysteresis loops of magnetic materials, scheme presenting most commonly expressed parameters.

Such parameters critically depend on the size, shape, chemical composition and magnetic interactions, among others, in MNPs.[36] Magnetic particles, depending on their size, geometry, and thus on their

volume, are composed of different magnetic domains, as shown in Figure 1.3. Above a critical size, the existence of more than one magnetic domain separated by domain walls within the nanoparticle helps to minimize internal energy of the nanoparticles. In a multidomain particle the process of reversal of the magnetization is incoherent, which is associated with a small coercive fields. On the other hand, below a certain critical volume, the existence of only one single magnetic domain becomes energetically favorable, and in these cases, the reversal magnetization process is coherent. Such critical size when mono-domain structure becomes favorable, for a given shape, depends on the chemical composition and in case of IONPs lies around 60-80 nm.[37,38] The magnetization of single-domain MNPs, is frequently described as one giant magnetic moment by summing the individual magnetic moments of each constituent atom. This approximation is called the "macro-spin approximation." In this regime, the reduction in the volume of the MNPs is associated to a decrease in the coercive field and when MNPs are small enough, the energy barriers for magnetization reversal, which are proportional to grain volume, are relatively low compared to thermal energy. When the thermal energy at RT is enough to flip the magnetic moment, the material has suffered a transition from the ferromagnetic to the superparamagnetic regime (SPNPs), which for IONPs is displayed by MNPs with sizes typically below 25 nm.[37,38] In this regime, coercive field and remanent magnetization are 0 at 0 field applied. For biomedical applications, particles within the single domain, and either with a superparamagnetic behavior, or in the interface between ferromagnetic and superparamagnetic are preferred, due to the absence of agglomeration in absence of magnetic external field gradients thus behaving as inert carrier which can be promptly activated by the magnetic field only when applied.[39]

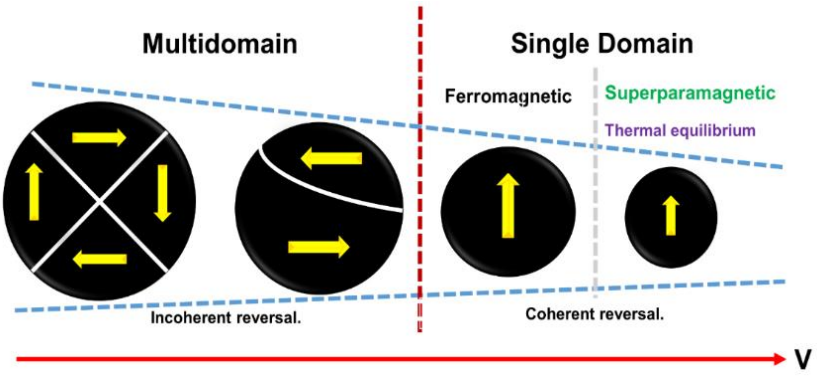

Figure 1.3. The configuration of magnetic domains as factor of particle size.

The overall energy of such single domain SPNPs depend on their anisotropic energy (E_A) and Zeeman energy (E_z) given by the equation 1.1.[40]

$$E = E_A + E_z = KV \sin_2\Theta - HVM_s \cos(\Theta - \phi) \quad \text{Equation 1.1}$$

Where K stands for uniaxial anisotropy, while *H, V and* M_s imply applied field, Volume and saturation magnetization, respectively, and Θ is angle at which the easy axis (energetically favorable direction of spontaneous magnetization) of MNPs oriented towards magnetization, ϕ is the angle between applied magnetic fields and easy axis. In absence of applied fields, the energy barrier of SPNPs is equal to KV, whose entire anisotropy energy barrier is comparable to the thermal equilibrium energy; that is $KV = k_BT$, where k_B is a Boltzmann constant.

The time between two flips in direction is called the Neel relaxation time.[41,42] In SPNPs, the average magnetization of the nanoparticles is zero when no external magnetic field is applied and the measurement time for the magnetization of the nanoparticles is greater than the Neel relaxation time (τ_N). With an external magnetic field applied, the nanoparticles are magnetized like paramagnets, but with much greater susceptibility. When the measurement time is much greater than the Neel relaxation time ($\tau_m >> \tau_N$), the particle is said to be blocked. The blocking temperature (T_B), is the temperature at which the transition from the ferromagnetic (the blocked state) and superparamagnetic states occurs. In addition, ferrofluids applied in MH have another mechanism aside from Neel relaxation that changes the directions of the particles' magnetic moments called Brownian relaxation,[43] which cause the grains to physically spin, as shown in Figure 1.4. Currently used single-domain MNPs can heat by Neel, Brownian relaxation or a mixture or both.

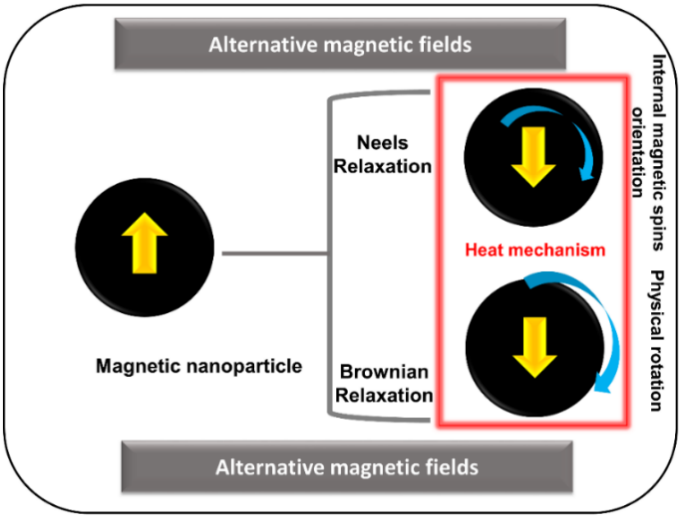

Figure 1. 4. The two relaxation processes that dictates the heating properties of magnetic nanoparticles.

This concept was first explained by the Louis Neels,[36] whose relaxation time given by following formula (Eq. 1.2).

$$\tau_N = \tau_0 \exp(KV/kBT) \qquad \text{Equation 1.2}$$

where $\tau_0 = 10^{-9}$ s. k_B = Boltzmann constant and T = temperature. While the later, comes from the physical rotation of the MNPs depending on the hydrodynamic diameters (dH) and viscosity of the media in which they measured given by the formula.

$$\tau_B = 3\eta V_H / k_B T \qquad \text{Equation 1.3}$$

where η = viscosity of media, V_H is the hydrodynamic size of MNPs.

The effective relaxation time of material can be estimated by combining two relaxation times that given by following formula (Eq.1.4).

$$\tau = \tau_N \tau_B / \tau_N + \tau_B \qquad \text{Equation 1.4}$$

There are different types of theories suitable for describing hysteresis loops of MNPs, and therefore to predict hyperthermia performance from various MNPs: equilibrium functions, Stoner–Wohlfarth model (SW) based theories,[39,44,45] using the Neel–Brown relaxation time. However, linear response theory (LRT) is compiled only in SPNPs at low magnetic fields very far from the saturation field of the NPs.[46] Under this regime, SAR is proportional to H_{max}^2 and its amplitude could be deduced directly from

the imaginary part of the susceptibility χ''.[46], as described by Landau and Lifschitz in their formula for the power P dissipated during magnetic relaxation under the application of an alternating magnetic field.

$$P\,(f,H) = \pi\mu_0\,\chi'' H^2 f \qquad \textit{Equation 1.5}$$

However LRT is inappropriate for ferromagnetic NPs or for NPs close to the superparamagnetic/ferromagnetic transition (as it is the case of most of the MNPs presented in this thesis). In the ferromagnetic state, the SW model is more suitable to interpret the experimental data.

The original Stoner–Wohlfarth model does not take into account any thermal activation, which is relevant at T = 0 K or in the limit of infinite field frequency.[39] Thus, the switch of the magnetization from the metastable state to the equilibrium position can only occur when the energy barrier is fully removed by the magnetic field. The field at which this occurs is called the critical field.[39] This theory predicts magnetization reversal by a uniform mode, so-called homogeneous rotation. In this case, hysteresis loss is proportional to the product of coercivity and remanence. Interestingly, this theory predicts a hysteresis loop with the shape of a perfect square whose maximal area is given as:

$$A = 4\mu_0 H_c M_s = 4\mu_0 H_K M_s = 8K_{eff} \qquad \textit{Equation 1.6}$$

Nevertheless, the prediction of the area of the hysteresis loops and thus the heating performances of MNPs remains an open problem. The experimental determination of the heat generating efficiency of MNPs is done in the terms of specific absorption rates (SAR), which means the energy absorbed per mass of iron on exposing to the electromagnetic fields, given by formula Eq. 1.5.

$$SAR = \frac{P}{m(MNP)} \qquad \textit{Equation 1.7}$$

Where *p* is power dissipated and *m* is mass of MNPs.

1.1.3 Route to determine the magnetic hyperthermia properties of MNPs

The MH abilities of MNPs can be estimated by two main experimental approaches; 1). Calorimetric measurement and 2). Inductive magnetometric method.[36]

Calorimetric measurement

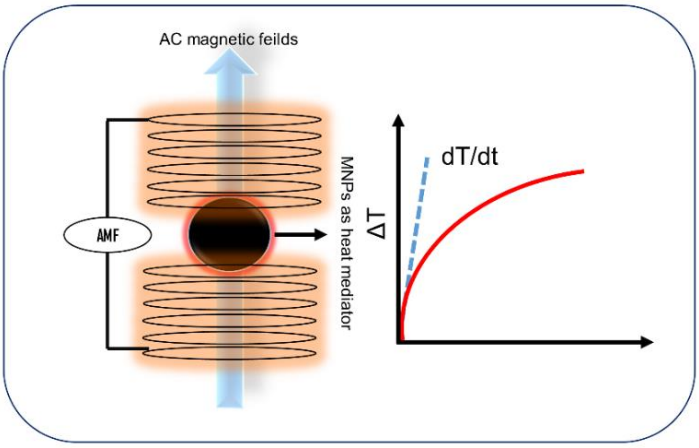

Figure 1.5. A general scheme of magnetic hyperthermia setup. The application of AMFs induces temperature increase in MNPs which was as function of the time using optic thermo recorder. The specific absorption rate; SAR can be calculated considering initial slope of dT/dt of the curve.

The calorimetric method is most commonly used technique for MH approximation of MNPs. In this, temperature raise from fine MNPs dispersion, which are placed in the center of a radiofrequency generating coil (water cooled), is recorded by means of optic thermal probe. The entire scheme of instrument scheme was given in Figure 1.5. The corresponding SAR was calculated from the temperature derivatives by using Equation 1.8 below.

$$SAR\ (W/g) = \frac{C}{m} \cdot \frac{dT}{dt} \qquad \text{Equation 1.8}$$

Where *c* defines the specific heat capacity of media, *m* is mass of MNPs (often express as mg of Fe for IONPs), *dT/dt* is initial slope of temperature difference achieved in a well-defined time (few seconds). The values of SAR are expressed in units of Watts per gram (W/g). Maintaining adiabatic environment, such as vacuum conditions, in order to prevent heat losses to surrounding environment is a costly approach.[47,48] Hence, most groups adopted cost effective and easy handling non-adiabatic conditions to perform calorimeter.[49] However, temperature raise heat curves in this method, starts to drop as they losses their heat into surrounding environment. Therefore, for a better approximation, slope from initial few seconds of heat curve is considered for calculation, as it is denoted with blue dotted line in Figure 1.5.

Inductive magnetometric method

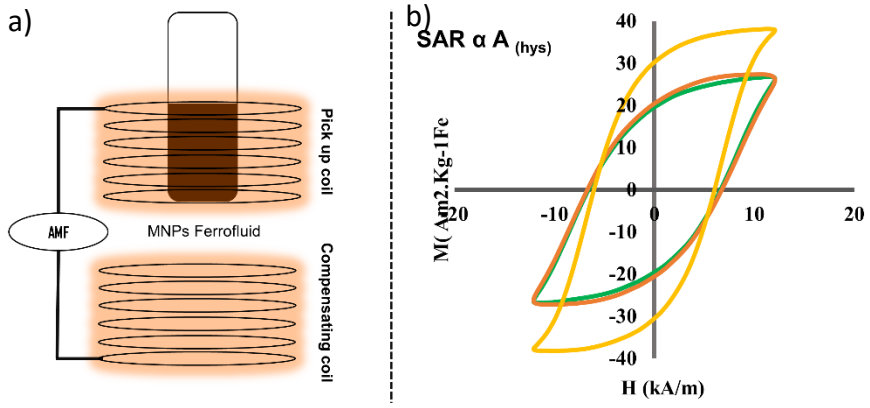

Figure 1.6. a) Scheme illustrates Inductive magnetometric instrument. b) The AC susceptibility measurement derived hysteresis area of curve where the SAR of the sample is proportional to loop area.

Secondly, the SAR of MNPs can be estimated by measuring their dynamic magnetization M (t), where the hysteresis loop area can be obtained.[29] In this setup, pick up coil rounding the holder receives dynamic magnetization M(t) of sample, while the lower compensating coil with no sample have minimal induced voltage. Basically it works on the principle of Faraday's law of induction, where it record magnetic field interaction with the electric circuit, which creates an induction. In this magnetometric method, SAR can be calculated by integrating directly the dynamic M(t) (in another word the area of hysteresis loop) and strength of applied magnetic fields, which was normalized to the concentration of MNPs and value derived by using following equation.

$$SAR = \frac{f}{c} \oint M(t)\, d(H) \qquad \text{Equation 1.9}$$

Where *f* stands for the frequency, c for concentration of MNPs. According to this, the SAR derivative is directly proportional to the area of the hysteresis loop as emphasized in Figure 1.6.

1.1.4 Biological safe limits of alternative magnetic fields for MH

A great debate was happening within the scientific community working in the field of MH, in order to determine the biologically acceptable limits of magnetic excitation fields. Because, apart from M_s, *V* and *K* of MNPs, the strength of field (*H*) and frequency (*f*) also have proportional influence on the heating properties. Within this, the heat dissipation from MNPs can increase linearly with an increase

in excitation strength, up to certain critical size limit. However, application of high frequencies was associated with a serious concern due to the fact of generating "eddy current" within the tissue which may cause non-specific heating in off-target organs.[50] Atkinson and Brezovich are the ones who first estimated that this H*f* product should not cross the limit of 4.8×10^8 A m^{-1} s^{-1}.[50,51] Later, Hergt *et al*., quoted, this can be extended upto 5×10^9 $A{\cdot}m^{-1}{\cdot}s^{-1}$, since the applicator used by Atkinson was far different from clinical applicators currently in use[52] and this range was mostly adopted. Just to mention, however the current clinical studies mostly applying the frequency fields ranging between *f*= 50 kHz - 120 kHz and field = 0-5 kA m^{-1}, which are obviously lower than range established by Hergt *et al*. The amount of eddy current generated within tissue is possible to calculate by applying the following Equation 1.8, as it was adopted by Mamiya et al.[53]

$$P_e = 1/2\,\pi^2\mu_0^2\sigma r^2 f^2 H_{AC}^2 \qquad Equation\ 1.10$$

Where σ is the electrical conductivity of the tissue, (constant σ = 0.2 $S{\cdot}m^{-1}$) and r is the radius of body (assuming cylindrical). As per induction law, the probability of heating is proportional to the frequency (*f*), field (*H*) and the diameter of the coil (D) given by formula (H.*f*.D).[52]

1.1.5 Effect of dipolar interaction on heat properties of MNPs

The SAR properties of MNPs depends on *Ms*, *V* and *K (*anisotropy) that can be optimized by tuning their intrinsic properties, which includes size, shape, composition and crystallinity.[29] Among the MNPs available, iron oxide nanoparticles (IONPs) with cubic morphologies have stood significantly as the best in terms of their SAR values, which were report to have 10 to 20 times higher SAR values than those of spherical IONPs.[54,55] The reason for such behavior was theoretically explained. As given in Figure 1.7 due to the fact of their defective free, low index faces, for instance, 100 cubic faces, where the surface spin canting was relatively less (Figure 1.7a). On the contrary, the spherical moieties with curved surface would experience higher surface spin canting than flat surfaces since their spins remain disoriented. The calculated spin disorder for cube are around 4% versus the 8 % of spheres as shown in Figure 1.7b.[56] Indeed given the large fraction of surface atoms in such a tiny nanoparticles, the disordered surface spins do not contribute to the heat.

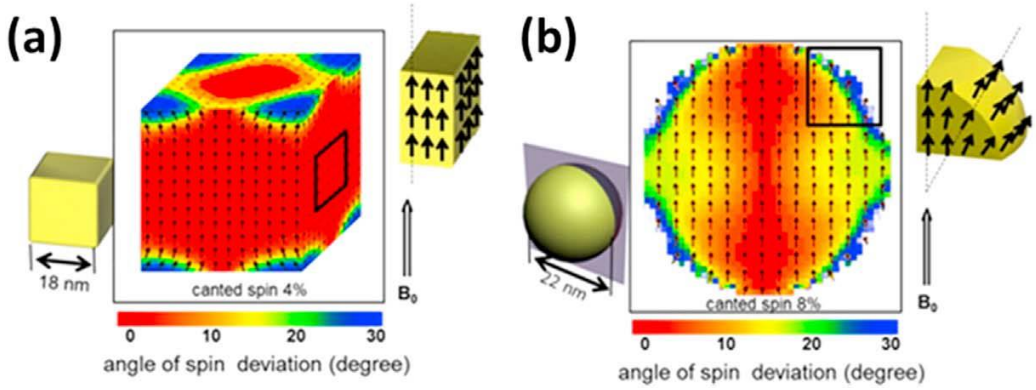

Figure 1.7. Simulated magnetic spin states of (a) cubic and (b) spherical nanoparticles; the color map indicates the degree of spin canting in the presence of an external magnetic field (B_0), where red indicates non-deviated spins and blue indicates highly canted spin states; local spin states on the surfaces of nanoparticles are depicted on the right corners of (a) and (b). Reprinted with permission from reference(56) Copyright © 2012, American Chemical Society.

It was reported that the MNPs highly concentrated inside the cells, tends to aggregate because of internal complex and viscous environment and the consequent strong magnetic dipolar interactions could predominantly shrink their MH efficiency by 70-90 %.[57–59] Within this, it has been realized that properties of MNPs profoundly varies under high concentrations due to dipolar coupling, which makes hyperthermia properties to differ in comparison with well-dispersed MNPs.[60–62] Indeed, Salas, G. *et al*. reported difference in heat abilities of 12 and 20 nm nanoparticles as factor of concentration. When those samples prepared in agarose solution at two different concentrations of 2.5 mg_{Fe} /mL and 10 mg_{Fe} /mL, a steep reduction of SAR has occurred at higher concentrations due to fact they formed instant temporary nanoclusters, where the particles are randomly oriented.[63] Similar conclusions were given by Materia, M. E.*et al*, where the iron oxide nanocubes are randomly oriented and assembled within colloidal stable polymer matrix with a hydrodynamic size of around 173 nm structure named as "magnetic nanobeads (MNBs)". The 3D-orientated IONPs in these beads undergo immense magnetic frustrations, consequently reducing SAR values.[64] Such isotropic, densely packed spatial arrangement could create very strong magnetic dipole-dipole interactions (more like an antiferromagnetic coupling), in return interrupts the relaxation of individual magnetic momentums of the nanocrystals in the cluster, thus demagnetize and suppress the SAR.[65,66] However, this effect strongly relays on average hydrodynamic size of assembly and degree of interparticular spacing. Fu,R *et al*. performed experimental and simulation study on nanoparticles assemblies of different size and concluded random

aggregates brings SAR increase only if clusters are optimally small, that brings structural anisotropy enhancement as demonstrated in Figure 1.8a.[67]

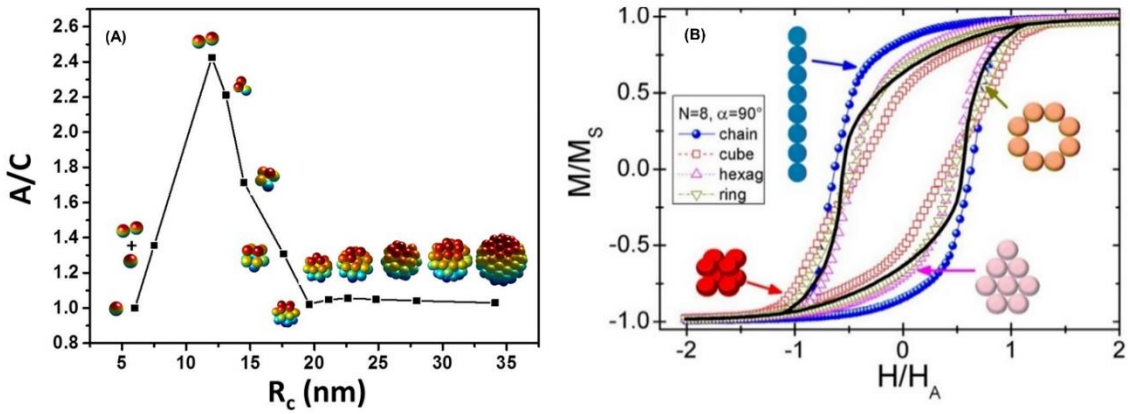

Figure 1.8. A) Change of shape anisotropy in numerically fabricated clusters as function of average radius (Rc).[67] (B). Simulated M(H) hysteresis curves corresponding to different spatial arrangements (bidimensional chain, hexagonal lattice, and ring; 3D cube) of the same amount of particles, N = 8, and for the easy anisotropy axes randomly distributed into a cone of angle α = 90°. The black line stands for the case of noninteracting particles. Reprinted with permission from reference ([68]) Copyright © 2014, American Chemical Society.

Instead, MNPs have tendency to form spontaneous, temporary linear clusters in response to AC magnetic fields, that changing SAR in a positive direction.[69] Many theoretically and experimentally works justified the reasons for the impact of linear clustering on heating, that was mainly due to the linear dipolar coupling and increased shape anisotropy.[70,71] In 1D-array of linear chains, particles experience uniaxial magnetic dipolar coupling, where their magnetic easy axis aligned along the longitudinal direction of the chain length, hence the magnetic spin behaves as single elongated entity with an improved uniaxial anisotropy,[72] consequently, responds quickly to the magnetic field excitations, thus the higher SAR. In addition, they do not face second order effect coming from adjacent nanoparticles, likewise to 3D and 2D arrangements, if so, it would create antiferromagnetic coupling. Within this explanation, Alphandéry, E. et al reported the efficiency of linear chains of the cubic shaped MNPs (35-50 nm) extracted from the organelles of bactereosomes(cultured under anaerobic conditions) in eradicating cancer with respect to their individual magnetosome nanoparticles,[73,74] as well as for MRI applications.[75] Particle in chains have a locked magnetic moments in the direction of applied magnetic fields that can creates ferromagnetic coupling within the particles[76], rather being antiferromagnetic, to participate in improvement of heating properties.[45,77,78] Serantes, D.et al.[68] justified the outcomes of Alphandéry, E. *et al.*, through his stimulation and experimental work. In their

analysis, among MNPs arranged in chains, rings, 2D, 3D (an ensemble of 8 particles in each) and isolated forms, the dipolar interactions diminished the hysteresis loop areas in all cases except for linear chains. Advanced properties of strings lies within the explanation given before, that the uniaxial coupling of magnetic easy axis along direction of the chain length, expands magnetic anisotropy, thus hysteresis loop area (Figure 1.8b) and eventually the SAR. It is worthy to state, SAR trend within linear geometries also depends on angle at which they align towards applied magnetic fields. Experimental work of Serantes, D. et al, in agarose shown, that chains aligned parallel (0°) to AC magnetic fields given maximum SAR, conversely, the one at 45° and 90° behave intermediate and poor respectively. According to their assumption, chains in parallel alignment may have more chance of rotating, thus the higher SAR. From this same study we can interpret, the two-dimensional assemblies (2D-arrays) of MNPs would show an intermediate behavior in terms of loop area, than those of isolated nanoparticle, 1D and 3D-assemblies. The distinct behavior is coming from the fact of their spatial confinement of the MNPs. Though the MNPs here are ordered in a monolayer, their magnetic easy axis were partial disrupted by the adjacent magnetic momentums, more likely as a second order effect, that creates a slight antiferromagnetic coupling.[76,79] This partial misalignment of magnetic easy axis would partially erase hysteresis loop area, but definitely a minimal magnetic frustrations and demagnetization effect than 3D ordered assemblies, hence could preserves heating abilities not less than 3D forms.

Therefore, besides choosing magnetic nanocrystals with individual anisotropy, a strategy of assembling MNPs into permanent optimized anisomeric geometries with colloidal stability, has been recently implemented to further exceed the SAR properties of same MNPs. Indeed, these findings inspired many groups to explore the effects of clustering MNPs into different morphologies for magnetic fluid hyperthermia (MFH).[33,73,80–84]

1.1.6 Strategies for colloidal stable magnetic assemblies

The colloidally stable structures of fixed configuration can be produced through sol-gel (stobers process)[85] and microemulsion approaches,[86] however the latter was widely accepted by the scientific community. Most of the high performing MNPs reported in literature were produced through non-hydrolytic routes with hydrophobic properties, therefore these ensembling methods using biocompatible, anisotropic templates such as, amphiphilic block co-polymers or mesoporous silica, became versatile and robust practice for obtaining water stable clusters, that suit bioneeds.

1.1.6.1 Micro emulsion technique: amphiphilic polymers for magnetic assemblies

Amphiphilic polymers are more widely studied than any other, to assemble MNPs for magnetic hyperthermia. These polymers are composed of both hydrophilic (water retaining) and hydrophobic groups (water repelling) in its same backbone.[87] Through micro-emulsion technique, when an immiscible or nearly miscible polar solvent is added to the nonpolar solvent mixture with polymer, the hydrophobic moieties will collapse rapidly into micellar structure. Various, non-toxic, biocompatible block co-polymers with amphiphilic properties were widely reported in the literature, such as poly(ε-caprolactone)-b-poly(ethylene glycol), poly- (trimethylammonium ethyl acrylate methyl sulfate)-b-poly- (acrylamide), poly(ethylene oxide-b-acrylate), poly(lactic-co-glycolic acid)-b-poly(ethylene glycol), poly(ethylene imine)-b-poly(ε-caprolactone)-b-poly(ethylene glycol), Poly(maleic anhydride-alt-1-octadecene), poly(styrene-co-maleic anhydride) cumene-terminated to encapsulate or assemble MNPs for theranostic application.[88] Just to mention, by adopting this method, our group previously encapsulated spherical[89] or cubic shaped iron oxide nanoparticles,[64] that prepared through non-hydrolytic routes, into magnetic polymerosomes using an amphiphilic polymer; poly maleic anhydride alt-octadecene. The initial mixture of particles and polymer in organic solvent THF/$CHCl_3$, later precipitated in a controlled manner by adding anti-solvent; acetonitrile. Here, the acetonitrile, having relatively higher polarity than THF functions to de-stabilize and induce rapid assembling of IONCs within hydrophobic domain of the polymer, while exposing the hydrophilic parts into the solution as illustrated in Figure 1.9a.

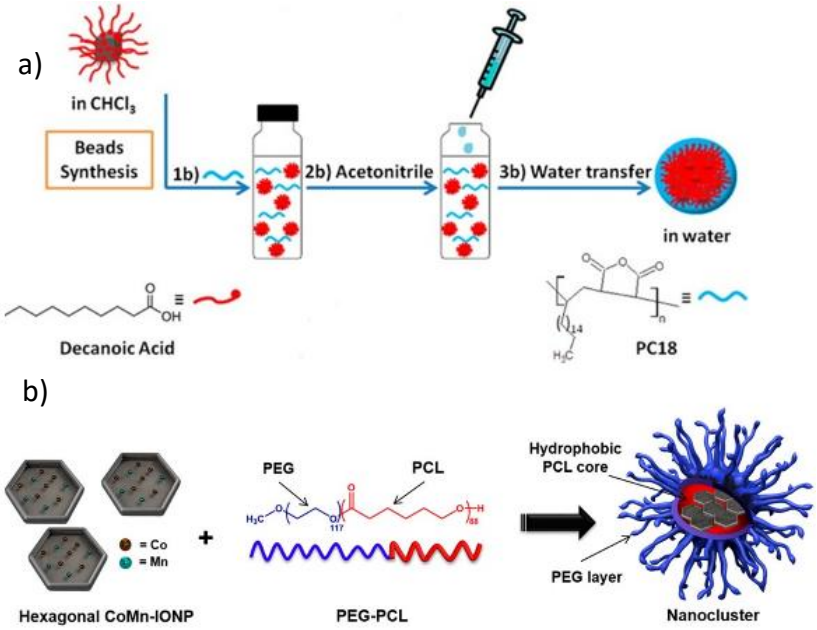

Figure 1.9. Schematic illustration of microemulsion techinique, a) Preparation of water soluble magnetic nanobeads (MNBs). Reprinted with permission from reference ([83]) copyright © 2015, American Chemical Society. b) The encapsulation of hexagon-shaped cobalt- and manganese-doped iron oxide nanoparticles (CoMn-IONP cluster) in polymer matrix of poly(ethylene glycol)-b-poly(ε-caprolactone). Reprinted with permission from reference ([90])Copyright © 2019, American Chemical Society.

A similar approach was recently adopted by H. A. *et al*., where the high efficient, cobalt and manganese doped hexagonal iron oxide nanocrystals (CoMn-IONP) were assembled into anisotropic nanoclusters (CoMn-IONP clusters) for magnetic hyperthermia. The oleic acid capped CoMn-IONP are likewise dissolved in THF with biocompatible amphiphilic polymer; poly(ethylene glycol)-b-poly(ε-caprolactone) (PEG–PCL, 15 kDa), where the particles are encapsulated in hydrophobic PCL moiety of 10 kDa, on adding aqueous solution. Whereas, the remaining hydrophilic PEG moieties (5 kDa) extends out solubilizing final clusters in water (Figure 1.9b).

1.1.6.2 Sol-gel approach

As an alternative to organic amphiphilic polymers, MNPs can assemble through two step sol-gel-based Stöber process by using tetraethyl orthosilicate (TEOS) as silica precursor. In this two-step reaction, the hydrophobic inorganic nanomaterials are water transferred firstly using water-soluble surfactants such as cetyltrimethylammonium bromide (CTAB) or tetramethylammonium hydroxide (TMAOH) and secondly, the TEOS precursor introduced to obtain silica coated assemblies.[85,91] Accordingly, Andreu,I. *et al*. fabricated colloidal water stable one-dimensional structures (nano-worms) from hydrophobic

iron oxide nanocubes of size 13±1 nm.[85] As mentioned, cubes were water-transferred using TMAOH and later, in a mixture of water/EthOH, with ammonia and TEOS, under prolonged sonication, transformed them into nanoworms, where its silica thickness can be adjusted by varying the amount of TEOS or the sonication time.

1.1.7 Objective of the work

While several studies have been reported for three-dimensional magnetic beads (3D-MNBs),[33,83,92] only few attempts of producing a 2D-assembly of MNPs have been successful, however some of them were following solid substrate based deposition methods such as the Langmuir-Blodget technique,[93,94] a chemically assisted self-assembly technique,[95] or a magnetic field-induced assembly technique.[96] Moreover, as-produced 2D monolayers of MNPs, which are in the micrometer size range, are especially applied to magnetic storage, sensing or filtering applications.[97–100] To date, the studies on colloidal stable 2D assemblies of inorganic nanoparticles stable are very few reports, but one of this kind is the work of Yan *et al*. where the gold nanoparticles are self-assembled into 2D nanogrids, using DNA as a mediator for a nano-optonic application.[101] In another, Andreau *et al*. have also reported a magnetic study on 2D assembly of MNPs embedded in a solid matrix of epoxy resin (micrometer size) or on 2D arrangement of MNPs immobilized in PLGA nanosphere that is 200 nm in size; a group of 2 to 12 particles in each assembly. Although this paper has pioneered the work on magnetic nanocrystal arrangements in hyperthermia, due to the choice of the initial particles with poor heat performances, the SAR values recorded were not impressive in MH point of view, whose values range between 0.7 and 2.9 W/g.[102]

In this work, we have made an attempt to cluster MNPs into a 2D assembly of mesoscale range, using our benchmark high performing iron oxide nanocubes (IONCs).[103] Moreover, we aim to investigate the transformation of 2D structures upon exposure to enzyme action, where we have exploited the polymer cleavable in presence of lytic enzyme, here the esterase, which is abundant in the tumor microenvironment.[104] For this purpose, an aliphatic polyesters, Polyhydroxyalkanoates (PHAs), produced by the group of Dr. Ipsita Roy, West Minister Collage London. PHAs are a class of bio resorbable and highly biocompatible polymers extracted from different range of bacterial strains[105,106] and they are susceptible to hydrolytic depolymerization which includes bio-catalytic cleavage using enzymes such as esterase's and lipases.[107,108] The enzymatic and hydrolytic cleavage of the ester bonds

leads to PHA resorption in the human body, for the reason which PHAs have been found as an suitable candidate for tissue engineering,[109–111] and drug delivery[112–116] applications. In principle, PHAs present in two types, short chain length PHAs (scl-PHAs),[117] composed of C_4-C_5 carbon chain length monomers and medium chain length PHAs (mcl-PHAs),[118] with C_6-C_{16} carbon chain length monomers. In our study, we used a soft mcl-PHA copolymer which is in an oligomeric form (oligo-PHA;10 KDa) after knowing thier amphiphilic and resorbable properties[115,116,119] and good solubility in both hydrophobic and hydrophilic solvents. A wide range of suitable solvents for oligo-PHA enables utilization of this material in solution phase self-assembly methods.[120] Indeed, in this study, oligo-PHA directed 2D ordering of highly interactive IONCs into colloidal stable 2D structures (2D-MNBs) and the properties of these 2D-MNBs was systematically investigated in comparison to those of both isolated nanocubes and 3D centro-symmetrical assemblies produced from same nanocubes. The most remarkable features of the 2D-MNBs assembled with the assistance of natural polyester is the ability to disassembly in smaller assemblies of chains of nanocubes due to enzymatic cleavage of the polymer under biological conditions, and in turn, these chains doubled the heat efficiency (two-fold increase of the SAR value) at a well-defined incubation time point. On the other hand, 3D and 2D clusters, being composed of multiple MNPs which can align simultaneously to an external magnet, accumulate much quicker than individual MNPs to an external magnet.[121] The quick response is crucial for magnetically guide MNPs in order to apply local MH or heat-mediated drug delivery at sufficient MNPs dose at the tumor site.

In addition to the above work, in the group of Dr. Pellegrino at IIT (work initiated by Dr. Dina Niculaes), I synthesized colloidally stable geometries of core-shell IONCs, which includes (i) single particles, (ii) Dimer/Trimer assemblies, and (iii) centrosymmetric structures, from same core-shell iron oxide nanocubes (less interacting) by using one specific amphiphilic polymer, poly(styrene-co maleic anhydride), cumene-terminated, where the amount of polymer molecules per nanometer surface of nanoparticle was exploited as a main parameter to tune the morphology and we studied the evolution of SAR with the size and spatial arrangement of clusters. The SAR of Dimer/Trimer (short chains) was compared to the heating performances of single nanocubes and centrosymmetric assemblies.[122] The SAR enhancement was favoured for the iron oxide nanocubes in the form of Dimers/Trimers because of their effective magnetic anisotropy of the nanocube chains and the long-range dipolar interactions between the nanocrystals within the chains.[123] This work clearly complements the results of 2D-MNBs

where their initial structures were disassembled into short chains similar to that of Dimers/Trimers, upon exposure to esterase enzyme. In both cases, this short chained clusters exhibit advanced heating properties.

1.2 Materials and methods

1.2.1 Materials

Oligo-PHA, tetrahydrofuran(99%), nitrodopamine-PEG carboxylic terminated ligand (DOPA-PEG), triethylamine (TEA), toluene (99%), Poly(maleic anhydride-alt-1-octadecene) (PC18, Mn 30 000−50 000, Aldrich), Milli-Q water (18.2 MΩ, filtered with filter pore size 0.22 µM) from Millipore, Chloroform ($CHCl_3$, Sigma-Aldrich, 99%), iron(III) acetylacetonate (Acros Organics, 99%), decanoic acid (Acros Organics, 99%), dibenzyl ether (Acros Organic, 99%), squalene (Alfa Aesar, 98%), and liver porcine esterase(Sigma Aldrich), fetal bovine serum. The bacteria species Pseudomonas mendocina CH50 used for the production of PHA was obtained from the National Collection of the Industrial and Marine Bacteria (NCIMB 10541). For the production, characterization and hydrolysis of PHA ammonium sulphate, potassium dihydrogen phosphate, Glucose, magnesium sulphate heptahydrate, methyl benzoate, anhydrous sodium sulfate were purchased from Sigma-Aldrich (Dorset, UK) while disodium hydrogen phosphate, chloroform, methanol, tetrahydrofuran were purchased from VWR (Poole, UK). All the chemical were used as supplied without any further purification. Iron pentacarbonyl (Fe(CO)5, 98%), 1-octadecene (1-ODE, 99%), OA (90%), triethylamine (99%), ethanol, dichloromethane, poly(styrene-comaleic anhydride), cumene-terminated (Mn = 1600 g/mol), obtained from Sigma-Aldrich. Sodium oleate (97%) was obtained from TCI. THF for cluster production was purchased from Carlo Erba Reagents.

1.2.2 Synthesis of iron oxide nanocubes (IONCs)

IONCs of edge length of 16±2 nm were synthesized according to previously published protocols which following solvo-thermal method.[83,103] Briefly, 0.353 g of iron (III) acetyl acetonate (1 mmol) 0.69 g of decanoic acid (4 mmol), 7 mL squalene were dissolved in 18 mL of dibenzyl ether in three-neck flask of 100 mL. After degassing mixture for 120 min at 65 °C, heated up to 200°C at a rate of 3°C/min which was maintained for 2.5 h. Later, this temperature was increased further to 310°C, at a rate of 7° C/min,

and then maintained for another 1 more hour. After this step, by cooling down to room temperature, the particle in solution were precipitated by centrifuged at 4500 rpm on adding 60 mL of acetone. We have repeated centrifugation for another two times in order to eradicate excess surfactant in mixture and finally, re-dissolved the dark pellet in 15 mL of chloroform.

1.2.3 Production of mcl-PHAs by *Pseudomonas mendocina* CH50

The mcl-PHAs was extracted from *Pseudomonas mendocina* CH50 (NCIMB 10541) that cultured using coconut oil as the sole carbon source, according to work of Basnett *et al*., 2019,[124] performed at Westminster College London, in the group of Dr. Ipsita Roy. The production was implemented in a 20L bioreactor. mcl-PHA copolymer was recovered from the freeze-dried biomass by a two-stage Soxhlet extraction process using methanol and chloroform as solvents and the polymer was precipitated using ice-cold methanol, where the product mcl-PHA was identified by GC-MS (Figure 1.10) and ^{1}H, ^{13}C NMR (Figure 1.11) as the terpolymer composed of 3-hydroxyoctanoate, 3-hydroxydecanoate and 3-hydroxydodecanoate (molar fraction for each monomer was found to be 0.30, 0.48 and 0.22 respectively) Poly(3-hydroxyactanoate-co-3-hydroxydecanoate-co-3 hydroxydodecanoate.

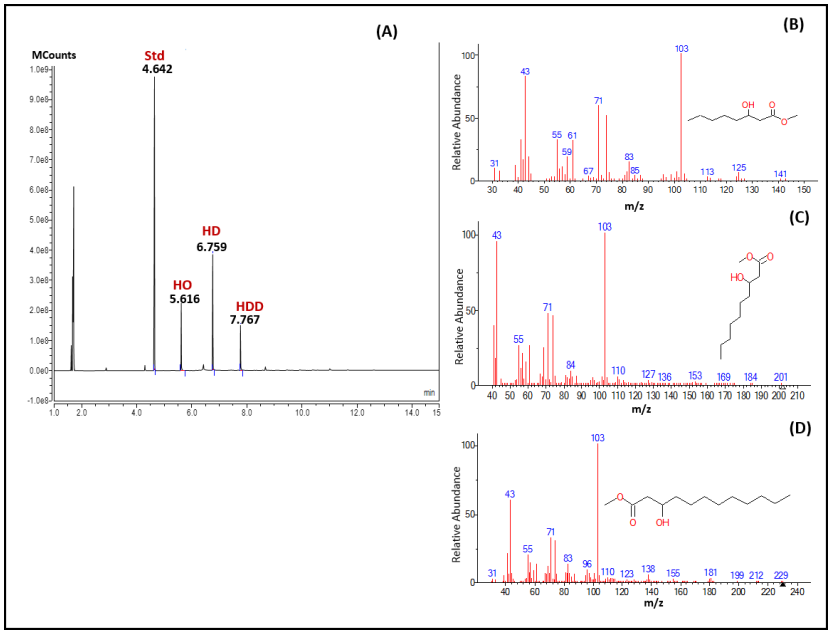

Figure 1.10. Gas chromatogram (A) and mass spectra (B-D) of the polymer produced by P. mendocina CH50 with coconut oil as the sole carbon source. Reprinted with permission of reference[125] Copyright © 2019, American Chemical Society.

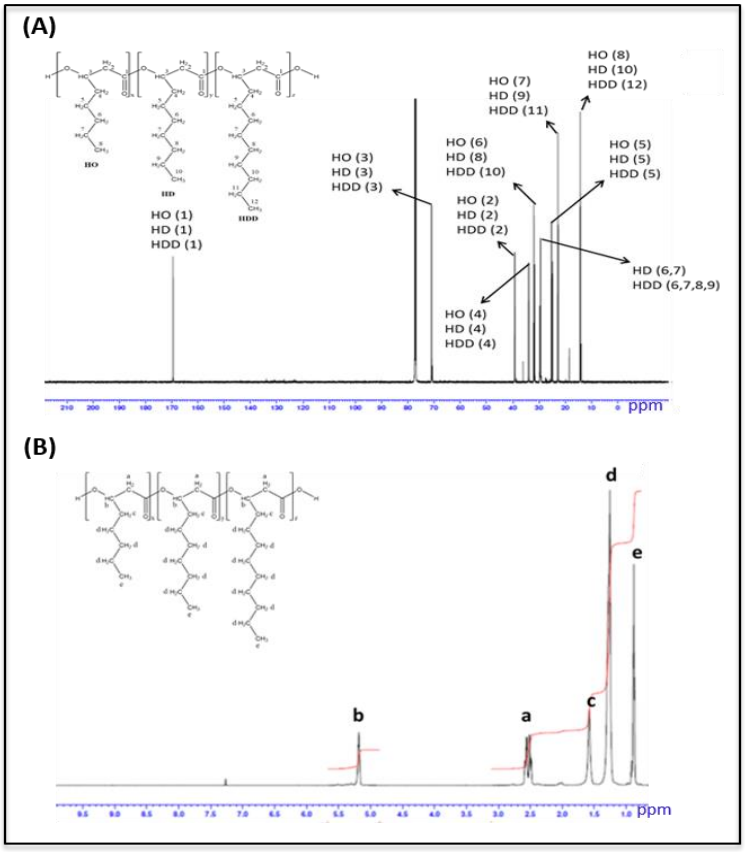

Figure 1.11. [13]Carbon NMR (A) and 1H NMR (B) spectra of the polymer produced by P. mendocina CH50 with coconut oil as the sole carbon source. Reprinted with permission of reference(125) Copyright © 2019, American Chemical Society.

1.2.4 Hydrolytic depolymerization of mcl-PHA

The oligomeric derivative of PHA (oligo-PHA) was prepared by hydrolytic depolymerization of mcl-PHA copolymer. 3 g of mcl-PHA pellets were added to a mixture of 166 mL of glacial acetic acid and 34 mL of deionized water and subsequently hydrolyzed for 20 hours at 100-105°C under reflux for 20 hours. Later, the reaction was quenched by dropping 200 mL of chilled deionized water into the reaction mixture. This produced an unstable emulsion of the product in aqueous media. Through solvent extraction methods product was extracted using 300 mL of chloroform. The water content in chloroform dissolved product was retained by adding crystals of anhydrous sodium sulfate. Once after the solution turns clear, the oligo-PHA was concentrated by rotary evaporation. The residues of chloroform from the product were excluded through evaporation under room temperature. Following this, the waxy oligo-PHA was re-dissolved in a small volume of tetrahydrofuran (THF) and re-precipitated by pouring into cold methanol kept in a crystallizing dish. When the product is precipitate

at the bottom of the dish and its walls, solvent mixture with admixtures was decanted and finally the oligo-PHA was dried in a vacuum oven at 40 °C for further use.

1.2.5 Preparation of 2D Magnetic Nanobeads (2D-MNBs)

The IONC were assembled into two dimensional magnetic nanobeads (2D-MNBs) by using a solution phase self-assembly method, modified from protocol established in Pellegrino's group.[120] Briefly, 30 µL of IONCs of edgelength 16±2 nm, 2.08 g_{Fe}/L in $CHCl_3$) were added into a 8-mL glass vial. Subsequently, 30 µL of stock oligo-PHA solution (2 mM in $CHCl_3$, 10 kDa) was added. By evaporating the initial solvents using a N_2 flux, the particle and polymer were re-dispersed in 200 µL of THF that freshly taken from new bottle. After sonication for 30 seconds, we have injected 1.5 mL of Milli-Q at rate of 0.5 mL/min by the fixing on an orbital shaker rotating at 420 rpm. Thus, the obtained 2D-MNBs were collected by placing the vial on a permanent magnet (0.3 T) for 5 min. Later, the product in the vial was recovered by discarding the supernatant. Finally, the obtained 2D-MNBs were promptly dispersed in 500 µL of distilled water and filtered through a 5 µM hydrophilic filter. The described method was repeated for 40 times in order to obtain enough material for the hyperthermia measurements and all reactions were merged together to reach a concentration of 2.2 g_{Fe}/L based on iron dispersed in water.

1.2.6 Water transfer of individual IONC for comparison (single NCs)

The initial $CHCl_3$ dispersed hydrophobic IONCs were transferred into water using a standard ligand exchange where the initial oleate surfactant on the surface was replaced with a nitrodopamine-PEG carboxylic terminated ligand (DOPA-PEG), which was prepared according to previously reported work.[126,127] Briefly, 1.93 mL of DOPA-PEG (1500 mw, 0.05 M, i.e. 145 mg in 1.93 mL of $CHCl_3$, 150 Lig/nm^2) and 1.93 mL of IONC (2.08 g of Fe/L, 0.22 µM) that diluted to 1 g of Fe/L were mixed together in a 40 mL glass vial. Next, 947 µL of triethylamine (TEA) was added dropwise. Then the mixture was vigorously shaken overnight under room temperature. Afterwards, the reaction mixture was transferred into a 1000 mL separation funnel, and subsequently diluted by adding 100 mL of toluene and 300 mL of Milli-Q water. After shaking it manually and stabilizing the solution for 1 h, we have extracted the lower aqueous phases carefully, which contain the transferred particles, and purged thoroughly with N_2 gas. Then the sample volume was concentrated to 20 mL by means of centrifuge, using 100-kDa centrifugal filters (Amicon filtering tube) and lastly, dialyzed for 3 days against Milli-Q

water in a cellulose membrane with a cutoff range of 50 kDa. Finally, thus water transferred IONC were concentrated to adjust iron amount to 3 g_{Fe}/L.

1.2.7 Synthesis of standard 3D Magnetic nanobeads for comparison (3D-MNBs)

The standard 3D magnetic nanobeads (3D-MNBs) for comparison were produced according to our work previously published, with minor modifications [83]. Firstly, 18 µL of the IONCs dispersion (2.08 g_{Fe}/L in $CHCl_3$) and 33 µL of poly(maleic anhydride-alt-1-octadecene) (PC18) stock (50 mM in $CHCl_3$, that correspond to monomer units) were introduced to a 8 mL glass vial. Similar to the procedure of 2D-MNBs, the organic solvent from mixture was evaporated using a N_2 flux. Subsequently, the particles and polymers were re-dissolved in 200 µL of THF and sonicated for 2 minutes. Afterwards, by fixing vial on an orbital shaker at 1250 rpm, we have injected 1.6 mL of Milli-Q water, dropwise at rate of 4 mL/min. Finally, the beads were collected by a permanent magnet (0.3 T) for 10 min and after discarding the supernatant, a brownish pellet of product was re-dispersed in 500 µL of Milli-Q water. Similar to 2D-MNBs, to scale up the amount, the same protocol was repeated at least 60 times, and merged together to reach a final concentration of 3 g_{Fe}/L.

1.2.8 Quantification of iron

We quantified the iron content in each sample through elemental analysis using an inductive plasma atomic emission spectrometer (ICP-AES, iCAP 6500, Thermo). Prior to the measurements, the 10 µL of each sample were digested overnight in Aqua Regia, which was prepared at ratio of 1:3; nitric acid to hydrochloric acid and subsequently diluted to 10 mL with water and filtered through 0.45 µM hydrophobic filter for the final analysis.

1.2.9 Dynamic light scattering

The hydrodynamic size (dH) of the nanocluster were measured using a Zetasizer Nano ZS90 (Malvern, UK), equipped with a He-Ne laser (4.0 mW) and a photodiode detector, which is operated at wavelength of 633 nm. The results were presented after averaging three consequent measurements.

1.2.10 TEM imaging

The structure and morphology of the nanostructures were investigated under transmission electron microscopy (JEOL JEM-1011), which was operated at an accelerating voltage of 100 kV. Diluted aqueous solutions of samples were deposited by drop-casting, and they were allowed to dry under room temperature for 12 hours. In addition, for the 2D-MNBs, a separate grid was prepared and stained with uranyl acetate so that it would contrast better with the polymeric shell.

1.2.11 Cryo-TEM and cryo electron tomography (CET) of 2D-MNBs

Frozen hydrated samples were prepared by applying a 3 µL aliquot of 2D-MNBs to a previously glow discharged QUANTIFOIL holey carbon grid (Cu 200 mesh 2/1, Nanovision, Italy). The grids were vitrified into liquid ethane using a FEI Vitrobot Mark IV cryo-plunger (Thermo Fisher Scientific, USA). Images of the samples were taken at cryogenic temperature (-170°C) using a Tecnai F20 microscope (Thermo Fisher Scientific, USA), equipped with a Field Emission gun operating at an acceleration voltage of 200 kV, with a US1000 Gatan CCD camera and an FEI automatic cryo box. For the CET, the tilt series were collected by tilting the vitrified sample over ±66° with the following tilt sequence: starting from 0° to ±48 with a tilt step of 3°; then from ±48° to ±66° with a tilt step of 2°. The cryo-EM imaging was carried out at a final object pixel of 3.6 Å, with a total dose of ~ 90e-/A2 in order to limit specimen damage. Computation of the tomogram was carried out with the IMOD software package using a WBP based algorithm.[128] Segmentation and 3D visualization were done using the Amira package (Thermo Fisher Scientific, USA).”

1.2.12 Magnetic accumulation experiment

In three disposable cuvettes, the 40 µg of single NCs, the 2D-MNBs and the 3D-MNBs (based on iron) were dissolved in 500 µL of Milli-Q water, that suspension contains equal amount of material. Then the each sample was exposed simultaneously to a permanent magnet of 0.3T. When solution turns transparent, the photographs of three vials were captured using a digital camera, after 80 sec for 2D-MNBs, after 120 sec in case of 3D-MNBs and after 24 hours of magnetic exposure for the single NC.

1.2.13 Magnetophoretic mobilities of 2D-MNBs

To derive the magnetophoretic velocity of the 2D-MNB and 3D-MNB samples, a magnetic attractor was used.[121] A nickel wire with a diameter of 50 µm was placed in a chamber, and it was submitted to a magnetic field of 0.2 T (which saturates the magnetization of the nano-objects). The magnetic field gradient that developed in the proximity of the wire was carefully calibrated using 1 µm beads (Dynabeads, MyOne). The individual nano-objects that were attracted to the wire were tracked when they passed through an observation window that was situated at a distance of 100 µm away from the wire extremity. At this distance, the magnetic field gradient (gradB) was 200 T/m. The migrating nanobeads' viscous drag force can be calculated using the formula $3\pi\eta dhv$ (in which η is the fluid viscosity 10^{-3} Pa·s, dh is the hydrodynamic diameter of the nanobead as measured by DLS and v is its measured velocity), and this should be equal to the magnetic force mgradB (in which m is the nanobead magnetic moment at saturation). This magnetic moment m is therefore directly inferred from the value of the velocity. Such measurements were averaged over 100 nano-objects and were repeated three times.

$$m = \frac{3\pi\eta dhv}{gradB} \qquad Equation\ 1.10$$

1.2.14 Calorimetric SAR measurements on single NCs, 2D and 3D-MNBs

The heating efficiency of water-dispersible single NCs, 2D and 3D-MNBs was evaluated by calorimetric and magnetic measurements. Calorimetry measurements were performed at different fields (range from 12-30$\mathrm{kAm^{-1}}$) and frequencies (110-300 kHz) using DM 100 Series (nanoScale Biomagnetics Corp), a commercially available instrument. For the measurements, 300 µL of an aqueous suspension of the samples (at a concentration of Fe in the range of 2.2-3 g/L) were first sonicated for 1 minute, and then they were introduced into the sample holder. Before starting the measurement, the sample temperature was recorded for 5 min until it attains a stable value. Upon the application of the alternative magnetic fields (AMF), the temperature *versus* time curves were recorded using an optic fiber thermosensor (LumaSense). The heating performance of nanostructures were quantified in terms of specific absorption rate (SAR) values by the initial slope (within the first few seconds) of the temperature *vs.* time curve using the equation below.

$$SAR\ (W/g_{Fe}) = \frac{C}{m_{Fe}} \frac{mddT}{dt} \qquad Equation\ 1.11$$

Where *C* is the specific heat capacity of water (C_{water}=4.18 $Jg^{-1}K^{-1}$), and m_{Fe} is defined as the iron mass per g of the dispersion, and m_d is the mass of the dispersion.

1.2.15 SAR of 2D-MNBs after enzymatic cleavage

We investigated the trend of SAR variations in 2D-MNBs after enzymatic cleavage as a function of the incubation time upon exposure to liver porcine esterase at 37°C. For this experiment, a frequency (*f*) of 300 kHz and a magnetic field amplitude (H) of 16 $\mathrm{kAm^{-1}}$ were the AMF parameter lies within the clinically acceptable limit (the H x *f* product was below 5 X$10^9\mathrm{Am^{-1}s^{-1}}$).[51,129] For the enzyme experiment, 300 µL of 2D-MNBs dispersed in water (2.2 $\mathrm{g_{Fe}}$/L) were incubated at a physiological temperature of 37° C with a 70-µL aliquot of the esterase enzyme that had been extracted from porcine liver(2 mg/mL and commercially available). The SAR values of the 2D-MNBs were investigated at several points of incubation from 0.25 to 48 h. The influence of the enzyme on the overall bead morphology and stability was traced using DLS and TEM.

1.2.16 AC magnetometry measurements

AC magnetometry measurements were carried out at a fixed iron concentration of 1 $\mathrm{g_{Fe}\ L^{-1}}$, using frequencies of 30 kHz, 100 kHz and 200 kHz, and a magnetic field amplitude of 24 $\mathrm{kAm^{-1}}$ at room temperatures. AC hysteresis loops were traced with a home-made inductive magnetometer based on the one described by Connord *et al.*[130] The values of AC magnetization were normalized to the mass of magnetic element (i.e. iron). AC hysteresis loop measurements consists in three repetitions to obtain an averaged and standard deviation of the magnetic area values. Afterwards, SAR values were calculated according to SAR= $A \cdot f$,[131] where *A* is the magnetic area and *f* is AC magnetic field frequency. In addition, the aggregation effects on the AC hysteresis loops were analyzed under the same conditions, with FBS volume fractions of 13 %, 55% and 27% (v/v) for single NCs, 2D and 3D MNBs respectively.

1.2.17 Cell culture

We cultured A431 epidermoid carcinoma cells (ATCC CRL-1555) in Dulbecco's Modified Eagle's Medium (DMEM, high glucose) supplemented with 10% fetal bovine serum (heat inactivated FBS), 2% penicillin−streptomycin (10000 U/mL), and 1% L-glutamine (200 mM) at 37 °C, 5% CO2, and 95% relative humidity. All of the cell culture reagents were purchased from Gibco.

1.2.18 Evaluation of 2D-MNB heat loss in tumor cells

To establish heat loss, 5 million A431 cells in 25 µL of complete media, simulating a small tumor mass, were supplemented with 2D-MNBs (50 µL 2 mgFe/mL) and an esterase enzyme solution (25 µL, 2 mg/mL). This sample was divided into two parts. In one part (50µL, sample named A431+2D-MNBs_no incubation), the AC hysteresis loop (at 300KHz and 16 kA/m) or the magnetic hyperthermia (MH) treatment was immediately performed (at a frequency of 300 kHz and a magnetic field intensity of 16 kA/m for three cycles of 30 minutes each with a 5 minutes break in between each cycle). The second part (50 µL) was incubated for 3h at 37° C to enable the enzymatic digestion of the polymer (the 'A431+2D-MNBs_3h-incubation' sample). Soon after the incubation, the AC hysterics loops were measured at 300 kHz and 16 kA/m on an AC magnetometer.

1.2.19 In vitro magnetic hyperthermia treatment and cytotoxicity assay

A431 cells ($5*10^6$ cells in 25 µL of complete media) were supplemented with 50 µL of 2D-MNBs (2 g_{Fe}/L) and with 25 µL of esterase enzyme (2 g/L) as a cleaving agent for 2D-MNBs. This sample was divided into two parts: one part was immediately exposed to alternative magnetic fields of 300 kHz and 16 kA/m (3 cycles of 30 min each) using an MH setup (DM100 series, nanoScale Biomagnetics). The second part was first incubated for 3 h at 37° C, and then it was exposed to MH treatment. After the MH treatment, the cells were re-seeded on 12-multiwell plates ($2.5*10^6$ cells/well), and the cell viability was assessed by trypan blue assay 24 and 48 hours post MH treatment. The first control group consisted of: i) cells ($5*10^6$ cells/well) treated with porcine esterase in the cell culture medium maintained at room temperature for 100 min (equivalent time needed for MH treatment) (t_0) before being re-seeded for the evaluation of cell viability at 24 and 48h (not added with 2D-MNBs and no magnetic hyperthermia cycles) ii) cells ($2.5*10^6$ cells) treated only with porcine esterase (no 2D-MNBs, no MH) incubated at 37°C for 3h (t_{3h}). After the time of incubation, they were maintained at room

temperature for 100 min (t_{3h}) before re-seeding them. The second group consisted of cells treated with 2D-MNBs, porcine esterase (but no magnetic hyperthermia cycles) and maintained at room temperature for 100 min (t_0, $2.5*10^6$ cells) before re-seeding. Also in this group cells (t_{3h}, $2.5*10^6$ cells) were treated with 2D-MNBs and porcine esterase (with no exposure to MH) and then incubated for 3 hours at 37° (t_{3h}). After this incubation time the cells were maintained at room temperature for 100 minutes before being re-seeded for cell viability assay. The third group consisted of cells treated with 2D-MNBs and porcine esterase which were then exposed to MH. For these groups, we have considered a first group that consisted of cells mixed with 2D-MNBs and porcine esterase and directly exposed to MH ($2.5*10^6$ cells). While for the other group (t_{3h}) the cells were mixed with 2D-MNBs and porcine esterase, incubated at 37°C for 3h and only after incubation, they were exposed to MH treatment.

1.2.20 Synthesis of Core-shell IONC

The synthesis of core−shell iron oxide nanocubes; FeO/Fe_3O_4 NPs (Cs-IONCs) of edge length of 18±2 nm was modified from recently published work.[132,133] Briefly, in this a typical synthesis, 1.6 g of oleic acid (5.7 mmol), 0.939 g of sodium oleate (3 mmol), and 5 mL of 1-ODE were introduced into three-neck flask (50 mL) equipped with reflux condenser that degassed at 90°C for 30 min. Subsequently, we cooled the solution temperature to 60 °C that is maintained under N_2 reflux. Later on, after injecting 0.597g of Fe(CO)5, the precursor solution (3 mmol) was dissolved in 1 mL of 1-ODE), then heated the reaction mixture up to 320 °C in span of 20 min. Under vigorous stirring, the solution turns blacks, and as the nucleation process starts where the reaction was continued for another 1.5 h at 320°C. After cooling down to the room temperature, the core-shell IONCs were centrifuged for 10 min at 8000 rpm and washed using solvent fraction of chloroform/methanol/acetone (1:6:1) for three times and dispersed them finally in $CHCl_3$.

1.2.21 Controlled clustering of Core-shell IONC

The Cs-IONCs of edge length 18±2nm were clustered in a controlled manners into three different morphologies; single NCs (SC), Dimers/Trimer (Di/tri) and centrosymmetric structures/Bigger clusters (BC), using commercially available polymer poly(styrene-co-maleic anhydride), cumene-terminated (PScMA, Mn=1600 g/mol, PScMA). Here we have exploited the amount of polymer chains per nanometer square as main parameters to obtain desired geometry of the assembly.

Briefly, for bigger clusters, to 9 mL of THF in 20 mL glass vial, we have added 500 µL of stock solution of PScMA (2.19 mM in THF), for dimers/trimers, 250 µL PScMA, to 9.75 mL of THF. Instead, for single NCs, 250 µL of PScMA was added to 9.85 mL of THF. Then, a fine dispersion of 35 µL of Cs-IONCs solution ([Fe] = 10.09 g/L in $CHCl_3$) was introduced and subsequently sonicated for 3 min. Then, by moving reaction mixture to an ice bath of 10°C, while it is sonicating, we have injected 1 mL of H_2O at the rate of 0.5 mL/min using a syringe pump. Following this, organic solvent from the reaction mixture was evaporated slowly, overnight, under room temperature, by placing them uncapped on a horizontal shaker shaking at 100 rpm. Next day, when the solution level reached to 1 mL, where particles are supposed to remain in water, the mixture has been transferred to 2 mL Eppendorf containing 1 mL of $CHCl_3$. After shaking the mixture vigorously by hand, we kept the two phases which were separated (water and $CHCl_3$) undisturbed for 3 hours. The upper water phase with particles, when it becomes clear and turbid free as presented in Figure 1.12, was transferred into a 1 mL glass vial. The unreacted, excess polymer remain in the interface and lower $CHCl_3$ phase can be discarded as this process was introduced for washing.

Figure 1.12. A photograph of sample under washing. The upper dark water phase composed of nanoclusters, which is indicative for their water transfer. The unreactive polymer can be identified at the interface as dense whitish substance (red arrow). While the lower clear solution is $CHCl_3$ phase.

The samples for TEM characterization and dynamic light scattering and elemental analysis was performed through similar approach, as described in section 1.2.9 and 1.2.10.

1.3 Results and Discussion

With the clear goal of identifying the most suitable materials for magnetic hyperthermia, the development of assembly protocols of magnetic nanoparticles into structured architectures has recently gained specific attention in the scientific community.[62,134,135] The focus of this research is on understanding how the heat efficiencies and thus SAR values change when MNPs are arranged in well-defined structured geometries. For this, we have exploited the effect on two different iron oxide nanocubes that clustered through different strategies. 1) High interacting iron oxide nanocubes. 2) Less interacting core-shell iron oxide nanocubes.

From here, the discussion will be divided into two distinct subtitles.

- Esterase cleavable 2D assemblies of magnetic iron oxide nanocubes: exploiting enzymatic polymer disassembling to improve magnetic hyperthermia heat losses.
- Anisomeric assembling of core-shell iron oxide nanocubes for improved hyperthermia.

Esterase cleavable 2D assemblies of magnetic iron Oxide nanocubes: exploiting enzymatic polymer disassembling to improve magnetic hyperthermia heat losses.

1.3.1 Preparation of 2D Magnetic Nanobeads (2D-MNBs)

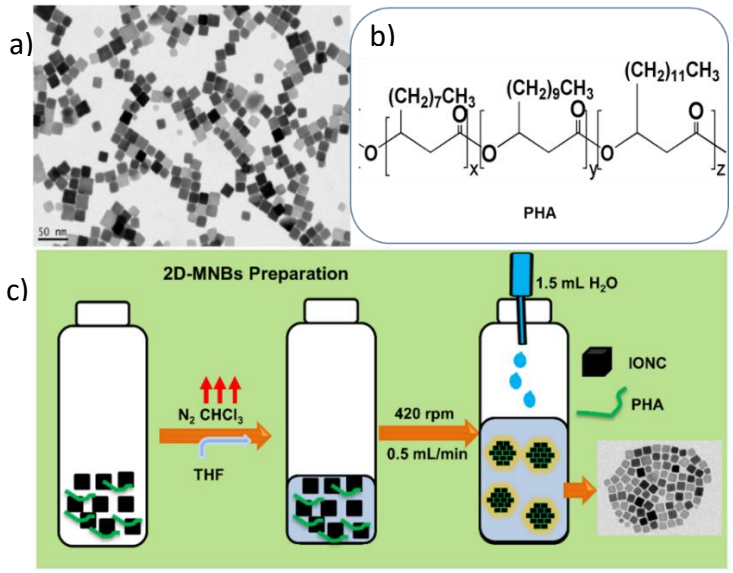

Figure 1. 13. Preparation of water soluble 2D-MNBs: a) TEM image of the initial iron oxide nanocubes (IONC) dispersed in chloroform with an edge length of 15.9±2.0 nm. b) Chemical structure of oligo-polyhydroxyalkanoates. c) Schematic representation of the protocol to prepare 2D-MNBs. Reprinted with permission of reference(125) Copyright © 2019, American Chemical Society.

As presented in Figure 13a, we have established a protocol to assemble IONCs into two dimensional nanostructures named as 2D magnetic nanobeads (2D-MNBs) using a biodegradable oligo-PHA processed from a bacteria, with a molecular weight of 10kDa. Initially, a dispersion of IONCs in chloroform (with a cubic length of 16±2 nm, Figure 13.b) were mixed together with the oligo-PHA solution in chloroform (2 mM). After complete evaporation of the chloroform solvent, we added fresh THF solution. The ratio of polymer added was estimated to be as 7 polymer chains per nm^2 of the nanocube surface. Then, a 30 second sonication step assisted to homogenize the dispersion of the materials. Later, on orbital shaker, under mild shaking conditions that was 420 rpm, 1.5 mL of Milli-Q water (0.5 mL/min) was added dropwise as an anti-solvent.

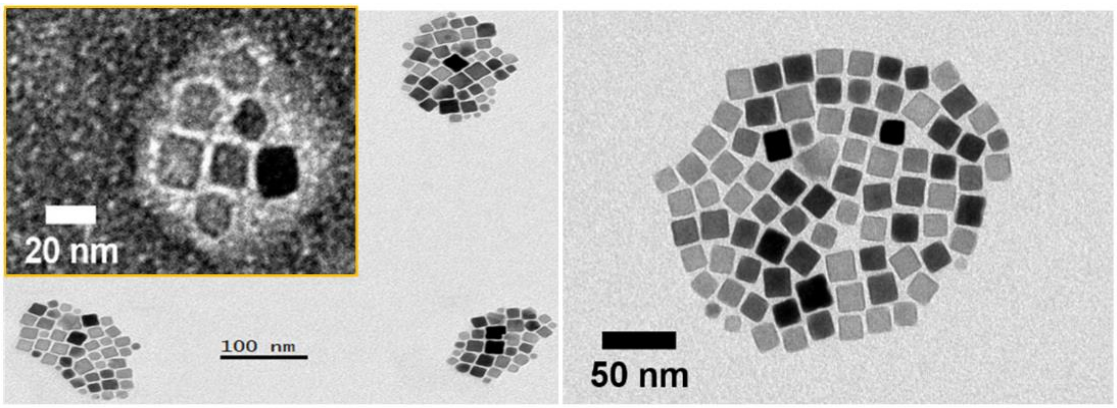

Figure 1.14. TEM images of 2D-MNBs dispersed in water, obtained after drying under room temperature. The inset, high magnification image, in left panel obtained after staining the grid with uranyl acetate in order to stain the polymer, where bright shadow around nanocubes corresponds to oligo-PHA. Reprinted with permission of reference[125] Copyright © 2019, American Chemical Society.

The polarity change occurs because of injecting water to THF which contains the PHA polymer and the IONCs, which promotes conformational re-arrangement of oligo-PHA and a controlled precipitation of the nanocubes where the alkyl chains of the polymer intercalate with the hydrophobic ligand caps of IONCs, producing an orderly 2D pattern of nanocubes as picturized in Figure 1.14 by TEM characterization.

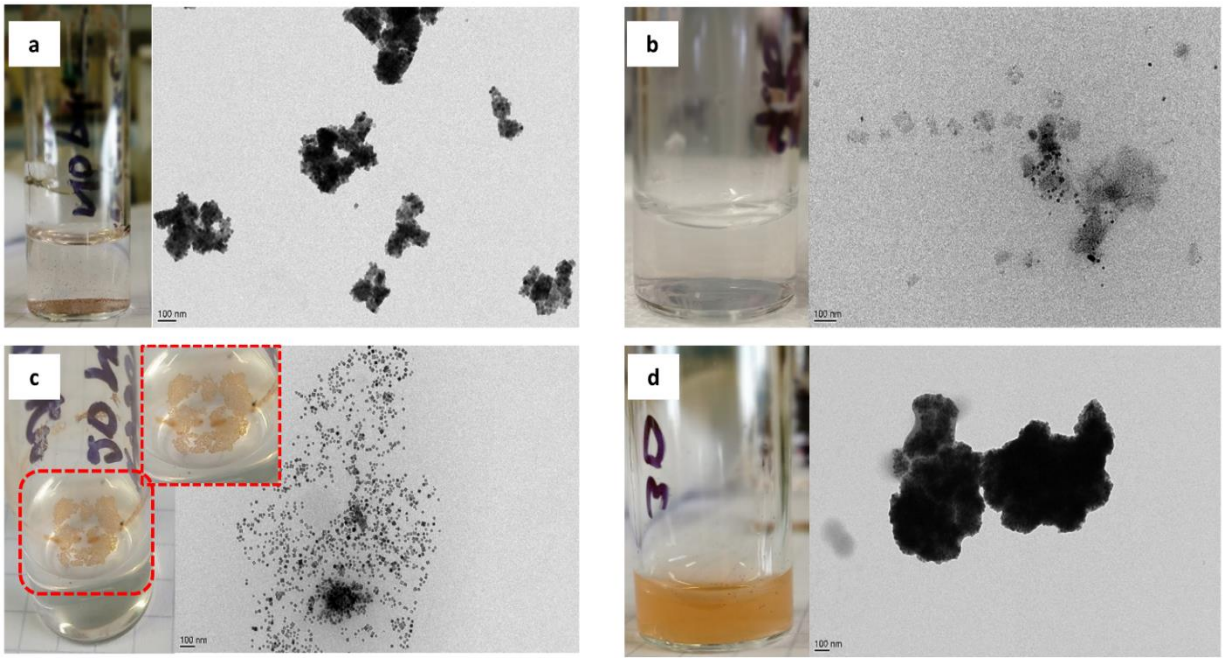

Figure 1. 15. Control experiments elucidating the 2D-MNBs clustering formation. a) Control reaction 1 obtained by applying the standard 2D-MNBs protocol only in presence of IONCs and in absence of PHA polymer. In this case the IONCs form large and irregular aggregates that precipitate out from the solution. b) Control reaction 2 obtained by applying the standard 2D-MNBs protocol in presence of only PHA polymer and in absence of IONCs. The polymer solution looks slightly milky at the end of the protocol and some flake-like structures of polymer are clearly visible on a TEM grid, indicating the precipitation of the PHA amphiphilic polymer under the working conditions. c) Control reaction 3 obtained by applying the 2D-MNBs protocol but when using increased shaking speed (1250 rpm) and water addition rates (4 mL/min) rather than standard conditions (420 rpm shaking and water addition rate at 0.5 mL/min). In this case large flakes of brown materials are floating in the vials and under TEM they correspond to irregular, disordered and large IONC structures. This experiment suggests that the low addition rate is a key parameter to control the ordered precipitation and assembly of IONCs in 2D-MNBs. d) Control reaction 4 obtained by applying the standard 2D-MNBs protocol (shaking at 420 rpm and water addition rate at 0.5 mL/min) but using PC-18 polymer rather than PHA polymer. In this case irregular 3D-MNBs are obtained rather than 2D-MNBs. This experiments suggests that the PHA, rather than the PC-18, is specifically driven the formation of 2D-MNBs. Reprinted with permission of reference(125) Copyright © 2019, American Chemical Society.

We have carefully examined the optimal parameters to obtain 2D-MNBs, through control experiments and confirmed the importance of oligo-PHA as a directing templet to induce the 2D-ordering of IONCs, as presented Figure 1.15. Indeed, when 2D-MNBs protocol was repeated in the absence of oligo-PHA polymers, that was only in the presence of IONCs, resulted in formation of large, unstable, deformed 3D aggregates (Figure 1.15a). On contrary, this time by repeating the protocol in the presence of only oligo-PHA (i.e. with no IONCs in the solution) the resulted solution was opaque as it contains some flake-like polymer structures (Figure. 1.15b).

Instead, we have also identified that the rate at which anti-solvent (water) was added to the THF polymer-IONCs mixture is extremely important to control 2D-MNBs assemblies. To emphasize, when the 2D-MNB production was performed at higher addition rate such as 4 mL/min and 1250 rpm shaking speed rather than 0.5 mL/min (the standard rate used for 2D-MNBs), it created insoluble, floating flakes which contained very large and irregular IONC structures, as shown in TEM of figure 1.15c. Here the polymer PHA is extremely important to drive, 2D assembly. For instance, when the standard 2D-MNB protocol was implemented with poly (maleic anhydride-alt-1-octadecene) instead of oligo-PHA, the final water-soluble structures were identified to be very large and 3D ordered (Figure 1.15d). In overall, these important findings from control experiment highlights the key role of oligo-PHA in driving the 2D assembly of IONCs . In addition, it also demonstrate that it is extremely important to maintain low water addition rate to form 2D- assemblies. Here, as mentioned by Zhang, N. *et al*, we hypothesized that the linearity,[136] and amphiphilic properties of the oligo-PHA, in combination to our working parameters promote bidimensional self-assembling of IONCs.[137] Thanks to the rapid response of the 2D-MNBs (80 seconds) to a permanent magnet (0.3 T), due to which the cleaning steps were easy and quick enough to remove any excess of the oligo-PHA. The black pellets were attracted to the magnet, and the supernatant was discarded with a final pellet re-dispersion in Milli-Q water.

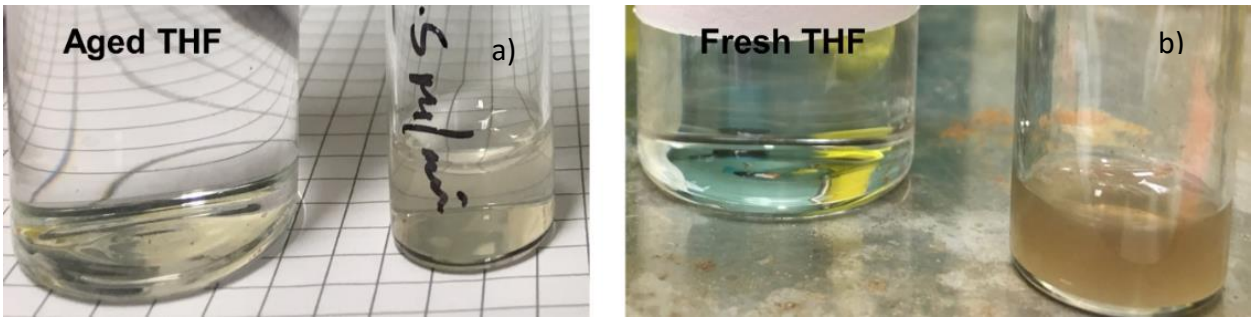

Figure 1.16. Digital image representing the difference in yield using same protocol, produced with two different THFs. The image on the left corresponds to the method using an aged THF (bottle expose to air). Please note that with this THF most of the sample precipitate. The image on the right uses a fresh bottle of THF. The brownish color of the solution demonstrates the success of the protocol. Reprinted with permission of reference(125) Copyright © 2019, American Chemical Society.

It is worthy to state that the reproducibility of the 2D-MNBs was affected by the quality of THF, as presented in pictures of Figure 1.16. Indeed, when we synthesized 2D-MNBs using THF from freshly opened bottle, the fraction of 2D-MNBs were major (Figure 1.16b), while a subsequent reaction with THF from bottle opened before 45 days, produced aggregates; Figure 1.16a (note: THF was aged and

kept outside the glove box, minor traces of impurities were noted in NMR, data not presented). This was not the case when we prepared 3D-MNBs using the same batches of nanocubes and an amphiphilic polymer namely poly(maleic anhydride-alt-1-octadecene) (PC18) following our previously developed protocol (Figure 1d).[83,120] Our assumption was that, wetting behavior of IONCs with oligo-PHA could be different from IONCs with PC18 and instead IONCs-oligo-PHA interactions could be much sensitive to humidity than in the case of PC18 for making 3D-MNBs.

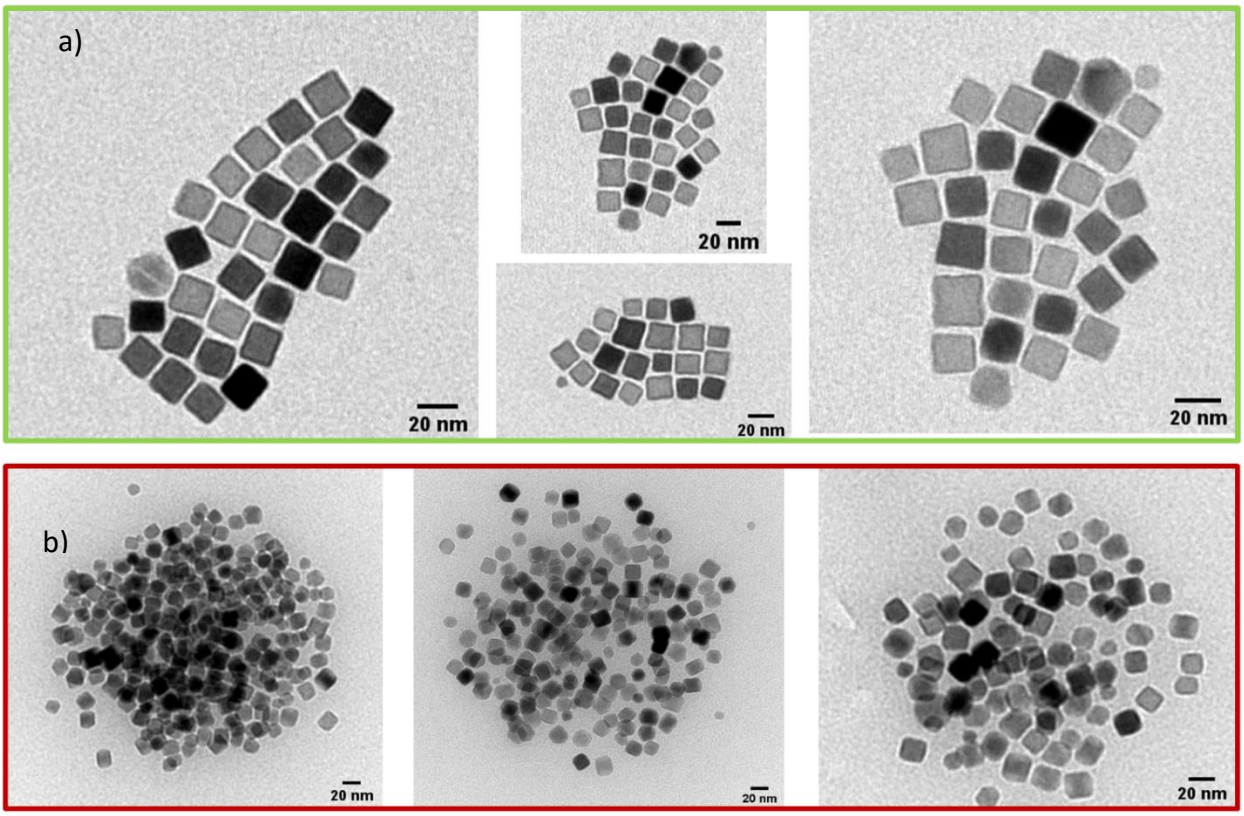

Figure 1.17. TEM images of 2D assemblies defining the role of IONCs shape anisotropy in clustering. a) The 2D-MNBs in green panel produced from monodispersed IONC (16.0±1.8 nm, statistics taken by measuring 230 particles) showing a defined 2D alignment. b) While, one in red panel beads produced under identical conditions, form another batch of IONCs of same size (16.0±2.7) with improper cubic shape. Reprinted with permission of reference(125) Copyright © 2019, American Chemical Society.

As another factor, the choice of cubic shape MNPs have predominant effect on the final ordering of 2D-MNBs. To emphasize as Figure 1.17 presents, we have repeated 2D-MNBs protocol by using two different IONCs; one with a more regular shape and a cube edge of 16.0±1.8 nm and another with IONCs of irregular shape (16.0±2.7 nm). Though the both resulting assemblies, still had a bidimensional

arrangement, however, imperfect ordering had realized for protocol with irregular shape IONCs (Figure 1.17b, in red) and this highlights that the face-to-face cube interaction should be favored in regard to form proper 2D-MNBs (Figure 1.17a, in green).

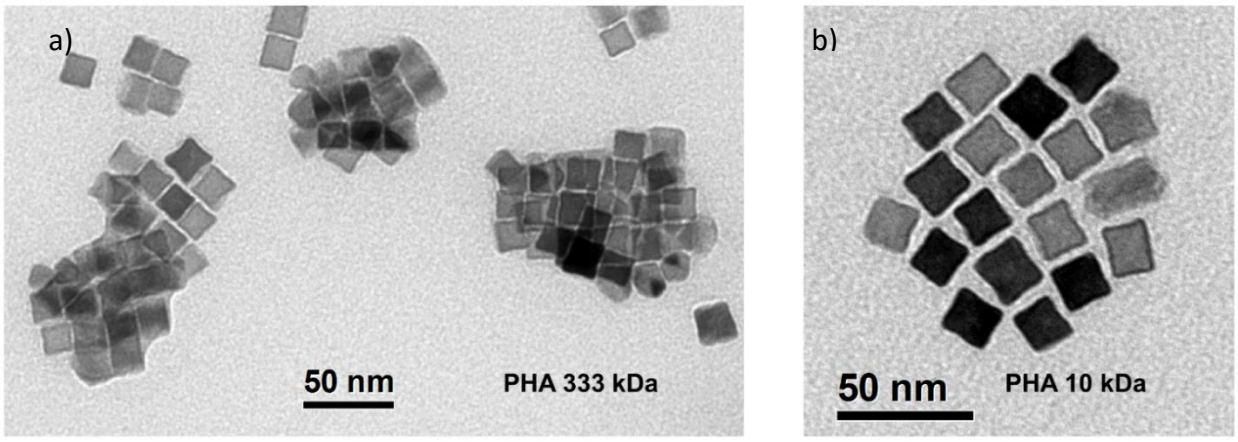

Figure 1.18. TEM images of assembling of IONCs, produced under similar conditions, using polyhydroxyalkonate of two different molecular weights. The image on the left is produced from mcl-PHA of 333 kDa polymer, which yields multiple layers of 2D packed nanocubes in a sort of 3D assemblies. The image on the right is from 10 kDa oligo-PHA derived a monolayer of 2D arranged of water-soluble structures. Reprinted with permission of reference(125) Copyright © 2019, American Chemical Society.

We have also investigated the significance of molecular weight of PHA in 2D-MNBs production. Prior to using the 10 kDa polymer, few preliminary attempts were given using a larger molecular weight native mcl-PHA; ca. 333 kDa. In fact, such a high molecular weight polymer, produced aqueous unstable 3D clusters (Figure 1.18a) rather being 2D clusters (Figure 1.18b). The consequence can explained by the fact that, polymers of larger molecular weight have poorer solubility in THF than that of short range oligo-PHA. This affect the level of interactions of the polymer with the IONCs and thus alters the geometry of the clusters and tend to collapse randomly and rapidly in presence of nanocubes, as a consequence forms 3D clusters.

In addition, overall TEM images also suggest that 2D-MNBs contain IONCs with constant spatial distance between particles within the structure, but this was not the case for 3D-MNBs, where the IONCs are densely and randomly packed (Figure 1.21).

1.3.2 Cryo-TEM and cryo electron tomography (CET) of 2D-MNBs

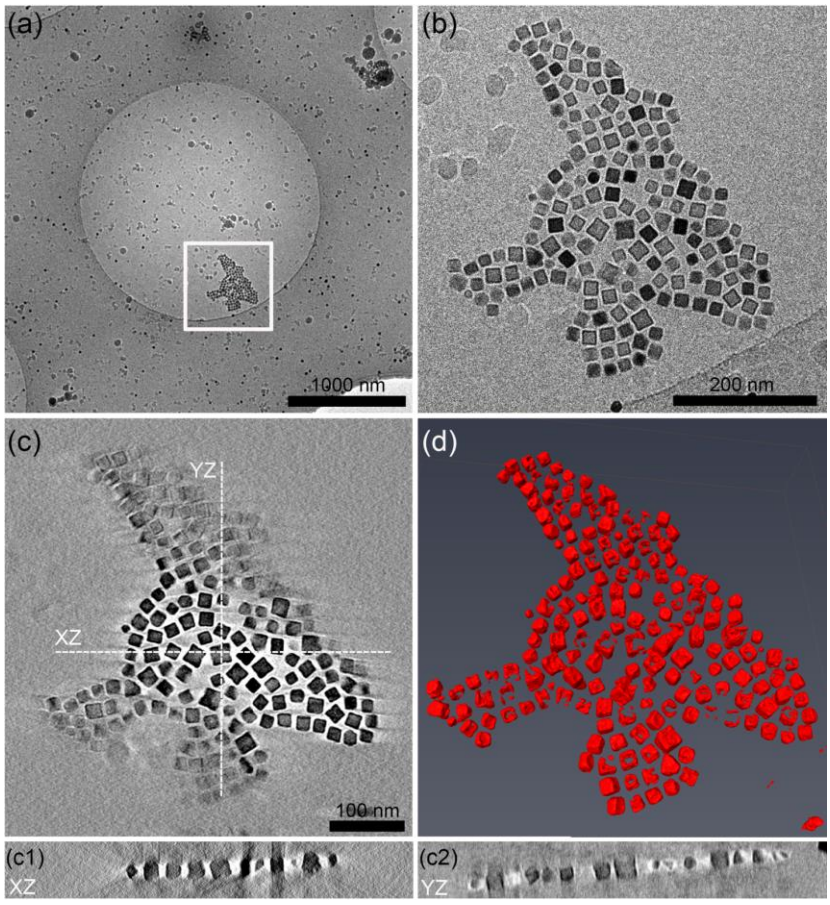

Figure 1. 19. ***Cryo-TEM and cryo electron tomography****. a) A low magnification projection cryo-TEM image of a vitrified 2D assembly. b) A higher magnification of the region outlined in (a). c) XY CET tomographic averaged slice (n=10) of the 2D assembly shown in (a) and (b). (c1) and (c2) are XZ and YZ slices sections respectively (n=10) of the tomogram in (c). d) A reconstructed 3D model from the tomogram in (c). These data confirm the presence of 2D-MNBs in the solution, forming a clear bi-dimensional monolayer assembly of IONCs. Reprinted with permission of reference[125] Copyright © 2019, American Chemical Society.*

In order to confirm the two dimensional geometry of 2D-MNBs in solution and minimize the artifact affect coming from conventional TEM, we characterized the 2D-MNBs in their solution by cryo-TEM. The analysis was performed on a vitrified sample clearly showed the presence of bi-dimensionally ordered nanocube assemblies in their fully hydrated state (Figure 1.19 a and b). We performed cryo-electron tomography (CET) to further investigate the geometry of these assemblies. The CET analysis explicitly revealed that the 2D-MNBs in solution were organized in a monolayer of IONCs with a well-ordered 2D assembly (see Figure 1.19c and d).

1.3.3 Water transfer of individual IONCs and preparation of 3D-MNBs for comparison

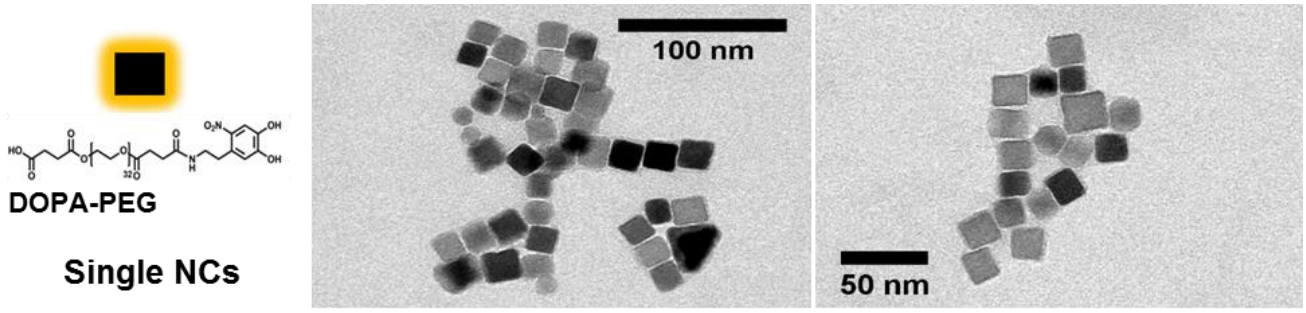

Figure 1.20. TEM images of water transferred single cubes (single NCs), which were obtained by means of the ligand exchange method using the same batch of nanocubes. Reprinted with permission of reference(125) Copyright © 2019, American Chemical Society.

To compare the MH efficiency of the 2D-MNBs, we have considered another two sample individual nanocubes (Single NCs) and three dimensional nanobeads (3D-MNBs) using same batch of nanocubes that we utilized for 2D-MNBs. For Single NCs, we transferred IONCs into water through a standard ligand exchange approach by using DOPA-PEG as stabilizing molecule.[103] Figure 1.20 given the view of sample after water transfer. The grouping of IONCs on TEM sample grid was purely a drying effect that can be justified by comparing DLS result, which we will present later.

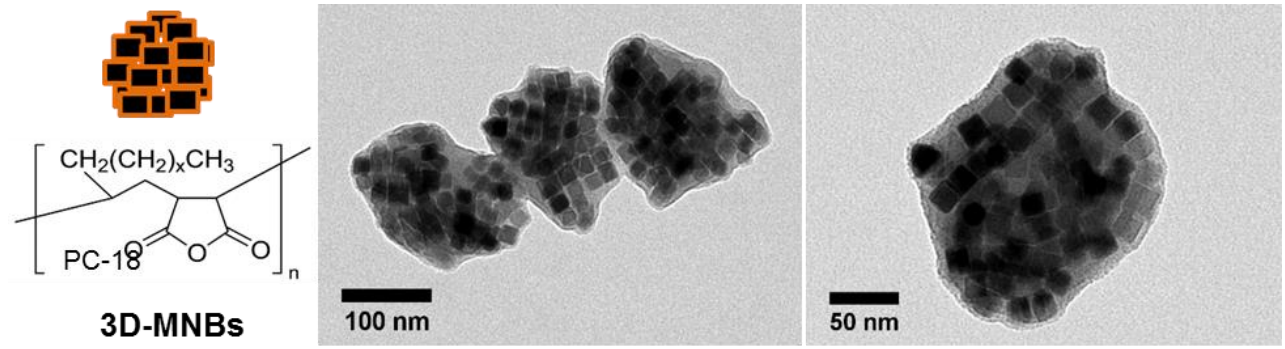

Figure 1.21. TEM images of three dimensional magnetic nanobeads (3D MNBs), produced from the same batch of IONC, using an amphiphilic polymer PC18 for comparison purpose to 2D-MNBs. Reprinted with permission of reference(125) Copyright © 2019, American Chemical Society.

We prepared 3D-MNBs using the same batches of nanocubes and an amphiphilic polymer namely poly(maleic anhydride-alt-1-octadecene) (PC18, 30-50 kDa) following our previously developed protocol (Figure 1.21).[83,120] Just to note, here we are not addressing the synthesis details of both these modalities because it has been widely discussed in previous studies.

1.3.4 Hydrodynamic size of three morphologies

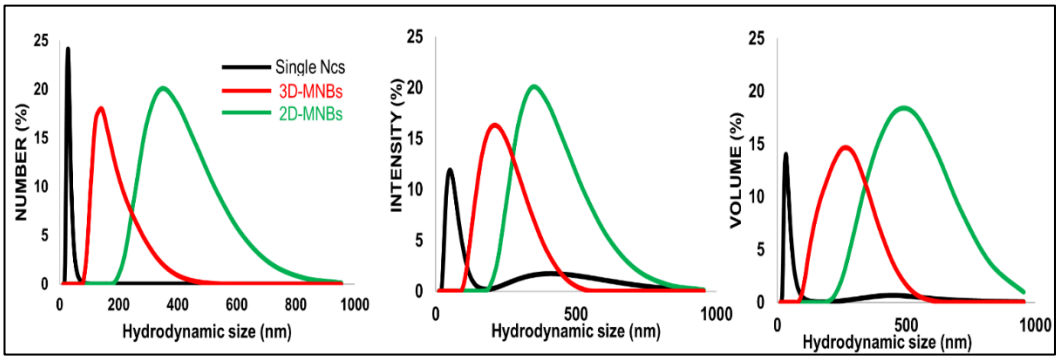

Sample	Number	Intensity	Volume	PDI
	d.nm	d.nm	d.nm	
Single Ncs	30±8	57±24	39±14	0.344
2D-MNBs	393±117	452±129	495±148	0.074
3D-MNBs	171±64	227±76	250±91	0.101

Figure 1.22. Comparative size distribution: Mean hydrodynamic size of single NCs (black curve), 2D-MNBs (green curve) and 3D-MNBs(red curve), dissolved in water weighed by number, intensity and volume percentage. In table, the summary of average hydrodynamic sizes of all three structures (i.e. single NCs, 2D-MNBs and 3D-MNBs) in water, as measured by DLS. Reprinted with permission of reference[125] Copyright © 2019, American Chemical Society.

As presented in Figure 1.22, the mean hydrodynamic diameters (dH) of 2D-MNBs, 3D-MNBs and Single NCs were determined as 393±117, 171±64 nm and 30±8 nm (DLS size weighted by number percent) respectively. In addition, narrow PDI values implies their good colloidal stability and no clustering in water dispersion (table in Figure 1.22). In fact, the reported dH values were larger than that of TEM size core because DLS considers and includes the hydrated polymer range.

1.3.5 Calorimetric SAR measurements on single NCs, 2D and 3D-MNBs

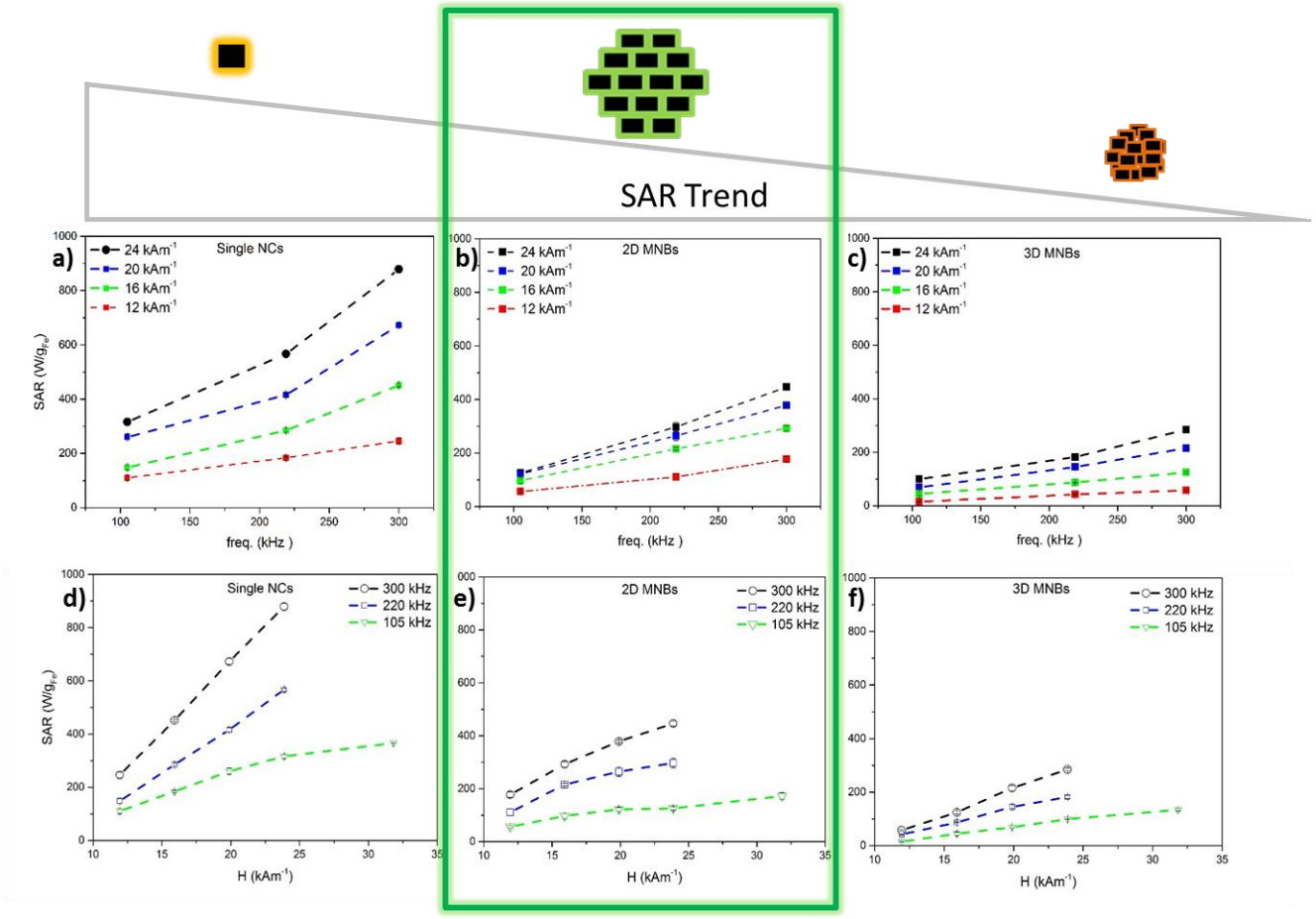

Figure 1.23. ***SAR values of single IONCs, 2D-MNBs and 3D-MNBs in water****:- a-c) Field frequency dependence of SAR values (W/g_{Fe}) for Single NCs, 2D-MNBs and 3D-MNBs for different field amplitudes in the range from 12 to 24 kAm^{-1}. d-e) Field intensity dependence of SAR values for single NCs, 2D-MNBs and 3D-MNBs at different field frequencies (105, 220 and 300 kHz). The green frame highlights the novel 2D structures developed in this work. Reprinted with permission of reference(125) Copyright © 2019, American Chemical Society.*

Figure 1.23 compares the SAR values of 2D-MNBs, with single NCs, and 3D-MNBs dispersed in water, derived through calorimetric analysis at different field conditions and at fixed iron concentration of 3 g_{Fe}/L. As we can see, in first glance, the SAR values were differing among the assemblies, showing predominant reduction from single NCs to 2D-MNBs, and much significant for 3D-MNBs. This highlights the correlation between SAR values and MNP clustering geometry. In fact, the 2D-MNBs exhibited lower SAR values than single IONCs, however, almost double to those of 3D-MNBs and the trend has been preserved for all the applied field conditions (Figure 1.23).

For example, at 300 kHz and 24 $\mathrm{kAm^{-1}}$, 2D-MNBs have given a SAR value of 443 ± 9 W/g, which is 30% greater than the one obtained for 3D-MNBs (284±5 W/g) and 50% lower to the SAR of single NCs. Such an effect of clustering on the SAR can be understood in terms of their varied magnetic dipolar interactions.[122,134] In 2D-MNB, the spatial order of IONCs into the cluster and the constant interparticle distance minimize magnetic dipolar interactions, resulting in SAR values that are closer to that of single IONCs (see the TEM image in Figure 1.20). While in case of 3D-MNBs the IONCs within cluster are randomly oriented and closely packed which causes significant demagnetization effects, that directly reduce the SAR performance.[83,84,138]

1.3.6 AC magnetometry measurements.

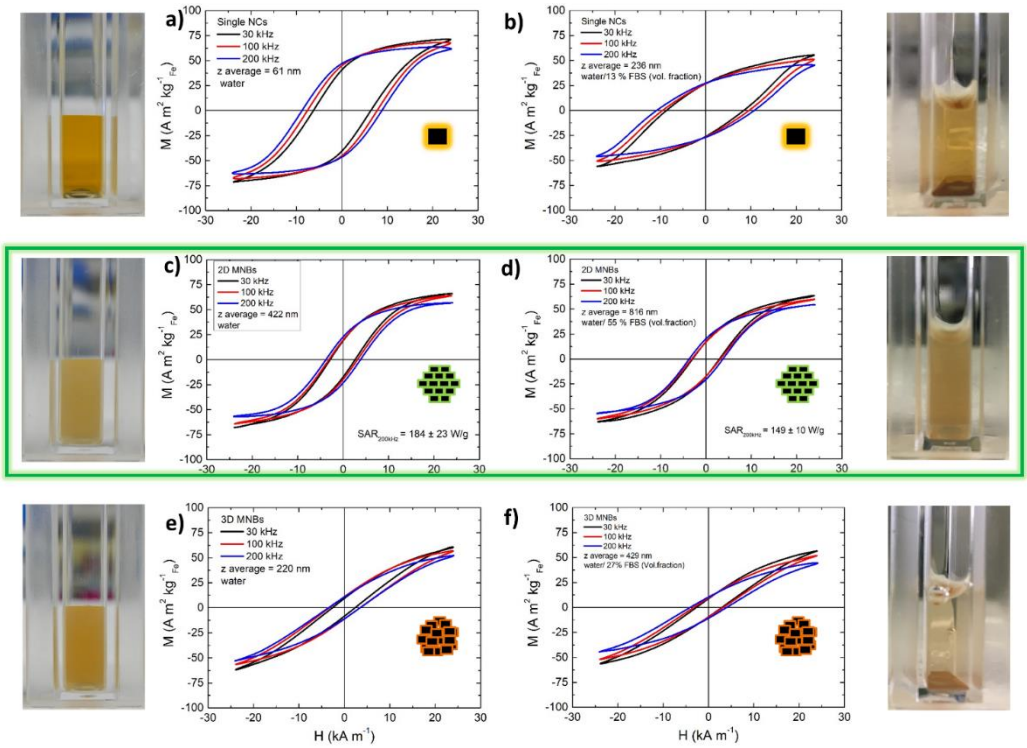

SAMPLE	30 kHz	100 kHz	200 kHz
1 g_{Fe} L^{-1} in water		24 kAm^{-1}	
Single Ncs	63±4	238±17	501±69
2D-MNBs	22±4	81±16	184±24
3D-MNBs	17±2	76±6	138±10

Figure 1.24. AC Hysteresis loops of single NCs, 2D-MNBs and 3D-MNBss in water (left panels) and in FBS (right panels) at different frequencies. a) ac hysteresis loops of single NCs dispersed in water. b) ac hysteresis loops of single NCs dispersed in an aqueous 13% FBS solution. c) AC hysteresis loops of 2D-MNBs dispersed in water and, d) in aqueous 55% FBS solution, e) ac hysteresis loops of 3D-MNBs dispersed in water and, f) 3D-MNBs in aqueous 27% FBS solution. The images on the left and right panels correspond to the assemblies dispersed in water (left) and in the corresponding FBS (right) solutions. The Table gives SAR data measured by AC magnetometry considering the hysteresis loops by considering SAR = A·f,[131] shown in Figure 1.24. Reprinted with permission of reference[125] Copyright © 2019, American Chemical Society.

In order to complement the SAR results of the calorimetric characterization, we have conducted the ac magnetometry analysis on three samples at an identical iron concentrations of $1 g_{Fe}/L$, whose field conditions ranges between 30 and 200 kHz. The Figure 1.24 demonstrates ac hysteresis loops of the three distinct dispersed assemblies in aqueous and in fetal bovine serum (FBS) diluted solutions. As observed, in water, the hysteresis loop of single NCs have larger magnetization and area values under

maximum field in comparison to 2D-MNBs. However, the latter show similar magnetization values, but larger loop area than 3D-MNBs. Considering SAR = A·f,[131] similar to calorimetric, the resulted magnetic losses are gradually reduced from single NCs to 2D-MNBs and then to 3D-MNBs. Corresponding values were given in table of Figure 1.24.

The addition of FBS induced intentional aggregation that would somehow mimic the conditions of real cellular environment.[58,139] The occurrence of aggregation in FBS was confirmed by DLS measurements, whose initial dH values (z-average values) shifted towards higher ranges, that was the case happened in all the three samples, those values are presented within corresponding plots in Figure 1.24. Besides different hydrodynamic values, images presented in the right and left panels of Figure 1.24 directly demonstrates the colloidal stability of the assemblies before and after the addition of FBS. What is actually remarkable for 2D-MNBs, the hysteresis loop area/shape/magnetization remained almost unaltered when the said size was doubled from 422 nm to 816 nm (compare Figure 1.24 c&d, green panels). Conversely, the single-NC and the 3D-MNB structures precipitate when the dH is increased, but AC hysteresis loops (shape and area) of only single NCs exhibit significant variations and however not a much change for the 3D-MNBs. This can be explained as, when assembly aggregates, the magnetic dipolar interactions boosts. Hence, the AC hysteresis loops are strongly affected by the aggregation of single NCs (i.e. larger hydrodynamic size, stronger dipolar interaction). Whereas for 3D-MNBs the random interparticle distance is already frozen per cluster in spite of their aggregation, doesn't influence the same. While the observation of 2D-MNBs is that the aggregation of individual clusters does not change the AC hysteresis due to the fact of their quite unexpected planar MNP spatial configuration. The latter could explain that in the particular case of magnetic planar arrangement of individual MNPs, magnetic moments result in no significant interacting effects between 2D-MNBs.

For the 2D-MNBs, in addition to the limited variation by AC dynamic hysteresis loop area/shape/ magnetization at maximum field, it also corresponds to a limited reduction of SAR at 200 kHz from the water-dispersed state (184±23 W/g) to FBS (149±10 W/g). This experimental evidence confirms aggregation independent behavior of the 2D-MNBs (Figure 1.24.c&d). This feature is extremely important because most of the reported nanoclusters exhibited significant shrink in their magnetic losses which drastically cause reduction in magnetic heat performances, if the aggregation increases, thus limiting their application for magnetic hyperthermia performance in a cellular environment.[58,140]

1.3.7 SAR of 2D-MNBs after enzymatic cleavage

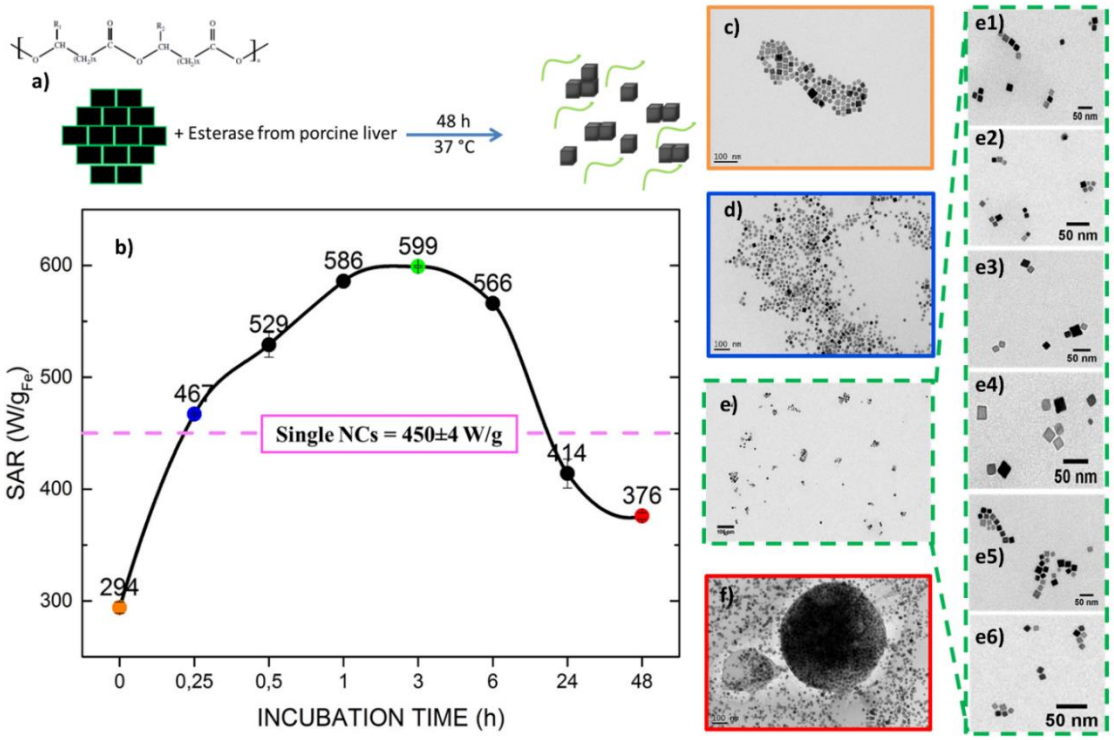

Figure 1.25. ***SAR values of 2D-MNBs exposed to esterase enzymes at different incubation times.*** *a) Graphical representation of the esterase mediated cleavage of 2D-MNBs (300 µL, 2.2 g_{Fe}/L), incubated at 37 °C. b) The plot defines the variation in the SAR as a function of incubation time with esterase, measured at 300 kHz, 16 kAm^{-1} (which is below the biologically acceptable limit $H_f = 5\ X10^9 Am^{-1}s^{-1}$). The horizontal dashed line corresponds to the SAR value of single IONCs (450±4 W/g). The TEM images on the right panel indicate the structural morphology of cleaved 2D-MNBs at different time points of incubation including, c) 0 h (before the addition of enzyme, highlighted in orange), d) 0.25 h (blue), e) 3 h (green) and f) 48 h (red). Additional images, framed in green (e1-e6), correspond to the sample at 3 h. At this time point, small chains of nanocubes appeared, which may explain how the highest SAR recorded was achieved, owing to their unique structural arrangements. Reprinted with permission of reference(125) Copyright © 2019, American Chemical Society.*

In order to show the effects of spatial distribution on the SAR performance of 2D-MNBs, we have taken advantage of biodegradable properties of oligo-PHA polymers and exploited them by exposing to lytic enzymes. Accordingly, we treated the 2D-MNBs with a porcine derived esterase enzyme and incubated at 37°C for 48 hours and monitored the SAR at different times point over this 48h as schematized in Figure 1.25a). Off note, we have chosen the magnetic excitation field ranges that lies within the biological acceptable limits, whose H*f* factor was 4.8 ˣ 10^9 $Am^{-1}.s^{-1}$. Surprisingly, the SAR values what we have recorded within the first three hours of incubation dramatically increased (almost doubled)

with a corresponding SAR value of 599±1 W/g with respect to that of initial 2D-MNBs whose SAR=294±5 W/g. If we note, the increase of SAR in 3 hours of exposure to esterase was even more than that of single NCs; 450±4 W/g (marked as pink line in Figure 1.25b). However at longer incubation times, the SAR began to decrease progressively upto 48 h but the value was never less than the initial value of 294 W/g (Figure 1.25b).

Attributing to these outcomes, we investigated systematically the structural changes happened in 2D-MNBs in response to esterase enzyme, at different incubation time points. As shown in Figure 1.25d, after 15 min of enzyme treatment, the structures already began to lose their 2D shape, and moreover, the spatial distributions of IONCs on the grids appeared similar to those of Single NCs. Interestingly, even the corresponding SAR value (467±1 W/g) at 15 minutes also resembled SAR of single NCs (450±4 W/g). Later, at 3 h of incubation, the TEM images showed the existence of a chain-like configuration (Figure 1.25e & e1-e6), which was accompanied with an increase of SAR values, which was doubled (599±1 W/g) than that of the initial 2D-MNBs (294±5 W/g) as we discussed before. Such a SAR increase can be understood due to the fact that, short chains of IONCs, as a result of the magnetic dipolar coupling, behave as elongated entities with a single and large magnetic momentum, whose magnetic easy axis was expected to respond quickly to magnetic fields. Moreover, in such a short chain configuration, the shape anisotropy improves, consequently, the heating dissipations are enhanced than those of isolated IONCs (which have no dipolar interaction) and 3D-MNBs (which have a random dipolar interaction). Indeed, these results are supported by other theoretical and experimental studies.[67,122,141,142] In addition similar outcome have been noted in our another work where core-shell IONC were arranged into dimers/trimer representing short chains, whose results will be discussed at the end of this chapter in separate section (1.3.2).

TEM of incubation times of 24h and 48h revealed the presence of nanocubes both as individual and some large aggregates (highlighted in red, Figure 1.25f). These observations supports why SAR recorded at the 24 and 48 hour time points was progressively reduced. It is also worthy to highlight that, as some structural modifications occurred, the dispersibility in water was progressively affected, especially only after the three hours (Figure 1.26).

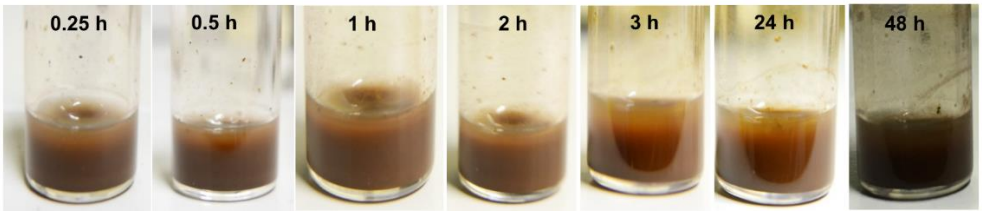

Figure 1.26. Digital images of esterase treated 2D-MNBs, incubated at 37°C for well-defined time point in the first 48 h. The images taken up to 24 h show the conservation of macroscopic stability even after the enzymatic cleavage. The last image at 48 h shows a color change, indicating an aggregation of particles, which was confirmed by TEM (fig 1.25f). Reprinted with permission of reference(125) Copyright © 2019, American Chemical Society.

1.3.8 Hyperthermia study on A431 cell line

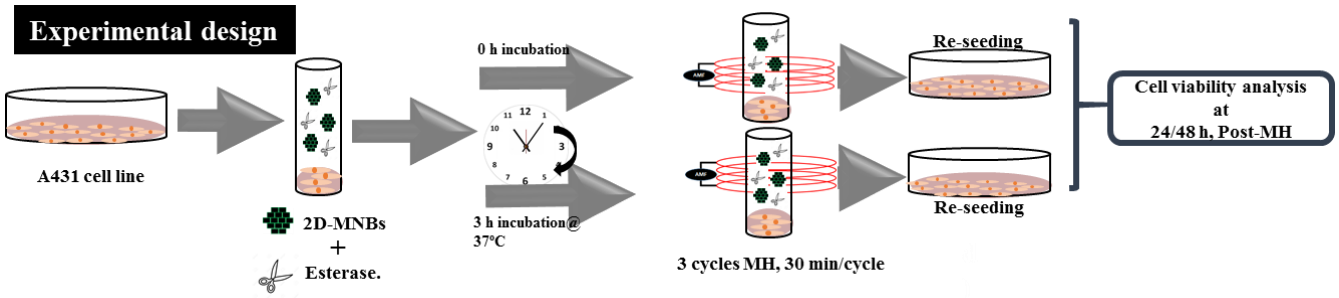

Figure 1.27. In vitro cellular experiments. a) Graphical scheme summarizing the cellular experiment. In vitro hyperthermia studies on an A431 cell line incubated with 2D-MNBs and esterase. Reprinted with permission of reference[125] Copyright © 2019, American Chemical Society.

To estimate the magnetic heat loss on the cells and the heat damage effects induced by magnetic hyperthermia treatment in the case of both the 2D-MNBs and the disassembled chains upon enzymatic action, an in vitro cellular experiment on epidermoid carcinoma cells (A431) was conducted as schematized in Figure 1.27. To this end, 5 million A431 cells, simulating a small tumor mass, were supplemented with 2D-MNBs and an esterase enzyme solution, the latter of which was added to enable polymer digestion.

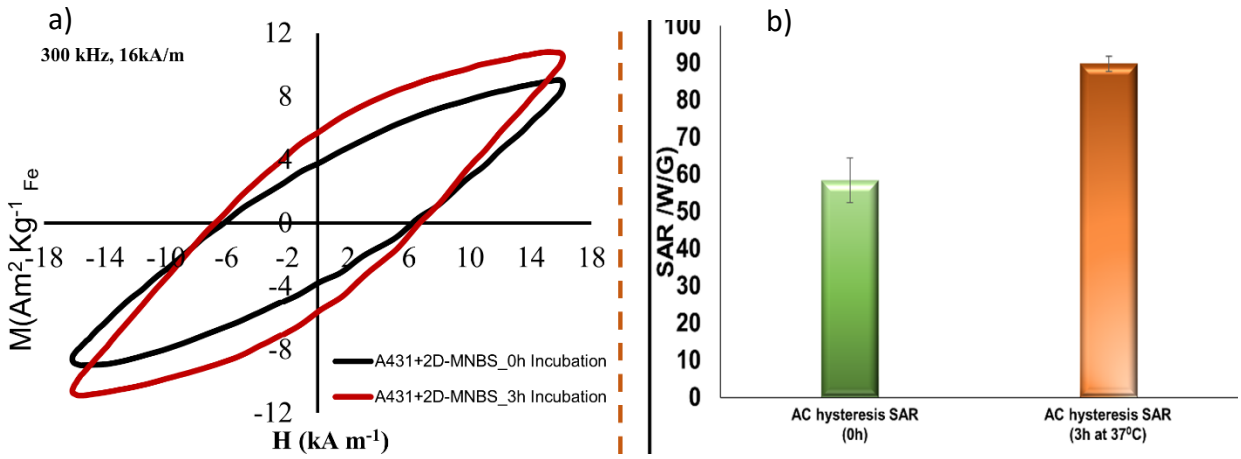

Figure 1.28. a) Comparison of AC Hysteresis loops recorded for the cell samples before (A431+2D-MNBs_0h incubation) and after incubation (A431+2D-MNBs_3h incubation) at 37°C. Even in the presence of tumor cells, the hysteresis loop is larger for the sample that had been incubated with enzymes (red curve) than for the sample that was not incubated at 37°C (black curve). b) SARs estimation based on AC hysteresis loops, for A431 treated with 2D-MNBs and esterase at time point 0h (green bar) and 3h after incubation at 37°C (orange bar). Reprinted with permission of reference(125) Copyright © 2019, American Chemical Society.

This sample was divided into two parts. On one fraction (sample named A431+ 2D-MNBs_no-incubation), the AC hysteresis loop was directly recorded (300 KHz and 16 kA/m). The second part was first incubated for 3 h at 37° C to enable the enzymatic digestion of the polymer (the sample will be referred to as 'A431+2D-MNBs_3h-incubation' from now on). Immediately after the incubation time, the AC hysteresis loops were performed that compared to A431+ 2D-MNBs_no-incubation (Figure.1.28a). The measurements clearly indicate that the sample A431+2D-MNBs_3h-incubation, which was incubated for 3h at 37°C, has a larger hysteresis loop than the A431+2D-MNBs_0h-incubation sample that was not incubated at 37°C. This was also reflected in the SAR values, which were calculated by considering the area of the hysteresis loops for both the A431+2D-MNBs_3h-incubation sample and the A431+2D-MNBs_0h-incubation sample (Figure 1.28b).

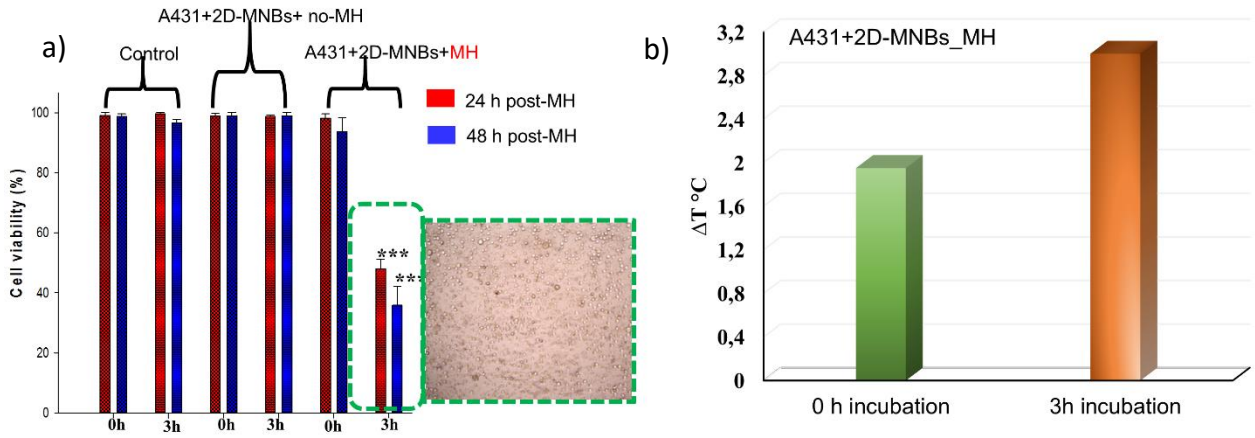

Figure 1.29. a) Cell viability study evaluating the cytotoxic effects with or without exposure to MH for A431+2D-MNBs_0h-incubation and for A431+2D-MNBs_3h-incubation. The viability was assessed after re-culturing the A431 cells after 24 and 48 hours. The MH was performed at 300 kHz and 16 kA/m. Inset: representative optical image of A431cells exposed to A431+2D-MNBs_3h-incubation and after MH treatment. Many detached round cells are present. b) Temperature variation recorded under MH for A431cells treated with MNBs and esterase just after mixing at time point 0h (green bar) or after 3h incubation at 37° C (orange bar). Reprinted with permission of reference(125) Copyright © 2019, American Chemical Society.

Moreover, this data is also supported by the cytotoxicity heat damage, which was recorded after having performed the magnetic hyperthermia treatment. In a parallel experiment, the A431+ 2D-MNBs_no-incubation and the A431+2D-MNBs_3h-incubation samples were exposed to MH treatment either immediately after the addition of the 2D-MNBs or after 3h of incubation at 37°. After re-seeding the cells, the viability was estimated by means of trypan blue assay at well-defined time points (24h or 48h) post MH-treatment and it showed severe toxicity for the A431+2D-MNBs_3h sample rather than for the A431+2D-MNBs_0h sample (Figure 1.29a). This data support the AC measurements indicating that the disassembling of the 2D-MNBs occurring during the incubation for 3 h at 37°C produced more cellular heat damages than the A431+2D-MNBs-0h incubation that was not kept at 37°C for 3 hours. The difference is also reflected in the temperature increase that was recorded during the MH treatment: the temperature reached during MH by the A431+2D-MNBs_3h-incubation sample was slightly higher than that of the A431+2D-MNBs_0h-incubation sample (Figure 1.29b). Also refer to inset optical image (Fig.1.29b) and to Figure 1.30 of A431cells exposed to A431+2D-MNBs_3h-incubation and after MH treatment. Many detached round cells are present. It should also be noted that the cytotoxicity for the same samples that were not exposed to MH treatment is negligible, independent

from the enzymatic incubation. These latter data suggest that the 2D-MNBs and the product of the digestions, i.e. the short chains, are biocompatible.

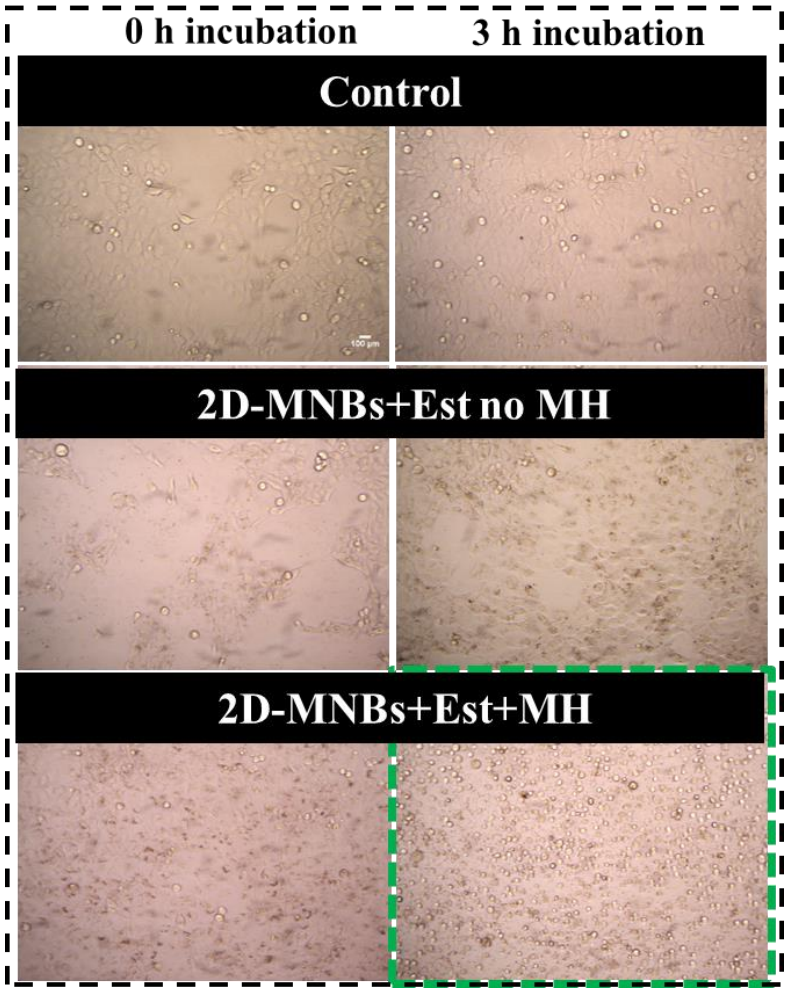

Figure 1.30. The optical image of A431 cells representing the viability results comparing with the control sample.

1.3.9 Magnetic accumulation and magnetophoretic mobility of 2D-MNBs, 3D-MNBs and single NCs

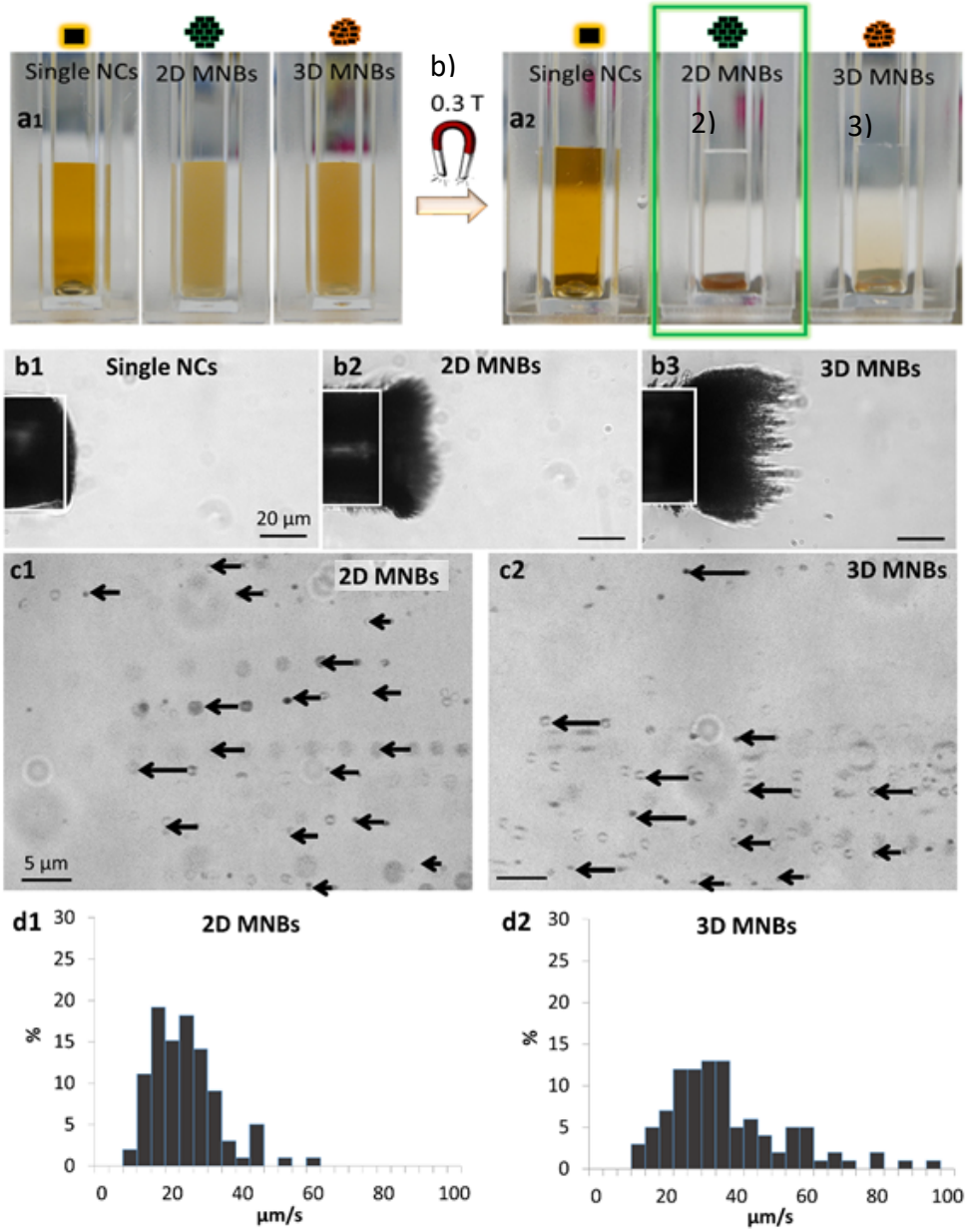

Figure 1.31. ***Magnetic accumulation and magnetophoretic mobility:*** *a1) Picture of single NCs, 2D-MNBs and 3D-MNBs dispersed in 500 µL of water (each with 40 µg of Fe) before and after exposure to a magnet (0.3T) for 24 h, 82 sec and 120 sec respectively. b) Attraction by a magnetic nickel tip magnetized in a 0.2 T magnetic field of single NCs (b1, no tip covering), 2D-MNBs (b2) and 3D-MNBs (b3). c) Magnetophoretic motions of the 2D-MNBs (c1) and 3D-MNBs (c2) towards the magnetic tip. Each image is the superimposition of successive images separated by 100 ms each. Arrows illustrate the displacement of single NBs in between two images, directly proportional to the magnetic velocity. d) Histograms of the magnetophoretic mobility in terms of µm/s, for 2D-MNBs (d1) and 3D-MNBs (d2). Reprinted with permission of reference(125) Copyright © 2019, American Chemical Society.*

Since the 2D-MNBs were composed of several nanocubes, it is interesting to analyze the response of these structures in the presence of a magnet. For macroscopical evidence, we first recorded the time required for an aqueous dispersions of three structures; single NCs, 2D-MNBs and 3D-MNBs, where each of them have the same initial iron concentration that is 40 μg_{Fe}, attracted by a permanent magnet of 0.3 T. Figure.1.31a displays the photographs of dispersions, before and after magnet exposition. As indicated, brown liquid transformed to colorless, in presence of permanent magnet. Among the three, the 2D-MNBs were attracted very quickly to the magnet which took place within 80 sec, see the green panel in Fig 1.31.a2 and this response was comparable to that of 3D-MNBs (120 sec), while, conversely it was not possible to collect single NCs even after 24 hrs. Indeed a quick magnetic response is suggestable to exploit magnetic targeting of materials at specific target site. It is Important to highlight, after magnetic accumulation, both the 2D-MNBs and the 3D-MNBs can be easily re-suspended by simply shaking, which indicates their superparamagnetic and non-interactive behavior at room temperature.

Besides macroscopic experiments, in order to confirm the magnetic attraction potentials in microscopic scale, we conducted the magnetophoretic mobility experiments on 2D-MNBs, comparing results to 3D-MNBs, and single NCs. Figure 1.31b (indexes 1,2&3) show the accumulation of nanostructures; NCs, 2D-MNBs and 3D-MNBs, respectively, on a magnetic nickel rod of diameters 50-µm with magnetic strength of 0.2 T. This creates a magnetic field gradient generated by magnetized rod in return traps magnetic nano-objects according to their magnetic properties, thus it directly represents the magnetic targeting abilities of each nano-objects. It is clearly known from the pictures that only 2D or 3D nanobeads (Fig.1.31 b2&b3) irrespectively, are attracted. While the tip of single NCs was totally uncovered (Figure 1.31.b1) which confirms the macroscopic magnetic accumulation results of in Figure 1.31a2. Besides, we have video-monitored the migration of the nano-objects towards the tip, to estimate the magnetic velocity generated within structure in response to the magnetic field gradient (200 mT/mm in the zone analyzed). Figure 1.31 c1&2 shows how typically the nanobeads migrate magnetically. The velocity (µm/s) here was computed for 100 nanobeads for each experiment and the corresponding velocity histograms was shown in Figure 1.31d 1&2. From computation, magnetophoretic velocity of 2D-MNBs was derived as 23.6±2.5 µm/s, which was slightly lower than the value that was measured for 3D-MNBs (34.2±1.9 µm/s). It is important to mention that the

hydrodynamic diameter of the 2D-MNBs is far higher (d_H=393 nm) than the 3D-MNBs (d_H=171 nm), so that 2D MNBs have high chance to face a viscosity drag friction that in return restrict their motion. Furthermore, if one estimates the magnetic moments of the clusters from the Stokes equation (see material and method section Eq. 1.9), the 2D-MNBs moment (m= 4.4±0.4x10^{-13}emu) is higher than that of 3D-MNBs (m=2.7±0.2 x10^{-13}emu). It could suggest that the planar arrangements of cubes in 2D increases the magnetic moment. However, these values must be taken with care, as the Stokes equation is based on a spherical model, which does not fit the 2D-MNBs, which are more bi-dimensional assembly. Yet it is also important to emphasize that the DLS determination of the hydrodynamic size used in Stokes formula is based on spheres, so that both approximations should compensate.

Anisomeric assembling of core-shell iron oxide nanocubes(FeO/Fe3O4 NPs) for improved hyperthermia

Apart from designing 2D-MNBs from high interacting iron oxide nanocubes, we have also initiated another study of clustering less interacting core-shell iron oxide nanocubes into three distinct geometries that includes Single core-shell nanocrystals (SCs), Dimers/trimer (Di/tri) and centrosymmetric structure/bigger clusters (BCs) and the idea is to investigate the significance of the direction of dipolar coupling in heating performance. This work was initiated by Dr. Dina Niculaes and published recently.[86] Since I have contributed for the work, here I am giving brief discussion about the outcomes of this work which give some conclusions regarding the importance of anisomeric clustering for better heat performance, which indeed supports the observations reported for 2D-MNBs in response to enzymes, where they have formed short chains similar to Dimers/Trimers in this work.

1.3.10 Procedure of clustering core-shell IONC

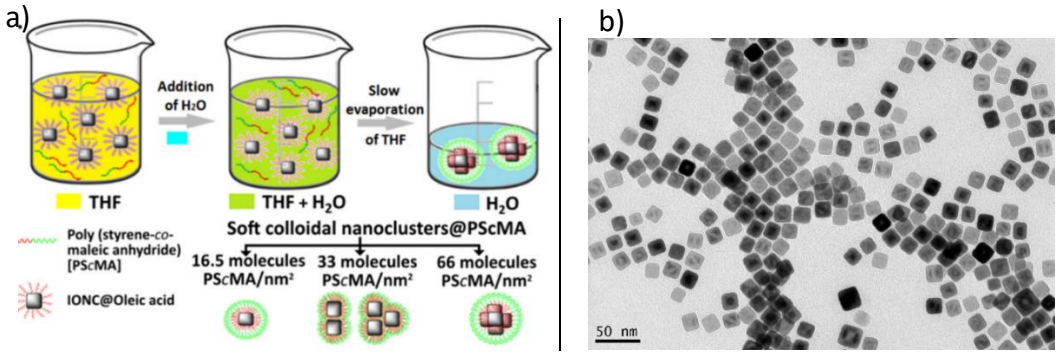

Figure 1.32. a) The scheme representing the procedure for clustering FeO/Fe_3O_4 core–shell iron oxide in a controlled manner by changing amount of polymer (poly(styrene-comaleic anhydride) (PScMA), cumene-terminated) as main parameter (Reprinted with permission of reference(86) Copyright © 2017, American Chemical Society. b) The TEM images of the FeO/Fe_3O_4 core–shell iron oxide nanocubes (Cs-IONCs) used in this procedure.

Figure 1.32a schematized the entire procedure of preparing the clusters of three different morphologies. The FeO/Fe_3O_4 core–shell iron oxide nanocubes (Cs-IONCs, Figure 1.32b) with an edge length of 18 ± 2 nm were applied in this study for clustering. The choice of Cs-IONC was justified by the fact of their non-interactive behavior and initial stability in THF. Indeed when the reaction was performed with high interacting, partial THF soluble nanoparticles, it resulted in clusters of deformed shapes and poor reproducibility, which the data we will present later. Both the said conditions were considered as prerequisites for a successful clustering protocol. In this typical clustering procedure (taken dimers and trimers formation as an example), as-synthesized oleic-acid capped Cs-IONCs (m_{Fe} = 0.23 mg) were dissolved in 10 mL of THF composed of a commercial amphiphilic polymer poly(styrene-comaleic anhydride) (PScMA), cumene-terminated, at a polymer ratio of 18 chains/nm^2 of particle surface. A three minutes of subsequent sonication has improved the stability and homogeneity of the mixture, where the solution appeared clear, which was a clear indication for the perfect solubility of cubes (Figure 1.33).

Figure 1.33. Photograph of the reaction mixture before destabilization with water, composed of Core-shell IONCs and PScMA that are dissolved in THF.

Then, the initial mixture was destabilized by adding 1 mL of H_2O with an assistance of syringe pump at the rate of 0.5 mL/min, while sonicating in an ice bath of temperature 10°C. We preferred to perform the destabilization step under sonication because it may prevent uncontrolled aggregation of magnetic cubes. A clear indication of difference in appearance of reaction mixture was observed if the step hasn't been taken place under sonication, as given in Figure 1.34. As we can see, the solution became turbid in the absence of sonication (Figure 1.34a. left image) and on contrary the same reaction turned clear under sonication (Figure 1.34a. right image), that these observations supported our assumption made about the necessity of sonication.

a)

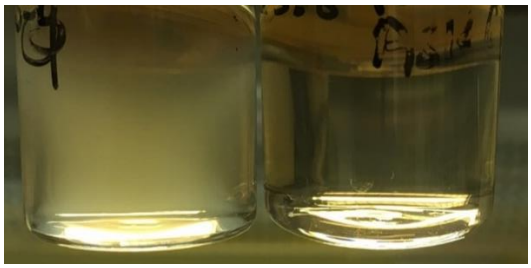

b)

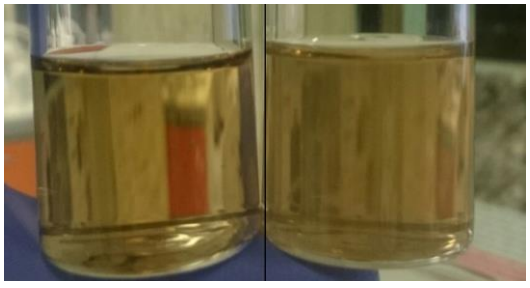

Figure 1.34. a) Photographs of reaction mixture after destabilizing with water, the one on the left performed without sonication. The image on the right, the same reaction under sonication. b) The images from left to right represents the unchanged of appearance from before to after destabilization.

In addition, it is also important to state that the appearance of solution haven't differed from before to after addition of water, which indicates the control over the reaction (Figure 1.34b). Later, the THF was completely evaporated from the mixture, under room temperature, shaking on a horizontal shaker (100 rpm). However, the appearance of the solution remain unchanged unless the last 0.5 mL of THF was evaporated and then the solution became turbid. This data suggests that, as soon as THF gradually evaporates from THF/H_2O mixture, it brings polarity changes in the solution, thereafter the clustering was favored due to the change in solubility of polymer and magnetic cubes. The solvent extraction process by adding chloroform, as described in methods section, promoted the removal of the excess polymer/surfactants from the product.

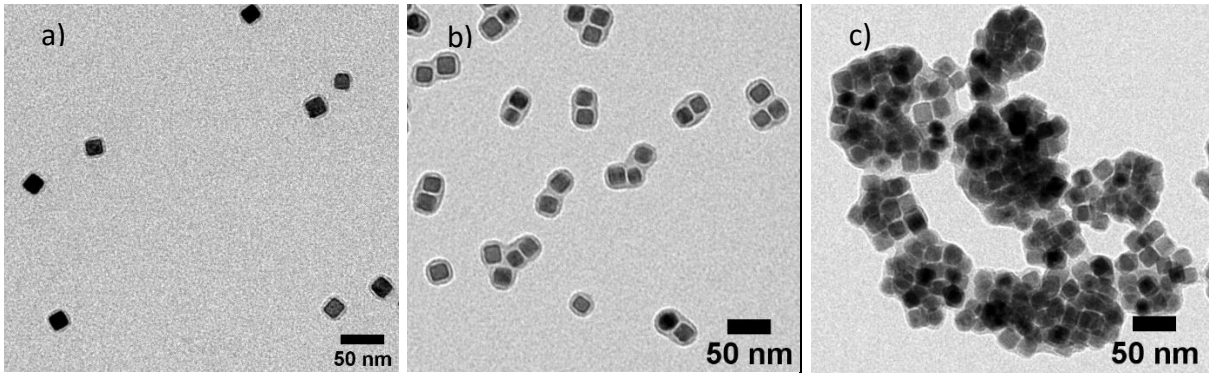

Figure 1.35. TEM images of particles in water. a) Core–shell iron oxide nanocubes coated with PScMA as individual particles at polymer amount of 12 molecules/nm², b) into Dimers/trimers at 18 molecules/nm², c) centrosymmetric clusters of particles >4 at 35.5 molecules/nm².

For fine tuning of the cluster configuration, we have determined adjusting number of PScMA polymer molecules per square nanometer of particle surface as the main parameter. Accordingly, when this ratio of polymer was increased from 12 to 18 and further to 35.5 molecules/nm^2, that corresponded to change in size or configuration of the particles; SC, Di/tri and BC respectively. As we can note on the TEM micrographs of Figure 1.35, corresponding to 12 molecules/nm^2 (Fig.1.35a) the cubes remain isolated with a clear evidence, confirming the presence of polymer and for 18 molecules/nm^2 (Fig.1.35b) most formed are Dimers/Trimers and when this amount of polymer has been doubled; 35.5 (Fig.1.35c) cubes were evolved as bigger clusters; each holding > 4 nanoparticles per cluster.

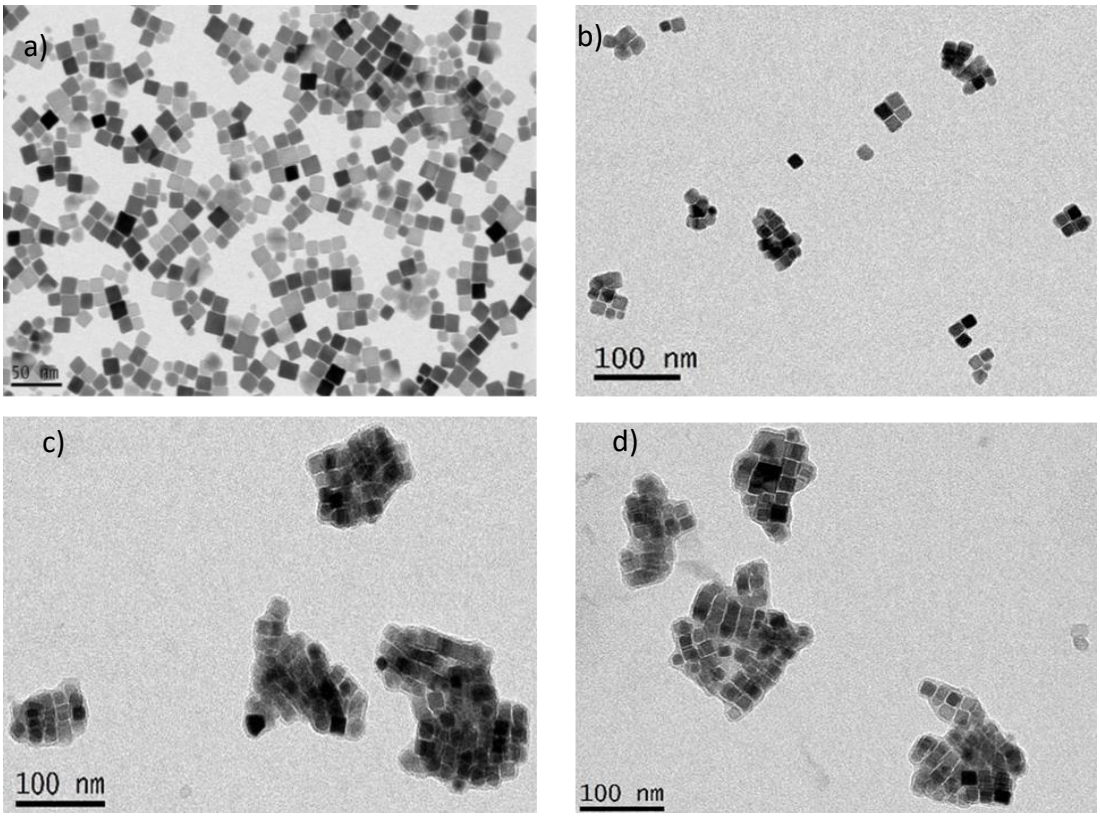

Figure 1.36. The repetition of the protocol using single phase high interaction iron oxide nanoparticles of edgelength instead of core-shell. A) as-synthesized 13 nm IONC, b) the reaction at 12 molecules/nm2 c) 18 molecules/nm2 and d) 35.5 molecules/nm^2.

As we stated before, the choice of non-interacting core-shell IONC was the one main reason for the success of protocol. Because, when we performed the same reaction using high interactive single phase iron oxide nanocubes (Fig.1.36a), we have lost control over the reaction, where it always resulted in turbid and unstable solution after addition of anti-solvent. Indeed, the final clusters under TEM appeared random and deformed (Fig.1.36b-d). In addition, the reproducibility of this procedure was greatly questioned, since we do not have proper control over the reaction.

The mean hydrodynamic diameter of clusters at different polymer amounts was determined by DLS as the results given in Figure 1.37 (dotted lines). The hydrodynamic size (number) of soft colloidal clusters can be adjusted based on polymer amount (Consider Sample 1a, 2a, 3a (dotted lines)) which corresponds to Single crystals, Dimer/trimer, bigger clusters respectively, that before thermal annealing in water.

1.3.11 Hydrodynamic diameter of nanoclusters in water.

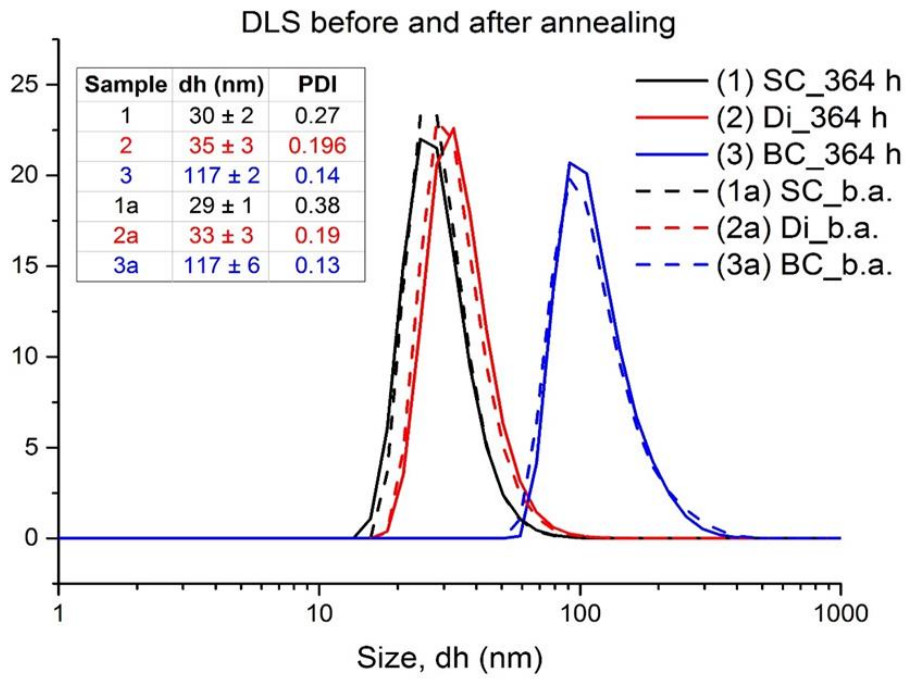

Figure 1.37. Mean hydrodynamic size (dH) of nanoclusters in water, explaining the fact of increase dH as function of polymer amount. The dotted lines obtained before thermal annealing of the clusters and continues lines derived after annealing of samples at 80°C for 365 hours, which indicates stability of clusters even after harsh thermal treatment.

As given in Figure 1.37, the mean hydrodynamic diameters by number were 29±1 nm (PDI 0.38), 33±3 nm (PDI 0.19), 117±6 nm (PDI 0.13) for SCs, Dimer/trimer, BCs respectively. No signs of aggregation were detected as their polydispersity index (PDI) values are acceptably narrow and indicate a homogeneous distribution of the clusters in water. This cluster in solution remain stable for a very long time (more than a year) without showing any sign of aggregation, that we have utilized same samples later for magnetic particles imaging (MPI) and MRI studies which will be discussed in next chapter.

1.3.12 Comparing magnetic hyperthermia performance of nanoclusters.

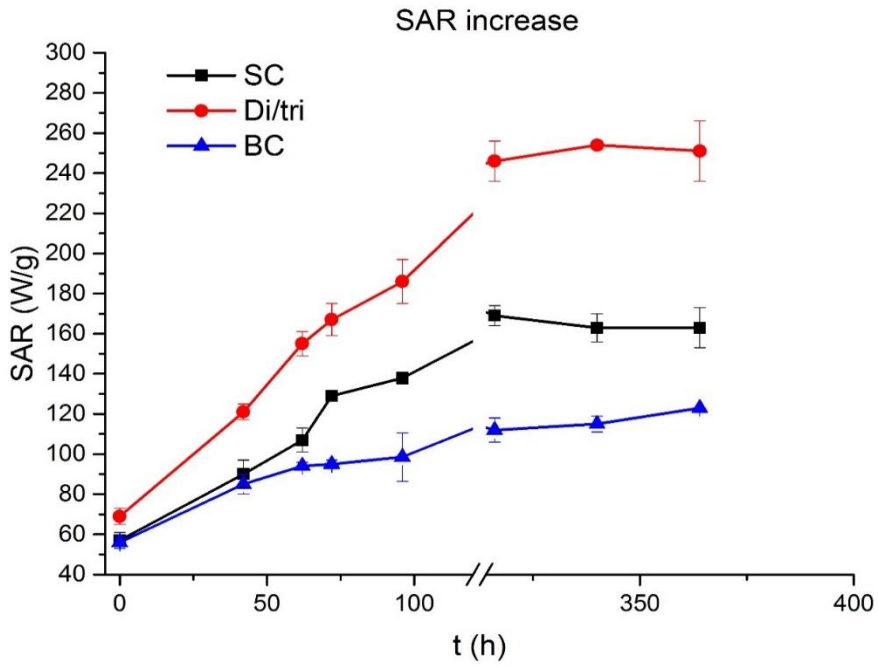

Figure 1.38. Evolution of SAR in soft colloidal clusters of Cs-IONCs: Calorimetric hyperthermia performance of soft colloidal nanoclusters of core-shell IONC, formed at polymer amount of 12, 18, 35.5 molecules/nm², measured at 300 kHz and 24 kA/m, which were recorded as the function annealing time at 80°C.

Figure 1.38 presents SAR values of the soft colloidal nanoclusters measured as function of the annealing time at 80°C over a span of 365 hours, measured at 300 kHz and 24 kA/m of magnetic field excitation range. As we can see, at time zero all the three; SC, Di/tri, BC have poor SAR values, however relatively higher for the di/tri. Their poor performance before thermal annealing is due to the fact of their poor magnetic behavior. As it is reported in XRD data of paper published, the initial Cs-IONC have dominated wustite phase (FeO, paramagnetic) and limited magnetite phase (Fe_2O_3) and it's has been well know paramagnetic materials do not suits to have energetic hysteresis losses, hence reflected as week SAR. Once after initiation of thermal oxidation at 80°C, the FeO cores gradually transformed into magnetite phase.[86] In fact, such a transformation has been corresponded to contaminant increase of SAR with annealing time, however obtained a saturation after 100 hours, because of complete dominance of magnetite phase at this point. The question arises whether cluster could withstand such harsh oxidation process to transform the phase, rather than choosing long room temperature oxidation. To investigate this, we have re-measured the hydrodynamic diameter of three samples, post

annealing, which confirmed their ability to sustain harsh oxidation process, because as compared in Figure 1.38, peak position and PDI values haven't changed from before to after annealing (continues lines corresponds to dH after annealing), which confirms their stability.

Besides the said trend, the SAR of Dimer/trimers dominate throughout the analysis. Such an increase of SAR can be explained due to fact of their dipolar coupling among particles. The particles in chain favors longitudinal alignment of magnetic crystallographic easy axis, where assembly can behaves as single magnetic nanorod whose magnetic susceptibility enhances along the chain direction, as a result improve effective anisotropy of the nanocubes, as it was confirmed by other theoretical studies.[68–70] The long-range dipolar interaction of the particles resulted in a cluster with a chain-like spatial distribution whose magnetic easy axis remains parallel to each crystal, and leads to the macroscopic, magnetization moment.[82,84] On the contrary, in 3D assemblies, the closed magnetic moments are arranged in a three-dimensional assembly where nanoparticles have a random spatial distribution, resulting in a decrease of magnetization, and consequently, reduces the heating performance.[83,102]

1.4 Conclusions

In this chapter, firstly we described the protocol for producing bi-dimensional structures of high interacting IONCs by using a low molecular weight derivative of mcl-PHA named as oligo-PHA, which was a bacteria derived, esterase sensitive biopolymer, as an assembling agent. PHA with low molecular-weight together with working parameters such as low water injection rate and slow shaking, enabled well-defined self-assembling of the IONCs into bi-dimensional structures. In our systematic comparison of 2D-MNBs with single NCs and 3D-MNBs produced from the same batch of IONCs, the aqueous dispersion of 2D-MNBs exhibited SAR values lower than those of single NCs but two-fold higher than 3D-MNBs. This behavior can be explained due to 2D spatial confinement of IONCs, resulting in special magnetic properties. Such spatial arrangement is weakly influenced by inter-particle magnetic dipolar interactions, contrary to 3D-MNBs. In addition, AC hysteresis loops of 2D-MNBs at given frequencies remained almost unaltered even after inducing intentional aggregation. Moreover, attributing to their high volume to surface ratio, 2D-MNBs exhibit a relatively quick response to an external permanent magnet (0.3 T), which was a crucial property for magnet guided localization and MH experiments that could assist to maintain optimal concentrations at tumor site. Above all, for the first time, we

demonstrated an esterase response cleavage of 2D-MNBs into short chain like geometries, when incubated at temperature mimicking physiological conditions. Interestingly, corresponding to evolved morphologies, SAR value of 2D-MNBs almost doubled as function of incubation time in presence of enzyme (up to 3h point). Within these observations, the *In vitro* cellular experiments on the A431 cells that were incubated with 2D-MNBs in the presence of esterase demonstrated cellular heat losses and significant cytotoxicity only after 3h of incubation at 37 °C and exposure to MH treatments. This can attributed to the better heating abilities of 2D-MNBs upon esterase disassembling. It is worth to highlight that the enzymatic digestion of 2D-MNBs in the test tube and in the in vitro cellular experiment represents a first proof of concept of the action of the esterase enzyme on the 2D-MNBs, leading to the disassembly of chain-like structures, which, in turn, produce more cytotoxic effects on tumor cells than the initial 2D-MNBs under MH. However, for a practical *in vivo* translation, under lytic enzyme conditions on a real tumor mass, the experimental conditions must be further investigated.[143,144]

Overall, our observations clearly show the potentiality of the 2D-MNBs as magnetic hyperthermia agents, since the heating performance is enhanced via the intracellular enzyme esterase, using the same doses of initial material injected. This could solve the issue of massive decrease in SAR that efficient nanomaterials for magnetic hyperthermia generally face when internalized and confined within endosomal intracellular compartment. The results shown here suggest that polymers based on cleavable enzymes could help to design a new generation of IONC-based clusters having dissembling features. This will help to pass from clusters being able to be promptly manipulated under external magnetic fields to intermediate configurations having more performing heating losses and at the same time facilitating their disassembly into smaller portions easy to be degraded and eliminated by the body.

Secondly, we have constructed core-shell iron oxide nanocubes into distinct geometries such as individual, dimer/trimer and centrosymmetric structures, by using the same commercial polymer. We have identified, changing the ratio of polymer molecules per nanometer square of particle surface as main parameter to tune the hydrodynamic size and morphology of the cluster. The less interactive behavior and their great initial stability in THF can be stated as a key feature necessary for the success of the controlled clustering. Indeed a reaction with high interacting particles, with similar features that

of IONCs used for 2D-MNBs, given deformed and uncontrolled geometries. When magnetic hyperthermia properties of three structures was studied as function of annealing time at 80°C, the SAR have been emerged with time because the paramagnetic, initially dominated wustite phase was gradually oxidized into magnetite under high temperature, thus favoured for MH response. Among the three, always the Dimers/trimers clusters were identified as best heat mediators, because of linear dipolar coupling and improved anisotropy. The increase of SAR in dimers/trimers of this project, are in complement to the similar findings corresponds to the shorts chains emerged from 2D-MNBs (produced from high interacting IONCs) when treated to esterase enzymes and incubated at 37°C. However, the absolute SAR values of Dimer/trimer was lower to the enzyme generated short chains, due to the poorer magnetic quality of the initial nanocrystals. In overview, this work emphasize how to achieve higher heat performances, by using the same nanoparticle building blocks that are arranged into anisotropic constructs through a smart and control versatile approaches, that are composed of two to three particles and second by promoting their phase transformation to Fe_3O_4.

2. Multimodel Imaging Abilities of Nanoclusters of Iron Oxide Nanocubes; Magnetic Particle Imaging/Magnetic Resonance Imaging

2.1 Introduction

The iron oxide nanoparticles (IONPs), despite their promising performance for magnetic hyperthermia (MH), were also explored and widely applied as magnetic tracers in high-resolution imaging techniques. Indeed, with the aim to improve diagnostic accuracy MNPs are interesting probes for magnetic resonance imaging (MRI)[9,145] and recently emerging magnetic particles imaging (MPI).[146]

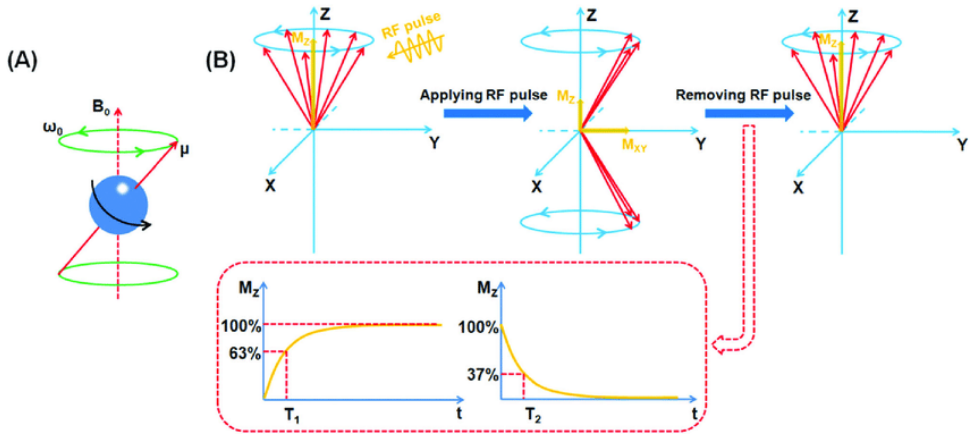

Figure 2.1. Scheme illustrating fundamental principle of MRI.[147] Adapted from reference (147) with permission from The Royal Society of Chemistry.

MRI works on the same principle of nuclear magnetic resonance (NMR).[148] It detects the magnetic moment of water proton (H^1). Generally, under a static magnetic field (B_0) the magnetic moments (μ) of proton aligns and rotates at a certain frequency (Larmor frequency w_0) along the direction of B_0 as shown in Figure 2.1a. On applying a short radio frequency pulse, the net "μ" of system flips away from the equilibrium. Upon removal of the radio frequency pulse, proton usually relaxes through two types of motions; the longitudinal, spin-spin relaxation that defines the z component magnetization recovery of nuclear spin towards thermal equilibrium (T_1) and transverse relaxation (spin-lattice relaxation) defined as the decay constant (T_2) of nuclear spin magnetization perpendicular to the static B_0 magnetic field.[147] In fact, the time taken by the proton spin to relax back varies based on the properties of

surrounding environment,[149,150] thus differs in contrast and this time can be measured in terms of relaxation time; T_1 (longitudinal) that corresponds to an increase in signal, the brightening of the contrast and T_2 (transverse) relaxation time that corresponds to a darkening of contrast. Both times generally fall in the milliseconds (m sec) range. The complete scheme of MRI working principle is given in Figure 2.1. The relaxation times of proton can be shortened to enhance the contrast of tissue by administrating contrasting agents;[8] among them superparamagnetic MNPs (T_2) are chosen as dark contrast which affect transverse relaxation[151], while paramagnetic based molecules (T_1) are chosen as they increase the bright signal affecting the longitudinal relaxation of protons.[152,153] The efficiency of this colloidal contrast agents can be estimated in terms of relaxivity rate values, r_1 (longitudinal rate) and r_2,(transverse rate) which is calculated from the linear slope fitting obtained by inverse of the relaxation time (T_1 or T_2) as a function of elemental concentration. It is worthy to highlight, this technique of detecting magnetization generated by the magnetic moments of water proton was adopted mainly because, more than 60 % of body contains water. In spite of its efficiency for soft tissues, such as for brain tumors, it suffers from low sensitivity.[12] Just to make a point, In MRI, iron oxide nanoparticles are widely used as negative agents to bring dark contrast to the tissue (r_2 relaxation). But, their superparamagnetic behavior, sometimes even shortens transverse relaxation of water proton out of the region where they are located, thus also darkens the site out of interest, which would create ambiguity in distinguishing target tissue from the offsite.[154,155] To filter such artifacts, it's been often suggested to apply multimodal imaging modalities.

Instead, the MPI is a quantitative real-time advanced tomography technique whose signal intensity is directly proportional to the concentration of the magnetic tracer, because a receiving coil in the setup directly detects the electronic transition (harmonics) of the magnetic tracer under magnetic excitations,[146,156,157] which later gets converted into Fourier transform signal. In fact, unlike the MRI, it directly detects the magnetic moments of magnetic tracers located at the target site. In comparison to "μ" of proton, the IONPs have "μ" at least 8 order of magnitude stronger, therefore consequent detection of magnetization strength can be 22 million times predominant than what we received in MRI.[15,158] Hence it's been claimed, with respect to MRI, MPI was very competitive for its resolution and tracer sensitivity. In addition, this noninvasive technique was operated at the low magnetic excitation fields, that detects signal only from the nanoparticles with no features of background

single/interference from diamagnetic biological tissue,[146] thus lowers the chance of artifacts. Combination of advanced MPI imaging with conventional MRI as a multimodal imaging modality was advantageous to increase the diagnostic accuracy with more anatomical details.[12,159,160] For instance, Kaul *et al*. in 2015 presented first commercial installed preclinical study in mice model in order to establish a work flow combining MPI and MRI.[161] Salamon, J. *et al.*[160] evaluated real time 4D tracking of endovascular devices and stenosis treatment by merging MPI and MRI imaging modalities; however this method was investigated in an *in vitro* model. By proper engineering of spatial encode of instrument, the excitation spot could be narrowed to increase the resolution, where the particles out of spot remain unaffected, which could prevent unintentional excitation of off-targets,[156,162] that addresses common drawback of magnetic hyperthermia. Since this MPI works on the same principle of MH, where MNPs are excited by applying AMF of certain field and frequency of lower frequency and field amplitude of those used in MH, the strategy of exciting same particles for heat generation can be implemented without affecting vital organs as performed elsewhere.[157,162] This combined MH and MPI modalities is also termed as magnetic nanoparticles imaging guided hyperthermia or hMPI. Indeed, similar to MH, the signal intensity in MPI depends on relaxation rate of MNPs (Neel's or Brownian), in response to AC magnetic fields.[163–165] Most of current studies adopted a commercial product Resovist as standard material for MPI. After knowing from theoretical studies that optimal size of MNPs necessary for MPI as 30 nm,[166] the performance of Resovist was surprising, because their core-size was between 4-6 nm.[166] However, it has been realized later, that Resovist form small aggregates of 24 nm size, behaving like monodomain particle, contributes to MPI signal.[167] Unfortunately, Bayer had abandoned this product in 2009. However due to small size and poor distribution of Resovist, it cannot be recommended as ideal candidate for MPI, because only 3% percent of its iron mass contributes to the signal. Moreover, due to poor heat performances of Resovist MNPs,[166,168] theirs applications in hMPI is certainly not optimized and for this reason alternatively MNP material have been searched.

Similar to MH, the signal intensities of MPI depend on the intrinsic properties of the MNPs.[157] Besides proven efficiency for MH[169] and MRI imaging properties[75] (T_2 relaxation abilities), some studies have demonstrated the use of magnetosome magnetic nanocubes extracts from bacteria also for MPI.[158] The performances achieved were assigned to their morphology, the cubic-based shape and high saturation magnetization (M_s). For instance, Kraupner, A. *et al.,*[158] investigated the application of MNPs

from magnetosmones as MPI tracers and reported a significant increase of signal in case of magnetosomes rather than in Resovist, due to the fact of large magnetic core.

2.1.1 Objective of the work

Given the fact that the development of tracers for MPI/hMPI is still in the early stage of research, during my doctoral work and thanks to the collaboration with other group expert in MPI imaging we have characterized some of the materials developed for MH also for MPI and MRI applications. In particular we have exploited our nanostructures reported and discussed in chapter 1 including the 2D-MNBs prepared from high interacting IONCs and the Dimers/trimer (Di/tri), individual cubes (SCs) and bigger clusters (BCs) produced from same core-shell iron oxide nanocubes for the MPI study. The MPI results obtained on these clusters were compared to the "gold standard", the Resovist. In particular, on the enzymatic degradable polymeric 2D-MNBs we were interest to study the evolution of the MPI signal as a function of the exposure of the 2D-MNBs to the esterase enzyme. As for the SAR values that were almost doubled upon enzymatic we were indeed expecting a significant change of the MPI signal during the enzymatic degradation and which indeed it was confirmed by our data. In addition, we have also detected efficient r_2 relaxation properties of all the nanostructures in water for MRI imaging. This complementary investigation of our geometric magnetic nanoclusters for MPI and MRI as multi imaging modalities along with MH, could create a new insight into next generation materials that can be considered as potential theranostic probes with simultaneous therapeutic and diagnostic properties, eventually expected to guide MH for an more targeted treatment planning.

2.2 Materials and methods

2.2.1 Anisomeric nanostructures from core-shell IONCs

The iron oxide core shell nanocubes;FeO/Fe_3O_4 (Cs-IONCs) of edge length 18±2 nm were clustered in a controlled manners into three different morphologies; single NCs (SC), dimers/trimer (Di/tri) and Bigger clusters (BCs), using commercially available polymer poly(styrene-co-maleic anhydride), cumene-terminated (PScMA, Mn = 1600 g/mol), exploiting the number of polymer chains per nanometer square as the main parameters to obtain desired geometry of the assembly. Please refer

to the section 1.2.21 in chapter 1 for more details of synthesis. The nanocubes utilized for this procedure initially have a core-shell structure (FeO/Fe_3O_4), dominated mostly by paramagnetic FeO and therefore not useful for MH. Under these conditions the FeO/Fe_3O_4 nanocubes are not interacting and therefore are easy to manage and could be easily incorporated within the different nanoclusters assemblies. However, before MPI analysis each cluster sample was thermally oxidized at 80°C for 360h, in order to transform completely the FeO phase into a magnetically active Fe_30_4 phase, according to the our procedure recently published.[86]

2.2.2 2D-MNBs synthesis from high interacting IONCs

The high interacting IONCs were assembled into two dimensional magnetic nanobeads (2D-MNBs) by using a bacteria derived polymer oligo-polyhydroxyalkonate (oligo-PHA), through solution phase self-assembly method, modified from protocol established in Pellegrino group.[64] Please refer to the section 1.2.5 in chapter 1 for more details of the synthesis. As we hypothesized before, the linearity,[136] and amphiphilic properties of the oligo-PHA that are in combination with our working parameters such as slow shaking (420 rpm) and injection rate of antisolvent (0.5 mL/min) promotes bidimensional ordering of IONCs.[137]

2.2.3 Magnetic particle imaging relaxometry (MPI)

MPI analysis was performed at Case Western Reserve University by the group of Dr. Anna Cristina S. Samia, at the Department of Chemistry, Cleveland, in a custom made MPI device, according to the procedure reported by Bauer, M.*et al*[157] A rough scheme of MPI relaxometry and how the signal generated from the instrument to perform analysis was given in Figure 2.2. In this measurements, the magnetic materials located in the chamber are exposed to alternating magnetic fields of certain field and frequency (excitation fields). In return, the magnetic materials undergo magnetization reversal process. This harmonic response of MNPs create electric induction in receiving coil surrounding the chamber that defines the information of the tracer.[146]

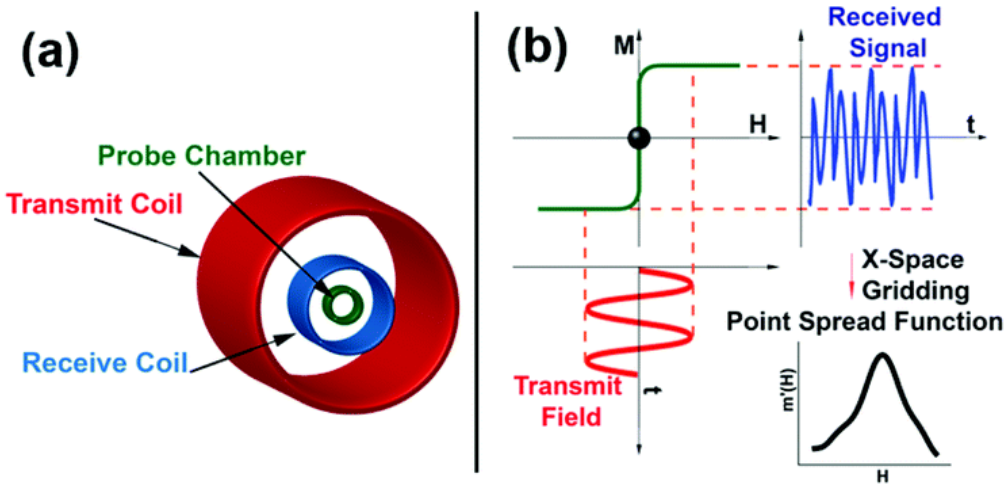

Figure 2.2 a) Scheme of the magnetic particle relaxometer used in our study to evaluate MPI performance on different nanoclusters produced from nanocubes. b) Scheme illustrates how signal generated in magnetic particle relaxometry. Adapted from reference (157) with permission from The Royal Society of Chemistry.

Before beginning the test, the background signal was collected and subtracted from the average signal produced by the sample, where n=3; averages of background and sample signals. The values of signal to noise ratio (SNR) were given by dividing the point spread function (PSF) peaks with the noise signal generated by instrument when measuring the deionized water. The full width and half maximum values (FWHM), which suggests resolution was derived from the one half value of PSF peak. An approximation of image resolution can be determined if we divide FWHM to strength of static field gradient.

2.2.4 MPI signal of nanoclusters

For MPI analysis on nanoclusters; SCs, Dimers/trimers and BCs produced from Cs-IONCs was performed in an aqueous suspensions of 200 µL at a fixed iron concentration of 0.48 mg_{Fe}/mL prepared in NMR tubes and well sonicated before measurement. In the case of 2D-MNBs, the solution was prepared in a volume of 450 µL at 0.5 mg_{Fe}/mL. The excitation of materials was conducted at a fixed field and frequency of 20 mT and 16.8 kHz respectively. The MPI signal generated was compared to the normalized signal of Resovist.

2.2.5 MPI signal of 2D-MNBs after esterase

To 450 µL of 2D-MNBs aqueous suspension (0.5 mg_{Fe}/mL), we added 23 µL of esterase enzyme (2 mg/mL, liver porcine esterase (Sigma-Aldrich)) and incubated for 48h at a temperature that mimics biological environment; 37°C. Later, MPI relaxation properties were re-recorded at several intervals during incubation, starting from 0h to 48h.

2.2.6 Relaxivity measurements

Proton relaxation profile of SCs, Dimers/trimers, BCs form Cs-IONCs and 2D-MNBs from IONCs was analyzed using a Minispec spectrometer (Bruker, Germany) mq 60 (1.5 T) according to published work.[64] Samples were prepared at a concentration ranging from 0.009 mM to 0.6 mM (based on iron) in an aqueous solution. Just to mention, sample of 2D-MNBs was prepared in 0.3 % agarose solution at the above concentration range. The relaxation constants; r_1 and r_2 (longitudinal and transverse relaxation) were determined from the linear slope of relaxation times ($1/T_{1or2}$ $mM^{-1}s^{-1}$), given by the following Equation 2.1.

$$\frac{1}{Ti\,(obs)} = \frac{1}{Ti(H2O)} + r_i C_{Fe} \quad (i = 1,2) \qquad \textit{Equation 2.1}$$

The C_{Fe} represent the concentration of the iron.

Before initiating the measurement, each sample was sonicated for 30 sec to ensure uniform dispersity of materials. We have also determined relaxation properties of 2D-MNBs after exposing to esterase enzyme which was incubated at 37°C. For this, each dilution of 2D-MNBs was added with 10 µL of esterase enzyme (2 mg/mL) and re-recorded relaxation times at time intervals of 1.5 h and 3 h.

2.3 Results and Discussion

2.3.1 TEM images of nanoclusters for MPI and MRI studies

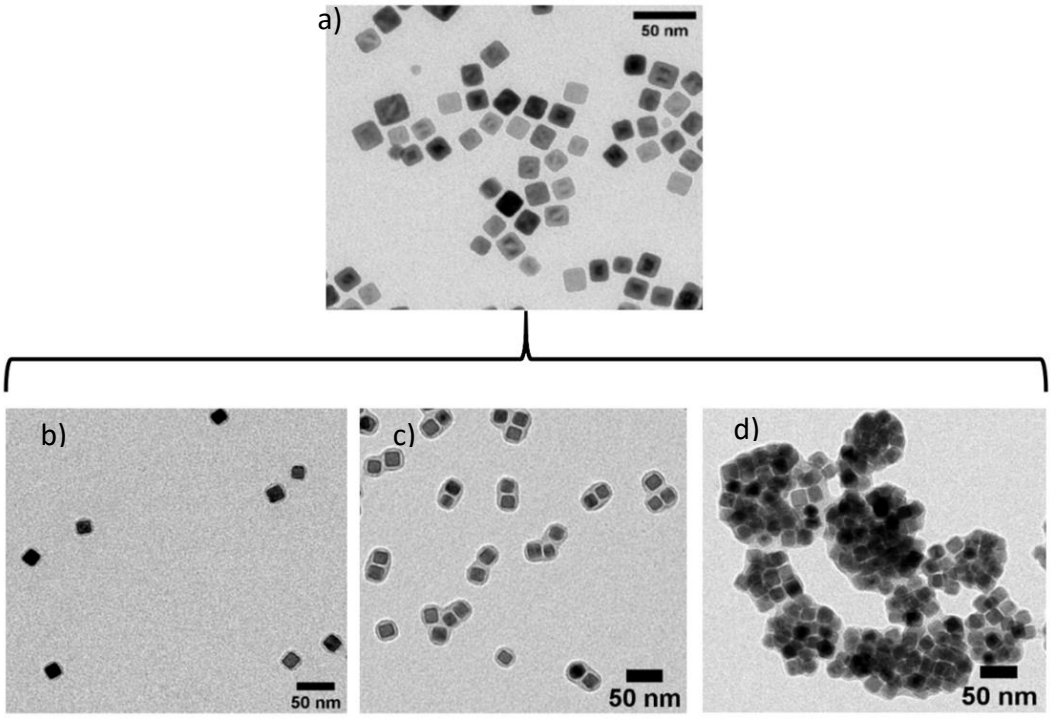

Figure 2.3 TEM images of a) as-synthesized core-shell iron oxide nanocubes in $CHCl_3$. b) Water stable core-shell iron oxide nanocubes obtained in individual forms at a PScMA concentration of 12 molecules/nm^2. c) The same into dimer /trimers at 18 molecules/nm^2 and d) into centrosymmetric structures at 35.5 molecules/nm^2. The images from b-d are captured after thermal annealing at 80°C.

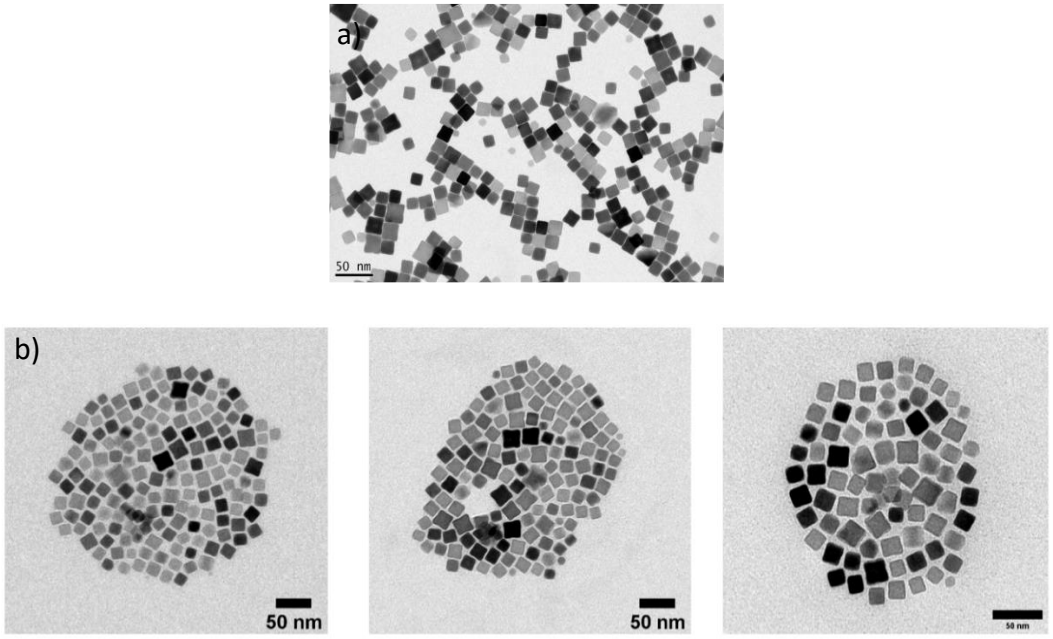

Figure 2.4. TEM image a) assynthesized high interacting iron oxide nanocubes. b) Water stable 2D magnetic nanobeads produced from the combination of high interacting iron oxide nanocubes and oligo polyhydroxyalknonate (10 kDa).

With the goal to understanding dual imaging abilities of our structures which were previously investigated for MH, in chapter 1, we have analyzed their MPI and MRI properties. The following clusters are studied here: 1) the single coated NCs (SCs,fig2.3b), Dimers/Trimers (Di/tri,fig.2.3c) and Bigger and packed centrosymmetrical clusters (BCs, fig 2.3d) produced from the same batch of non-interacting CS-IONCs (figure 2.3a) which are then thermally treated to convert them in one single phase Fe_3O_4 nanocubes. 2) The 2D-MNBs (Fig.2.4 b-d) were instead produced directly from highly interacting single phase IONCs (Figure 2.4a) when using an esterase degradable polymer; oligo-PHA. The colloidal stability of all these structures was confirmed by hydrodynamic measurements using DLS (Figure 1.37 and 1.22 respectively of chapter 1).

2.3.2 Magnetic nanoparticles imaging relaxometry measurements of nanoclusters

2.3.2.1 MPI signal of anisomeric structures form core-shell IONCs

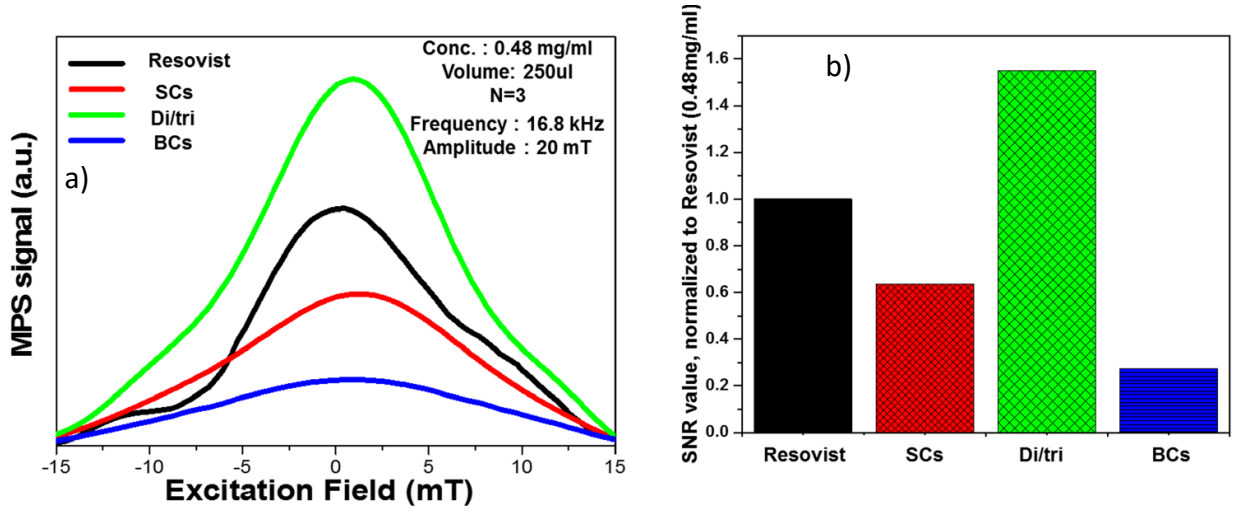

Figure 2.5 a) The normalized point spread function peaks of Single NCs, Dimers/trimers, Bigger clusters from Core-shhell IONCs. b) Corresponding signal to noise ratios, data compared to Resovist standard.

MPI relaxometry measurements were performed on SCs, Dimer/trimers and BCs and compared with normalized MPI signal of Resovist that upon exposure to a sinusoidal magnetic excitation fields of 16.8 kHz and 20 mT. Each sample was analyzed at a fixed iron concentration of 0.48 mg/mL in a final volume of 250 µL of water as given in Figure 2.6.

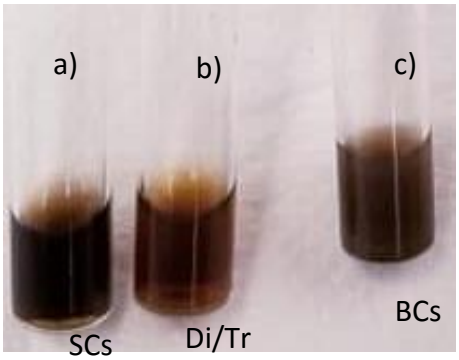

Figure 2.6 Photograph of aqueous dispersions of a) Single nanocrystals (SCs) b) Dimer/trimers and (Di/tri) c) Bigger cluster (BCs), in sample holder for MPI measurements.

Our previous analysis of this series of samples for MH (Figure 1.38) revealed advanced heating properties for Dimers/trimers than that of their individual forms (SCs) and BCs, which was explained due to their improved anisotropy and linear dipolar coupling, as we published previously.[86] Similarly, here the MPI signal of Dimers/trimers (green peak), compared to SCs (red), BCs (blue) and Resovist (black), have greater point spread function (PSF) positioned around 1.2 mT, as given in Figure 2.5a. In addition, as plotted in Figure 2.5b signal to noise ratio (SNR) of Dimers/trimers was 57 % greater (1.57) than SCs, 85% to BCs (0.23) and interestingly 36 % higher to the standard Resovist (1.0) respectively. Similar to the explanation of MH, the enhancement of MPI signal may correspond to the linear dipolar coupling and improved anisotropy of the nanocubes. This statement can be justified because, in fact the MPI relaxometry follows the same principle of MH, as mentioned earlier. In other words, the relative high M_s of Di/tri[86] with respect to SCs and BCs could also be seen as an additional reason for such good performance. In comparison to Resovist, our Di/tri have 36% greater performance due to the fact that, Resovist reportedly has a broad size distribution whose size ranges between 5-24 nm and only 3% of its iron mass contributes to the MPI signal, because the core size around 5 nm does not participate in signal generation.[166,167] The poor performance of bigger clusters can be explained due to the random orientation of cubes in the clusters where they undergo magnetic frustration resulting from very strong dipolar interactions giving rise to demagnetization effect[66,170] and compromises the spontaneous response to magnetic fields, thus lowers the MPI signal.

We have determined, if any temperature changes occurred in the dispersion during the measurement. Infact, no such significant changes are noted, as it was performed at very poor magnetic excitation field strengths. Corresponding differences of temperature achieved by each structure from before to after magnetic excitation are given in Table 2.1.

Samples in Water (Conc: 0.48mg/ml, volume: 250ul)			
Sample name	**Initial Temp. (°C)**	**Final Temp. (°C)**	**dT**
SCs	**21.09**	**21.1**	**0.01**
Di/tri	**21.08**	**21.11**	**0.03**
BCs	**20.75**	**20.78**	**0.03**
Resovist	**20.8**	**20.82**	**0.02**

Table 2.1. Describing the temperature difference achieved by each nanostructure from before to after excitation with magnetic fields of 16.8 kHz and 20 mT.

2.3.2.2 MPI signal of 2D-magnetic nanobeads produced from high interacting IONCs

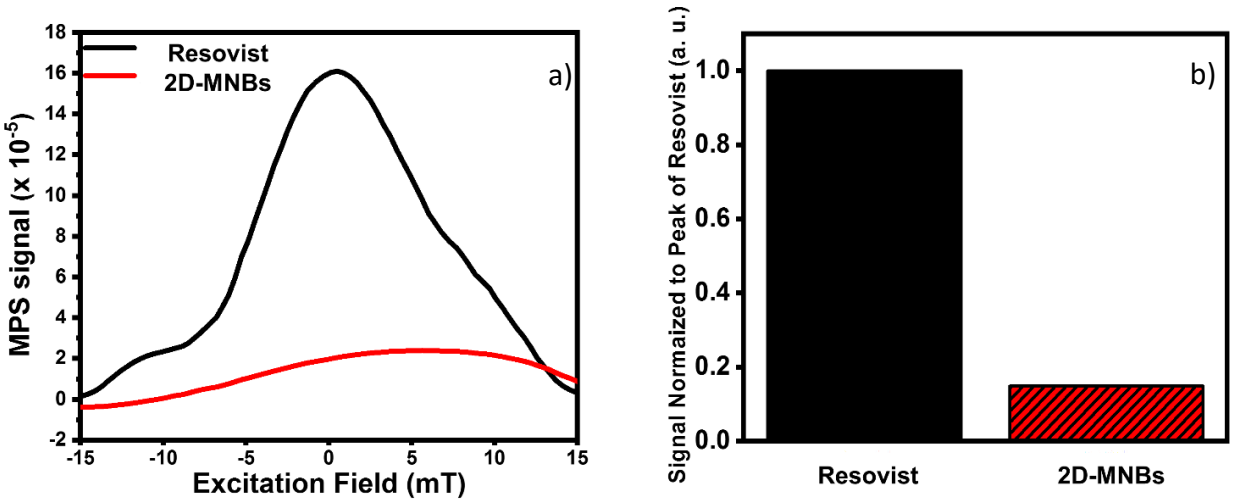

Figure 2.7 The MPI signal a) the point spread function of 2D-magnetic nanobeads compared to the intensity peak of Resovist, b) Corresponding signal to noise ratio of 2D-MNBs.

Following a similar MPI analysis 2D-MNBs were also studied separately at a fixed iron concentration of 0.5 mg/mL (450µL of water) and compared with normalized MPI signal of Resovist under same magnetic excitation fields (16.8 kHz and 20 mT, Figure 2.7). The PSF of 2D-MNBs have given a broad asymmetric peak, which was 8 times less intense than that of Resovist as shown in Figure 2.7a. The full width and half maximum (FWHM) value of 2D-MNBs was 17.6 mT, while it is 15.6 mT for Resovist (Lower this value greater the resolution). Indeed, its SNR ratio is approximately 82 % lower than Resovist. The reason can be ascribed to its morphological factor and frozen configuration of nanocubes within the 2D-MNBs.[64,84] Indeed, the IONCs arranged in planar form have fixed spatial configuration, whose interparticle distance was already frozen within a polymer (refer to TEM in Figure 2.7 c-d).

Moreover they present a large hydrodynamic size (please refer to chapter 1, Figure in 1.22). This large hydrodynamic size may be more an artifact as the DLS uses a spherical model for the calculation of the hydrodynamic size and the "D-MNBs do not really correspond to such configuration. However, nanocubes experience a partial antiferromagnetic dipolar coupling coming from adjacent particles.[76,79] This effect in turn, disturbs the inheritant magnetization reversal process, thus results in partial demagnetization with a clear MPI 2D-MNBs signal poorer than that of Resovist.

2.3.2.3 MPI signal of 2D-MNBs after esterase

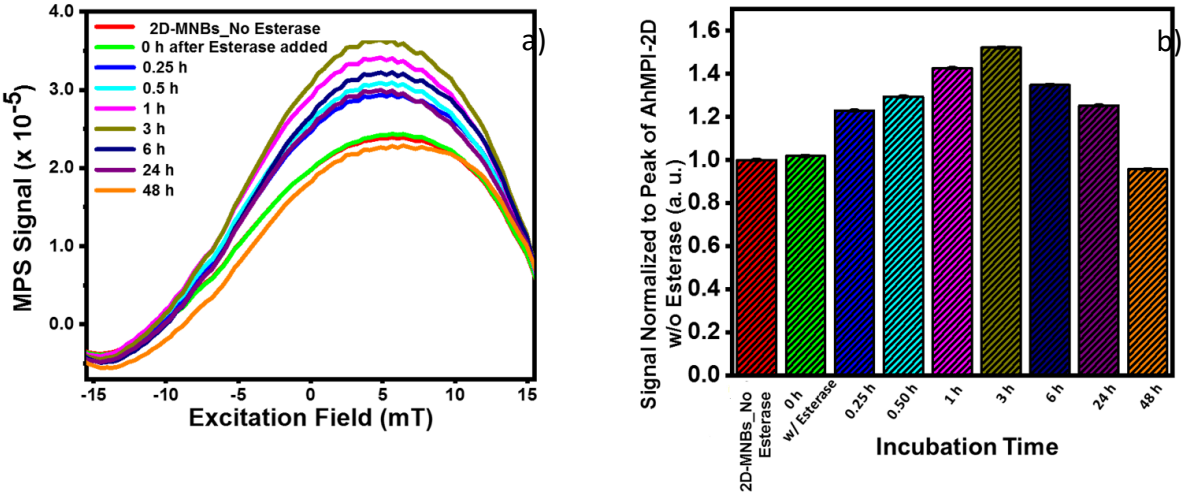

Figure 2.8 a) the point spread function, MPI signal peaks of 2D-MNBs after adding esterase enzyme, obtained at different time intervals during incubation at 37°C. b) Corresponding signal to noise ratios of MPI signal.

In chapter 1, Figure 1.25, we have demonstrated the disassembling of 2D-MNBs into short chain like structures when incubated with enzyme that was associated with an increase of SAR. Inspiring from this work, here we have replicated the same experiment, now for understanding how the MPI signal of 2D-MNBs varies in presence of the esterase enzyme. For this purpose, esterase enzyme was added to a aqueous suspension of 2D-MNBs (450µL at iron concentration of 0.5mg/mL), incubated for 48h at 37°C and the MPI signal was recorded at different time intervals, during incubation (0h, 0.25h, 0.5h,1h, 3h,6h, 24h and 48h). At an ideal magnetic field frequency conditions, signal PSF peak of 2D-MNBs appeared evolving gradually with time and achieved a maximum signal after three hours of incubation. At longer incubation time its intensity began to shrink, as we can spot it from the first glance of Figure 2.8a. In addition, their SNR was also increased, following the same trend with an approximate increase

of 36% in comparison to the signal of the 2D-MNBs before addition of the enzyme (Figure 2.8a). Surprisingly, this trend perfectly fits with the SAR data in presence of esterase enzyme (see section 1.3.7, Figure 1.25, the maximum SAR value was achieved after 3h of incubation and declines at longer times). Likewise, the reason for MPI enhancement can also be explained by the formation of short nanocube chains found upon polymer cleavage.

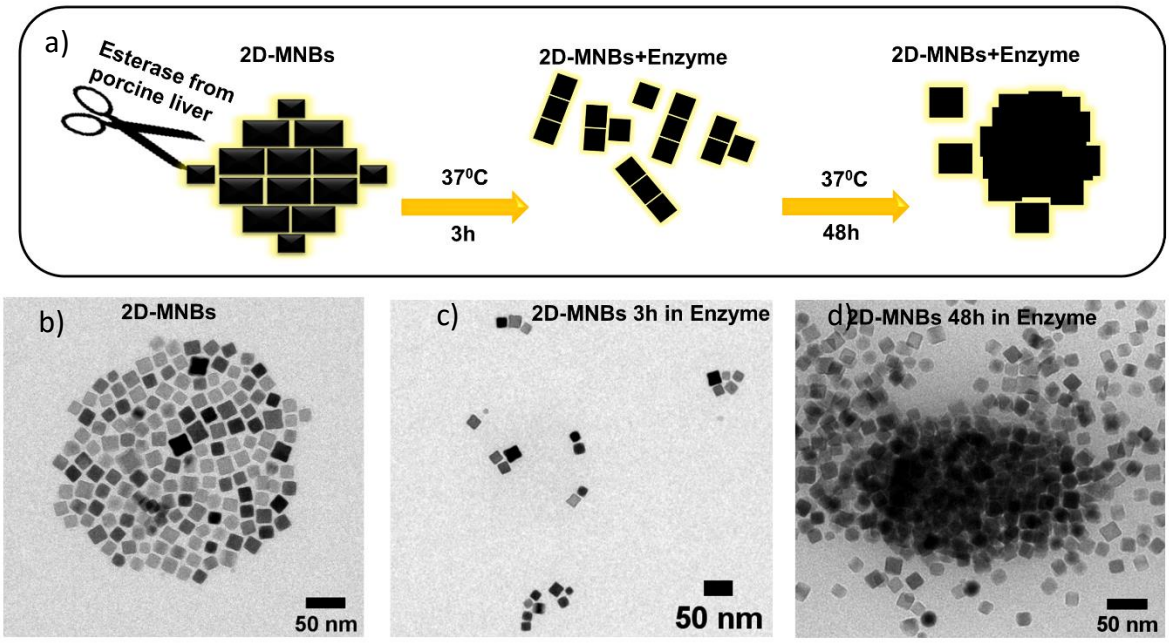

Figure 2.9 Scheme showing the treatment and concomitant breaking of 2D-MNBs in presence of esterase enzyme, that incubated at 37°C for 48 h. b-d) TEM images of 2D-MNBs, b) before adding enzyme, c) after 3h incubation with esterase enzyme and d) after 48h incubation with esterase enzyme.

Under TEM characterization we have observed that the 2D-MNBs (Figure 2.9b), after 15 min of enzyme treatment, began to lose their 2D shape (Figure 1.25d), that interestingly, corresponds to an increase of MPI signal and SNR by around 18% (blue peak and bar in Figure 2.8). On further incubation, at 3 h, the TEM images showed the existence of a chain-like configurations (Figure 2.9c), which was accompanied with a maximum increase of signals than that of the initial 2D-MNBs (Figure 2.8). Such MPI signal increase can be understood due to the fact of short chains of IONCs, as a result of the magnetic dipolar coupling, behave as elongated entities with a single and large magnetic momentum, whose magnetic easy axis was expected to have higher saturation magnetization and respond quickly to magnetic fields.[86] TEM image at 48h (Figure 2.9d) of incubation revealed the presence of nanocubes as large aggregates. These observations support why MPI signal progressively declines towards 48 hour

time point, due to their random dipolar coupling and consequent demagnetization effect as explained before.

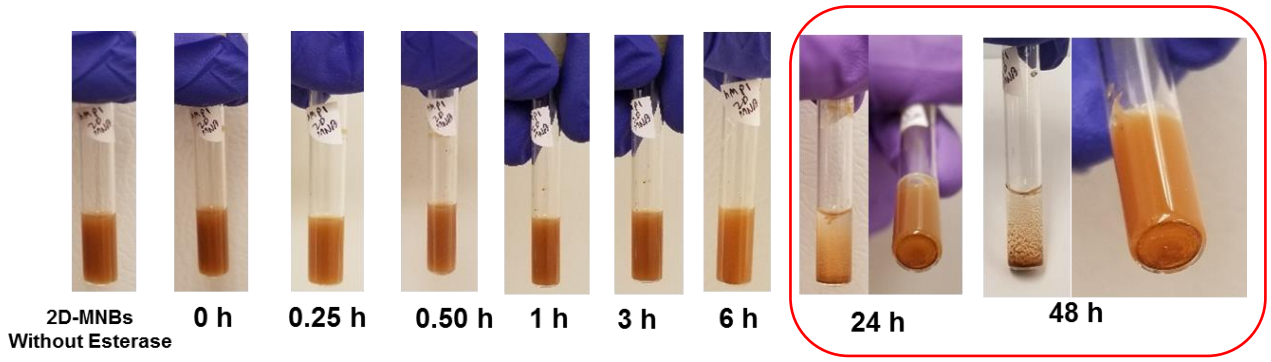

Figure 2.10. Photographs showing appearance of 2D-MNBs suspension at different time points of incubation with esterase enzyme at 37°C. The images highlighted in red panel corresponds to 24h and 48h incubation where the sample tends to precipitate.

As presented in Figure 2.10, it is important to highlight, the macroscopic dispersity of 2D-MNBs have not been affected up to 6h of incubation, but, thereafter it tends to sediment at 24h and 48h, which can be attributed to large aggregates observed under TEM image of Figure 2.9d. These data together with observations of Dimers/trimers suggest that the chain configuration of nanoparticles is advantageous for MPI as well as for MH.

2.3.3 Magnetic resonance imaging relaxivity of nanoclusters

2.3.3.1 Magnetic resonance relaxivity of nanoclusters from Cs-IONCs

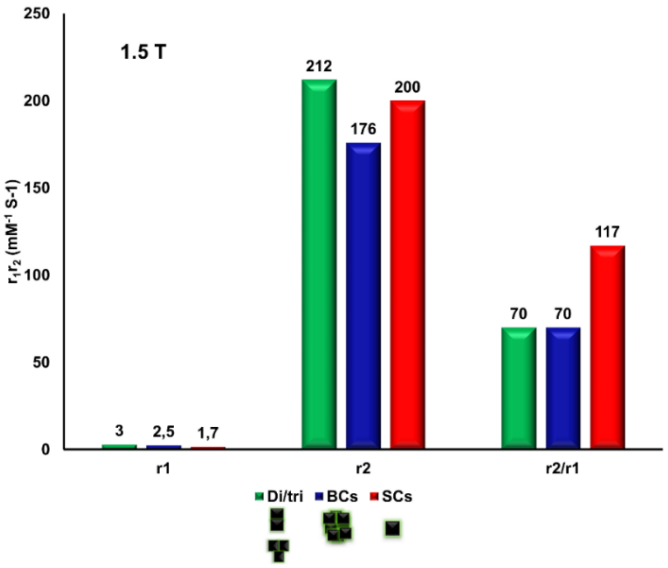

Figure 2.11. Relaxation constants; r_1 (longitudinal relaxation rate) and r_2 (transverse relaxation rate) of nanoclusters produced form core-shell IONCs dispersed in water, measured at 1.5 T, with corresponding relaxation ratios.

Along with MPI studies, the proton relaxation times r_1 and r_2 of Di/tri were investigated and results were compared to that of SCs and BCs produced from the same batch of nanocubes (Figure 2.11). Relaxation measurements of each sample was measured in the linear range at the concentration range in between 0.009 - 0.6 mM at 1.5 T of static magnetic fields. The iron oxide nanoparticles (T_2 agent) used for preparing clusters are expected to induce a transverse relaxation (r_2) to offer negative contrast in MRI imaging.[34,171] Accordingly, all the clusters have fair r_2 relaxation time values, which are greater than most commercial T_2 agents.[172] Among the three structures, the r_2 relaxation times of Di/tri and SCs are comparable to each other with absolute values of 212 and 200 $mM^{-1}s^{-1}$, while it is reduced to 176 $mM^{-1}s^{-1}$ for BCs. The higher values of Di/tri and SCs can ascribed to their higher saturation magnetization with respect to BCs.[86] The hydrodynamic size of SCs and Di/tri is around 30±2 nm and 35±3 nm respectively, which suggests that the structures are in the static diphase regime, where the r_2 values reaches their highest values. Instead, if cubes were aggregated as bigger clusters of hydrodynamic size around 117 ± 6 nm, they fall in the size region beyond echo limit where the decrease

in the r_2 value was expected with increase in size.[173] In all the cases r_1 values of structures are poor which was expected for iron oxide nanoparticles.

When considering the relaxation ratios (r_2/r_1), the highest ratio was obtained for BCs with an absolute value of 117 $mM^{-1}s^{-1}$. Indeed, these observations are perfectly merging with the results previously published by our group[64]. In that study, the high interacting IONCs of size 23 nm were assembled into bigger clusters of size around 173 nm (dH) having lower r_2 values than their isolated forms. But their corresponding r_2/r_1 ratios are well pronounced; 200 $mM^{-1}s^{-1}$ for bigger clusters and 33.8 $mM^{-1}s^{-1}$ for isolated particles. Similar results were observed in the work of Qin et al.,[174] where an enhancement of r_2/r_1 occurred in SPIONs embedded in PF127 triblock polymer and the poly(propylene oxide)/oleic acid.

2.3.3.2 Magnetic relaxation of 2D magnetic nanobeads

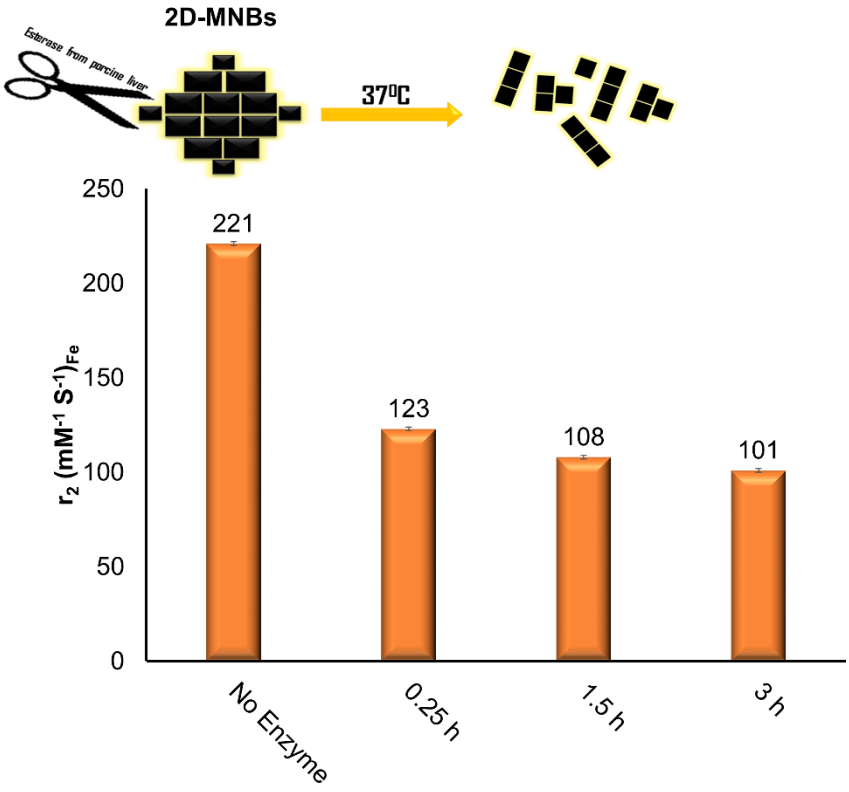

Figure 2. 12 The transverse relaxation rates (r_2) of 2D-MNBs, from before to, after incubation with esterase enzyme at 37°C, determined from the linear slopes of inverse relaxation time of water proton; $1/T_2$. Corresponding values of relaxation r_2 constants are given within the plot. Scheme next to plot representing the disassembly of 2D-MNBs on its treatment with enzyme on 3h of incubation.

We have also studied magnetic relaxation profile of 2D-MNBs under static magnetic field of 1.5 T. Considering their large hydrodynamic size, the samples of 2D-MNBs for measurements are prepared in 0.3 % agarose solution in order to prevent aggregation. Here the concentration range varies between 0.009-0.6 $mM^{-1}.s^{-1}$. Figure 2.12 elucidate the change of relaxation of 2D-MNBs on exposure to esterase enzyme with respect to that of pure 2D-MNBs. As we can see, the pure 2D-MNBs exhibited highest r_2 relaxation constant of 221 $mM^{-1}.s^{-1}$. The magnetic moment of each nanoparticle in assembly, synergistically contributes to enhance r_2 relaxation, since the response is directly proportional to the overall magnetic moment. In addition this value is comparable to the r_2 value of Dimer/trimers. Surprisingly, T_2 measurements performed on 2D-MNBs immediately after the addition of enzyme (sample named 0h of incubation) have shown 44 % reduction in relaxation constant; r_2 value of 123 $mM^{-1}s^{-1}$ Upon further incubation, the T_2 values gradually decrease with time having a value of 108 $mM^{-1}s^{-1}$ at 1.5h and 101 $mM^{-1}s^{-1}$ at 3h respectively. However, these values after enzyme disassembly are efficient enough and comparable with other commercial particles. The decrease of T_2 signal overtime with enzymatic digestion could be preferred because it may reduce the interference to monitor some organs using MRI. Longitudinal relaxation rates of all points could not be recorded because of the uncertainty, as the relaxation time values are saturated with values similar to that of water molecules (data not presented).

2.4 Conclusions

Magnetic particle imaging is a potential real time imaging tool. Moreover, if this is combined with conventional MRI, would possible to obtain real time anatomical details as it was already to adopt in some preclinical applications. In this work, we have measured magnetic particle imaging and magnetic resonance imaging properties of anisomeric structure developed from iron oxide cubic shape nanoparticles of different composition and compared to Resovist, “gold standard”. Owing to improved anisotropy and linear dipolar coupling, cubes in Dimeric/Trimeric form performed as best MPI agent with 36 % greater signal than Resovist. While the initial planar 2D-MNBs have poor signal, however, interestingly, this signal progressively evolved with time upto 3h, when incubated with esterase enzyme at 37°C. Such a raise can be attributed to the breakdown of planar beads into short chain like forms similar to dimer/trimers. Besides, all these structures, given a very high transverse relaxation

properties than many other commercial T_2 agents for negative contrast in MRI imaging. Overall, our structures with MPI and MRI properties can be implemented as theranostic nanoprobes. These kind of advanced materials could guide in obtaining real time, precise anatomical details of diseased region for better treatment planning and same materials can be excited to generate heat for treatment, thus can avoid multiple injections which can cause discomfort to the patients. In addition enzyme responsive signal enhancement of 2D-MNBs was remarkable, as they can be activated within the intracellular enzyme rich environment.

3. Multifunctional Enzyme Responsive Nanoprobe for Theranostic Applications

3.1 Introduction

Magnetic hyperthermia (MH) is a unique thermo-therapeutic approach to heat tumor mass, produced by MNPs in response to oscillating magnetic excitation fields, currently in clinical practice for the treatment of solid tumors such as brain and prostate cancer.[28,30] Nevertheless, if injected through systemic routes, it lacks efficiency, because we do not know when the desired site achieved sufficient magnetic reservoirs after the injection and when to initiate the application of alternative magnetic fields (AMF). For that, often tracking the target site through diagnosis is necessary. In such a scenario, multifunctional nanoprobes with theranostic features were advantageous and recently attaining a great deal of interest.[175–177] Magnetic resonance imaging (MRI) is a non-invasive and powerful bio-imaging tool in gaining submillimeter range image resolution.[178,179] By combining, MRI imaging abilities together with MH into single platform not only helps in detecting optimal reservoirs of material concentration at target site to initiate treatment, but also assist in spontaneous viewing of treatment progress that induced by MH, through simultaneous imaging, thus helps to avoid multiple injections of materials. In 2015, our group reported the preparation of magnetic nanobead (MNBs) using high efficient iron oxide nanocubes (IONC)[103] with heating and T_2 transverse relaxation properties.[83] Despite their efficiencies, the sole use of IONCs, as T_2 contrasting agent, especially at concentrations of MH may associate with few ambiguities.[2] Basically, superparamagnetic compounds like IONCs at high concentration could create huge magnetic susceptibility out of accumulated site at proximities, thus notoriously darkens even the surrounding health tissue, thus may create a confusion in identifying/differentiating normal tissue from the affected one.[10] For reducing such artifacts, many proposed dual image modalities, like merging T_1 and T_2 properties in a single probe that facilitates a provision to switch between contrasts of our choice.[180–182] For instance yang *et al*., developed such $Fe_3O_4/SiO_2/Gd_2O(CO_3)_2$ core-shell structures with dual contrast abilities (T_1-T_2 properties).[183] Besides this, so far none reported combining hyperthermia as a treatment source in such nanoprobes with artifact filtering T_1-T_2 dual imaging abilities. It is worthy to mention, Santra *et al*., reported

encapsulation of Gd^{3+} chelates in a polymeric assembly of IONPs with above mentioned abilities. Nevertheless, the inclusion of less efficient IONPs hindered the idea of applying for MH. Even though the various Gd^{3+} chelates currently available in market were FDA approved[184,185] and extensively used, because of its unique paramagnetic feature with seven unpaired electrons that can induce longitudinal spin relaxation of water proton (T_1/positive agent), thus brightness the image. But, their usage was reportedly associated to some kidney related toxicity issues (Nephrogenic Systemic Fibrosis), due their molecular level leakage[179,186]. Therefore embedding Gd^{3+} ions in a rigid matrix such as in inorganic nanoparticles, could be a right strategy of designing, not only for better T_1 performance and increasing circulation time,[187] but also to reduce the toxicity concerns by preventing the free leakage[188].

In addition, as emphasized in chapters 1 and 2, nanoprobes responsive to tumor microenvironment, for instance acidic pH or enzymes responsive [178,189] were also gaining immense interest in recent days. Inspired by them, we initiated a work in constructing a theranostic nanoplatform composed of magnetic IONC as the main and efficient material for MH, and also T_2 contrast agent for MRI,[83,103] and gadolinium-based nanoparticles as a paramagnetic shell for T_1 relaxation, as schematized in Figure 3.1. It is important to note, merging of both the particles in an unorganized way, suppose, if both the modalities are in very close contact, it is much likely to cause the quenching of T_1 abilities of Gd^{3+} ions, because of magnetic susceptibility coming from IONCs.[190]

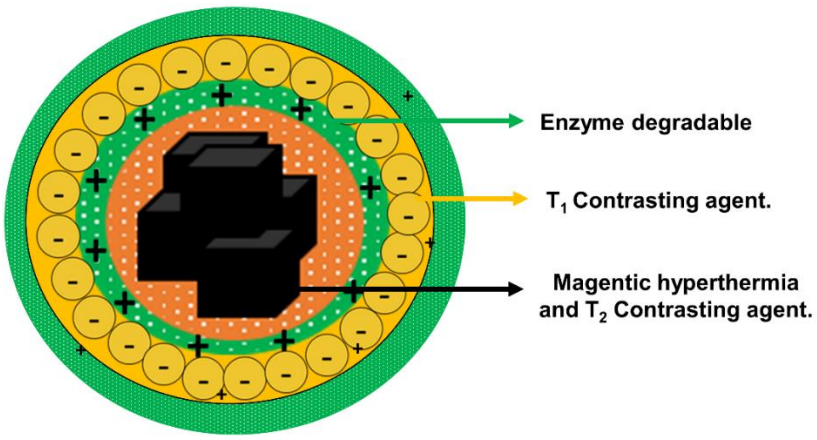

Figure 3.1. The scheme of multifunctional nanoprobe with theranostic properties, prepared in this project.

Therefore, as a novel route, we adopted our recently published layer-by-layer (LbL) approach [191] to synthesize composite structures of IONCs embedded in a polymeric bead as core MNBs, on which

negatively charged, water-soluble polyacrylic acid (PAA) coated $NaGdF_4$ NPs (PAA-$NaGdF_4$ NPs) were packed using intracellular protease[192] degradable polymer spacers Poly-L-arginine hydrochloride (PARG), thorough electrostatic interactions. We evaluated the layering process by analyzing shifts in surface charge potential. We have analyzed heating abilities and T_2 properties of MNBs, before and after layering, similarly the T_1 properties of PAA-$NaGdF_4$ NPs. Exploiting the intracellular environment of the tumor, upon protease treatment, we demonstrated changes of relaxations and morphologies when detaching the PAA-$NaGdF_4$ NPs from the magnetic bead surface. However, since it is an ongoing project, we have to conclude some more results with additional experiments and have to replicate in *in vitro* models that we will be planning in nearby future.

3.2 Materials and Methods

3.2.1 Materials

All chemicals for this work were obtained from Sigma-Aldrich and used without any further purification; Gadolinium (III) oxide (Gd_2O_3), Oleic acid (90%), trifluoroacetic acid (tfa), sodium trifluoroacetate, oleylamine (98%), tetrahydrofuran(99%), Poly(maleic anhydride-alt-1-octadecene) (PC18, Mn 30 000−50 000, Aldrich), Milli-Q water (18.2 MΩ, filtered with filter pore size 0.22 μM) from Millipore, Chloroform ($CHCl_3$, Sigma-Aldrich, 99%), poly(acrylic acid) (PAA) and liver porcine esterase(Sigma Aldrich). 1-octadecene (1-ODE, 99%), Poly-l-arginine hydrochloride (PARG, Mw > 70 kDa, no. P3892), protease (no. P5147).

3.2.2 Synthesis of ironoxide nanocubes

Iron oxide nanocubes of edgelength 14±2 nm prepared by thermal decomposition method, capped with oleic acid as surfactant and dispersed in $CHCl_3$.(under patenting process, Application No: IT 102019000006469, Inventor: T. Pellegrino et al., filed on 30 April, 2019).

3.2.3 Synthesis of $NaGdF_4$ nanoparticles

The sodium gadolinium fluoride inorganic nanoparticles of size 7.5±0.7 nm ($NaGdF_4$) were produced at IIT, by thermal decomposition method, coated with oleic acid and dispersed in $CHCl_3$.[179] In brief, firstly for obtaining Gd^{3+} trifluoracetate precursor (Gd^{3+}tfa) 0.75 mmol of Gd_2O_3 was added to 6 mL mixture of trifluoroacetic acid (tfa) and water (1:1) in a 100 mL three-neck round bottom glass flask. The

mixture heated upto 90° C, under magnetic stirring and reflux, until the solution turns transparent and later dried at 60 °C overnight (dry powder of Gd^{3+}TFA). Subsequently, we injected 1.5 mmol of sodium trifluoroacetate (Natfa), along with 5.3 mL of oleic acid, 10.7 mL of 1-octadecene and 7.05 mL of oleylamine and degassed the mixture at 100 °C under vacuum conditions and magnetic stirring, for 30 min. Once after the mixture turns yellowish (that is an indication of complete dissolution of precursors), solution was heated upto 310°C at a rate of 10°C /min and maintained for 10 min, that was followed by cooling to room temperature. Thus prepared oleate-capped $NaGdF_4$ NPs precipitated by adding 20 mL ethanol and centrifuged at 5000 rpm for 5 min and discarded the supernatant. These particles were repeatedly washed for 3 times by redispersing each time in ethanol and finally dissolved in 20 mL of $CHCl_3$.

3.2.4 Synthesis of standard magnetic nanobeads as core

The procedure of synthesizing of standard MNBs for this project was similar to the method of preparing 3D-MNBs in chapter 1, (section 1.2.7), however implemented with few modifications, which was adopted from our published works.[83] Firstly, 15 µL of the IONCs dispersion (5.4 g_{Fe}/L in $CHCl_3$) and 100 µL of poly(maleic anhydride-alt-1-octadecene) (PC18) (50 mM in $CHCl_3$, that corresponds to monomer units) were introduced into a 8 mL glass vial and sonicated for 3 min at 60 °C. After evaporating the initial solvent from the mixture, using a nitrogen flux, 200 µL of THF was added. Later, the reaction mixture was sonicated for another 2 min at 60 °C. Then, by placing reaction vial on an orbital shaker (1250 rpm), 1.6 mL of milliQ water was injected at a rate of 3 mL/min. The organic solvent in the solution mixture was evaporated slowly at room temperature (RT) while shaking at 1000 rpm, hereafter, beads finally remain in the water. Thus obtained MNBs were washed according to the procedure reported in section 1.2.7 of chapter 1. To scale up the amount of beads, the same protocol was repeated for 20 times and filtered through a hydrophilic filter of 1.2 µM and lastly concentrated to 3 g_{Fe}/L based on iron content.

3.2.5 Water transfer of $NaGdF_4$ NPs using polyacrylic acid

The hydrophobic $NaGdF_4$ NPs of size 7.5±0.7 nm (produced by our previous post doctorate, Dr. Emille Martinazzo Rodrigues) were water transferred using, polyacrylic acid (PAA) according to recently published work with few modifications.[179] Briefly, 1 mL of $NaGdF_4$ NPs dispersion (7.89 g_{Gd}/L in $CHCL_3$)

was introduced under sonication into an 8 mL glass vial composed of PAA solution (48 mg in 2 mL of ethanol) and this reaction mixture was shaken vigorously overnight on an orbital shaker (1250 rpm) under RT. Later, the particles were precipitated by adding cold diethyl ether (DEE); the ratio of DEE to reaction volume maintained was 8:1 and, that later centrifuged for 10 min at 3000 rpm. After centrifugation, the white pellet of nanoparticle was carefully collected by discarding the supernatant. Then, again the pellet was dispersed in 6 mL of acetone with the assistance of sonication and repeated centrifugation. This step of washing with acetone was repeated thrice in order to assure complete removal of organic ligand. Before dissolving in water, the organic traces from final pellet were vaporized using nitrogen flux. Once after dispersing in 1 mL water, this PAA-$NaGdF_4$ NPs were washed twice through Amicon filter of 100 kDa to exclude excess and free PAA and at the end re-dissolved in 1 mL water. As determined by ICP, the yield of the reaction was almost 93 %.

3.2.6 Layer-by-layer process of merging PAA-$NaGdF_4$ NPs on MNBs

The Procedure for systematic layering of PAA-$NaGdF_4$ NPs on to the surface of MNBs was adopted and modified from recently published work.[193] For this, 1 mL aqueous suspension of MNBs (0.5 g_{Fe}/L in water) was injected dropwise under sonication into 8 mL glass vial filled with 1 mL of positive charge polymer, poly-l-arginine hydrochloride (PARG (Mw > 70 kDa, no. P3892), 1 mg/mL in 50 mM NaCl solution, pH 7.2). After incubating this reaction mixture for 1 hour at RT on orbital shaker (1250 rpm), the PARG coated beads (MNBs:PARG) were collected as pellet to a permanent magnet (0.3T). The non-interactive, free PARG in supernatant was extracted and preserved for further use. Later, the dark pellet was re-dispersed in a milliQ water and repeated magnetic washes at least thrice before final dispersion in 1 mL of fresh milliQ water. For second layer, 1 mL PAA-$NaGdF_4$ NPs water dispersion (1 mg/mL in water) was added dropwise into 1 mL solution of MNBs:PARG under sonication (3 min) and subsequently incubated for another 1h on orbital shaker at 1000 rpm. Similar to the above, we extracted non-coordinated PAA-$NaGdF_4$ NPs as supernatant by collecting structures to magnet and repeated three washings with water to make free of any non-coordinated particle. Lastly, these structures (MNB:PARG:Gd) were prepared for next layering by dissolving in 1 mL of fresh millQ water. For third layering, we repeated the first layering process on MNB:PARG:Gd by re-using PARG extract preserved in the beginning. After magnetically washing for three times, the final product, MNB:PARG:Gd:PARG was dissolved in 500 µL of milliQ water for further investigations.

3.2.7 Quantification of iron and gadolinium

The iron and the gadolinium contents were quantified by elemental analysis using an inductive plasma atomic emission spectrometer (ICP-AES, iCAP 6500, Thermo). Prior to the measurements, the samples were subjected to overnight digestion in Aqua Regia before being diluted with water for the final analysis.

3.2.8 Dynamic light scattering and TEM imaging

The hydrodynamic sizes (dH) of the nanostructures were determined according to the procedure described in section 1.2.9 of chapter 1. The structure and morphology of the all structures were investigated under transmission electron microscopy (JEOL JEM-1011), which operated at an accelerating voltage of 100 kV. Diluted aqueous solutions of samples were deposited by drop-casting, and they were allowed to dry under room temperature for 12 hours.

3.2.9 AC magnetometry measurements

Magnetometry measurements were carried out at a fixed iron concentration of $3 g_{Fe}/L$, using frequencies of 300 kHz and 100 kHz, and a magnetic field amplitude of 16, 20 and 24 kA/m at RT, according to procedure described in section of 1.2.16. Afterwards, SAR values were calculated according to SAR= $A \cdot f$,[131] where A is the magnetic area and f is AC magnetic field frequency.

3.2.10 Calorimetric SAR measurements

The heating efficiency of water-dispersible MNBs was evaluated by calorimetric and magnetic measurements. Calorimetry measurements were performed at different fields (range from 16-$24 \mathrm{kAm}^{-1}$) and frequencies of 110 and 300 kHz, using DM 100 Series (nanoScale Biomagnetics Corp), a commercially available instrument. For the measurements, 300 µL of an aqueous suspension of the MNBs (at an iron concentration of 3 g/L) was first sonicated for 1 minute, then they were introduced into the sample holder, according to the procedure given in section 1.2.14 of chapter 1. In addition, temperature raise profile of the MNBs and MNBs:PARG:Gd:PARG was recorded on 1 hour continues exposition to the AMFs of frequency 300 kHz and field of 16 kA/m ($Hf = 4.8 \times 10^9$ $Am^{-1}.s^{-1}$). For this experiment, temperature raise was recorded using an optic fiber thermosensor (LumaSense) from 300 µL of water-dispersed structures ($3 mg_{Fe}/mL$).

3.2.11 Relaxivity Measurements

Water solutions of MNBs and PAA-$NaGdF_4$ NPs with an iron and gadolinium concentration ranging from 0.01 to 1 mM were prepared. The longitudinal (T_1) and transverse (T_2) relaxation times were measured at 40 °C using a Minispec spectrometer (Bruker, Germany) mq 60 (1.5T) and mq (0.5 T) and derived r_1 and r_2 relaxation profile according to procedure described in section 2.2.6 of chapter 2.

3.2.12 Relaxivity of MNBs:PARG:Gd:PARG after enzymatic cleavage

Similarly to above, the relaxivity of MNBs:PARG:Gd:PARG was studied under 1.5 T static magnetic field in 0.3 % agarose aqueous solution, whose concentration varied between 0.3 mM to 0.005 mM (based on Gd^{3+} ion). Once after this, each dilution was supplemented with 10 µL of protease solution (1.6 mg/mL in tris buffer pH 7.6) and incubated at 37°C that mimics the temperature of biological environment. Subsequently, re-measured relaxations under same conditions, at different time points of 15 min, 1 h, 3h, 5h, 24h and 48 h respectively. To note, before measuring, samples were sonicated for 30 sec.

3.3 Results and Discussion

With a clear intention of developing a multifunctional nanoprobe, with combined MH and MRI (both T_1 & T_2), we have adopted a unique layer-by-layer (LBL) technique to build desired morphology. For simplification, the procedure for construction of structure was divided into three step; 1) Production of MNBs; heat mediating agents for MH and T_2 contrasting agents in MRI (image darkening). 2) Water transfer of hydrophobic $NaGdF_4$ NPs; a source for T_1 contrasting (image brightening) in MRI and 3) Fabrication of multifunctional nanoprobe by merging $NaGdF_4$ NPs on MNBs through LBL process.

3.3.1 Production of magnetic nanobeads

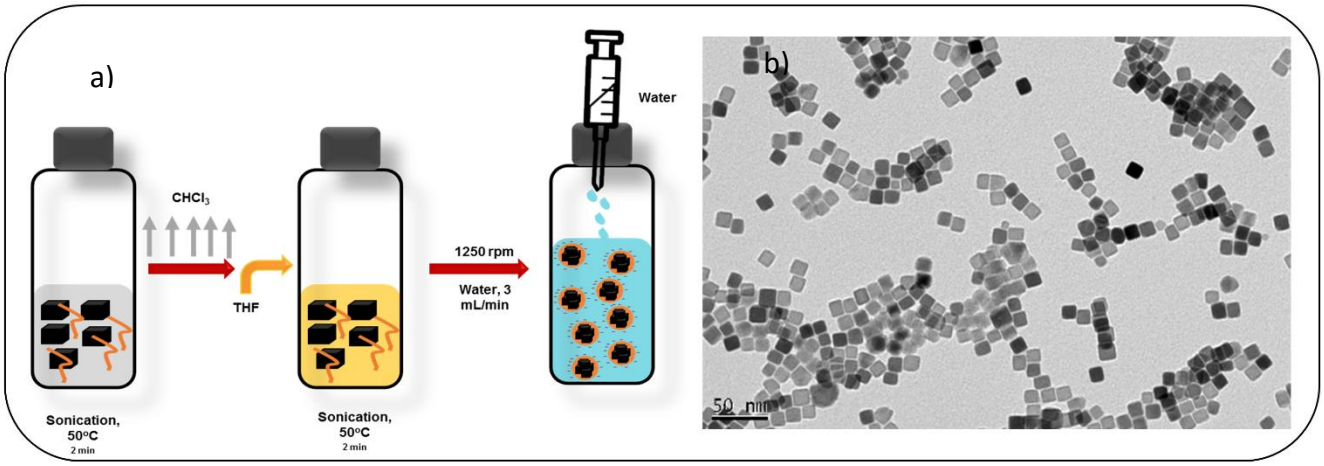

Figure 3.2. a) Schematic overview of synthesizing magnetic nanobeads to function as heat mediators and simultaneously as transverse relaxation agent for MRI. b) TEM image of as-synthesized IONC in $CHCl_3$.

As demonstrated in the scheme of Figure 3.2a, the magnetic nanocubes of hydrophobic properties were clustered within the hydrophobic moiety of amphiphilic polymer into three dimensional geometries named as magnetic nanobeads (MNBs). The IONCs of egdelength 14±2 nm (Figure 3.2b), synthesized by Dr. Helena Gavilan Rub from our group at IIT, which were capped with oleic acid and dissolved in $CHCl_3$, mixed with a stock solution of PC-18 in $CHCl_3$. After constant sonication for 3 min at 50° C, organic solvent from the mixture was evaporated using a nitrogen flux.

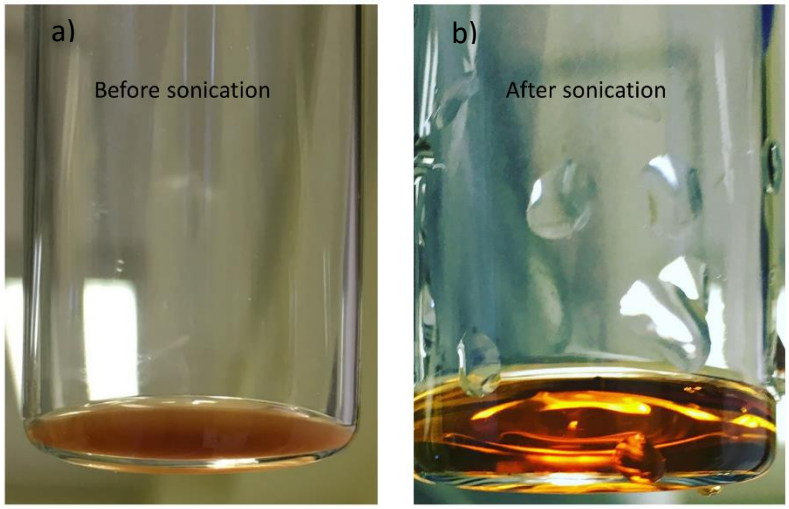

Figure 3.3. The appearance of IONCs and PC18 mixture in $CHCl_3$, a) before and b) after sonication at 50^0C for 5 min. The clear, non-cloudy appearance after sonication indicates the uniform distribution of particles with instant stability due to the partial intercalation of hydrophobic domains to particles surface.

We assume, this three minutes of sonication plus temperature were crucial for the reaction that may have prompted partial intercalation of polymer's chains to the hydrophobic surface of cubes, thus offers instant stability and prevents unwanted large aggregates. Indeed, as presented in Figure 3.3, the captured photographs clearly highlights our hypothesis, where the initial cloudy solution with a mixture of particles and polymer, transformed into clear and shiny substance after sonication, this somehow indicates the homogenous distribution and stability of the content.

Later, by re-suspending dried materials back in fresh THF, mixture was re-sonicated for another 5 min at 50° C. By keeping the reaction mixture under vigorous shaking at 1250 rpm on an orbital shaker, the polarity of the solvent was gradually changed by injecting milliQ water (destabilizing agent) dropwise in a controlled manner at the rate of 3 mL/min. Consequently, the solubility of materials, alters, firstly collapses the IONCs, because of their interacting behavior and secondly, the hydrophobic domains of PC-18 which entraps IONC into 3D geometry, where negatively charged, hydrophilic moieties of PC-18 extends out into the solution, as a result, structures gain water stability.[83]

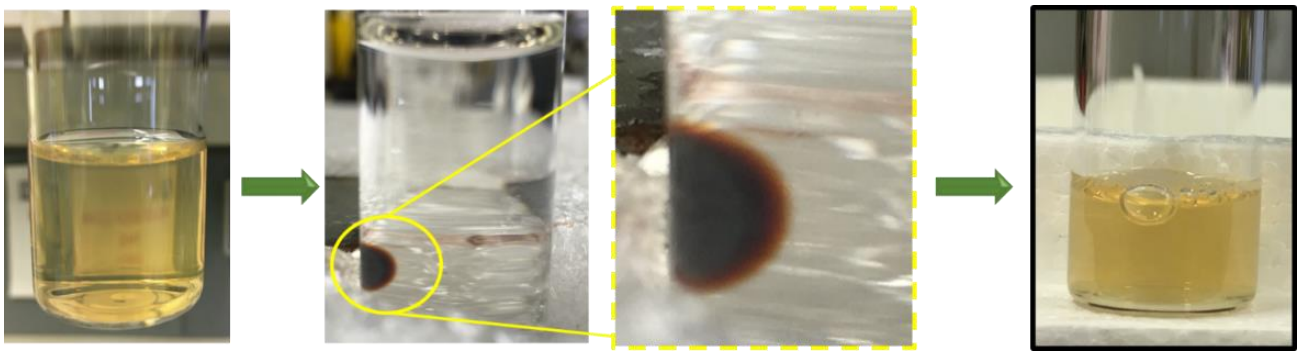

Figure 3.4. Magnetic washing: Digital image of MNBs before magnetic wash (first panel), beads accumulated to the magnet (central panel), beads re-dispersed in water after discarding the first supernatant (right panel).

As demonstrated in Figure 3.4, the unreacted polymer from product was excluded out as supernatant by accumulating magnetic nanobeads to an external magnet of 0.3T. Presence of multiple magnetic nanoparticles in each structure was advantageous, because they responds very quickly to the magnet and thus washing of MNBs became an easy task for us. In another word, this quick response was also crucial if we apply the same for external magnet guided MH, in order to localize the material precisely at the target site guided by external magnet gradients.[33] Despite of *in vitro* models, this approach has to be proven yet in *in vivo* models. By this high magnetic response, as we stated in chapter 1, section

1.3.9, we could withheld all the concentrations at target site, in spite of being interrupted by blood flows or other factors. Once after magnetic washing, beads were filtered through hydrophilic filter of 1.2 µM pore size to eradicate any unwanted aggregations and finally dissolved in 500 µL of borate buffer solution (pH 9). We repeated this entire procedure for 20 times, and lastly merged, and concentrated to 1 mL final volume in borate buffer at concentration of 3.2 mg/mL.

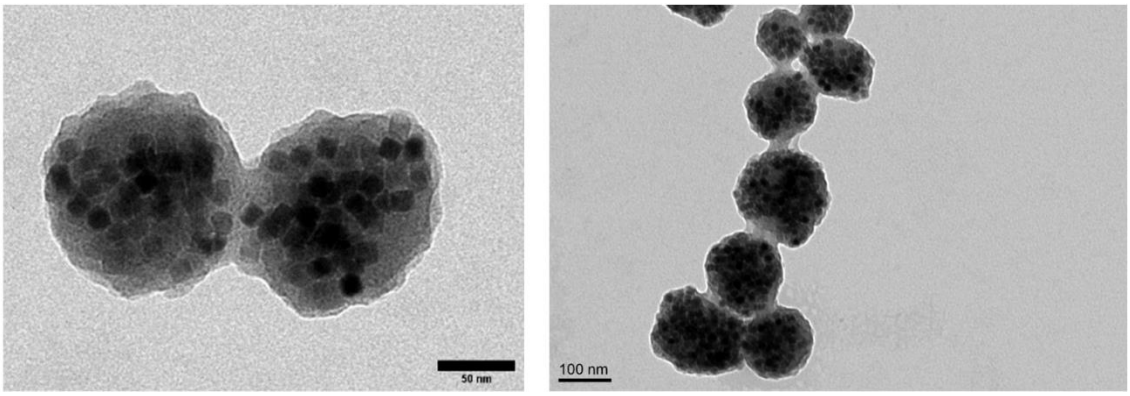

Figure 3.5. TEM image of magnetic nanobeads prepared using IONC and PC-18. Scale bar of first image (50 nm) and second (100 nm).

Transmission electron microscopy images presented in Figure 3.5 and dynamic light scattering data that we will discuss in LBL process (Figure 3.12 peak of MNBs), confirmed pseudo spherical 3D geometrical arrangement of IONCs, entrapped within polymer shell and colloidal water stability with an hydrodynamic size of 213 ±9 nm (PDI=0.1) respectively.

3.3.2 Water transfer of $NaGdF_4$ NPs using polyacrylic acid

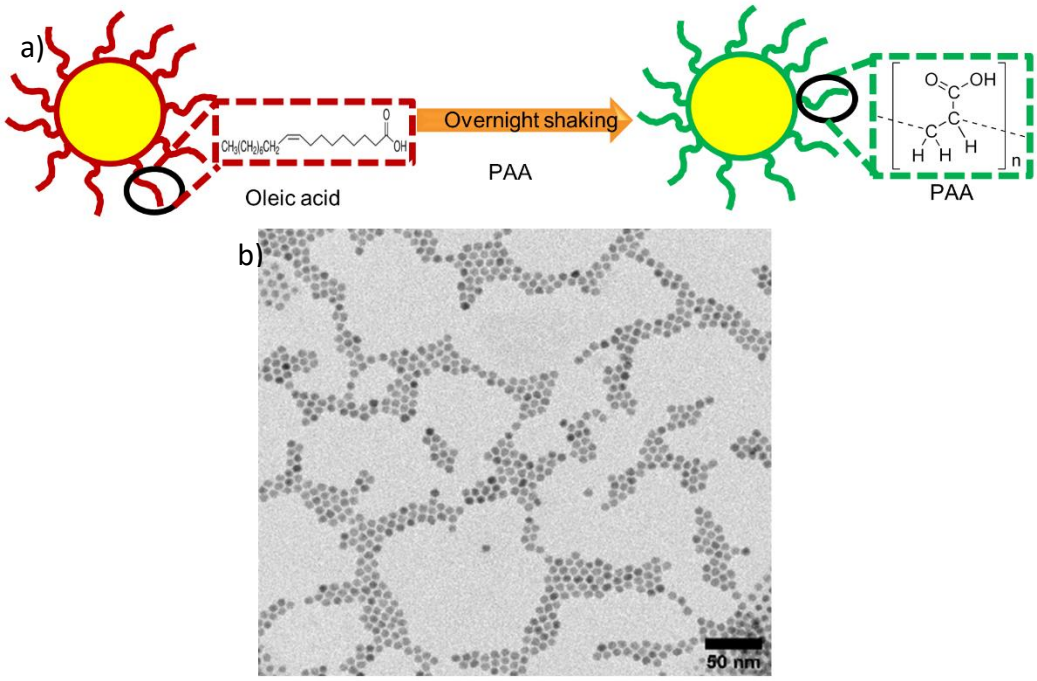

Figure 3.6. a) Schematic picture of water transferring hydrophobic sodium gadolinium fluoride nanoparticles using polyacrylic acid through ligand exchange method. b) Hydrophobic $NaGdF_4$ NPs (size = 7.5±0.7 nm).

The second task involves the water transfer of the hydrophobic $NaGdF_4$ NPs to have a surface negative charge. Being paramagnetic compound, bearing surface negative charge is extremely suggested that was expected to promote close interaction of water proton which is a crucial factor required to promote T_1 contrasting abilities.[181] By choosing commercially polymer PAA as ligand, we adopted and modified recently published work[179] to exchange hydrophobic oleic acid on surface of initial particles as schematized in Figure 3.6a. For this, 7.89 mg of $NaGdF_4$ NPs dispersed in $CHCl_3$ (fig.3.6b) added dropwise under sonication into 48 mg of PAA dissolved in 2 mL of ethanol. After shaking vigorously overnight, the PAA coated particles were precipitated by adding the cold DEE. The DEE being a hydrophobic solvent, PAA coated particles will precipitates apparently. Free oleic acid in solution discarded as supernatant by centrifugation (3 washes; once with DEE and later with acetone). Organic traces from pellet vaporized using nitrogen flux, that before dispersing in water. It is important to clear those traces, since it may disturb particles final stability in water. Now, the excess PAA from product was discarded by washing thrice through 100-kDa Amicon filter and finally dissolved in 1 mL of fresh DI water for further use (7.6 mg_{Gd}/mL).

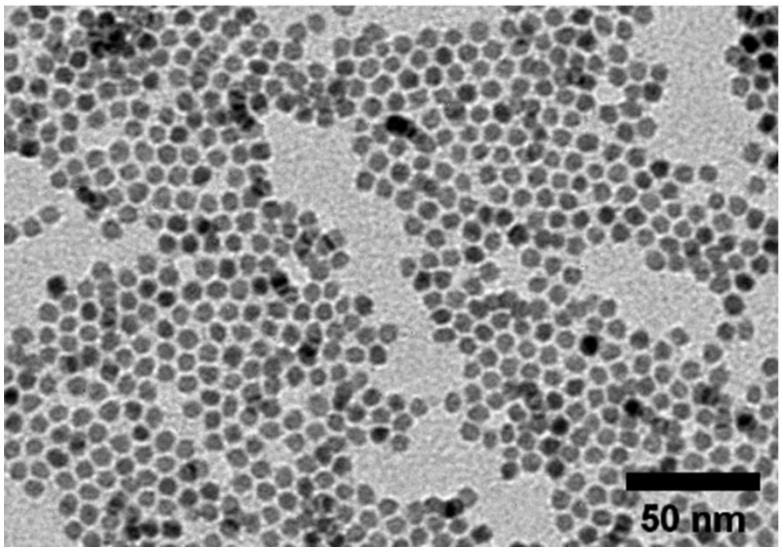

Figure 3.7. TEM image of $NaGdF_4$ NPs coated with polyacrylic acid dispersed in water.

As confirmed by TEM image in Figure 3.7, their initial morphology have not been interrupted and in addition, no signs of aggregations were noted anywhere over the sample grid.

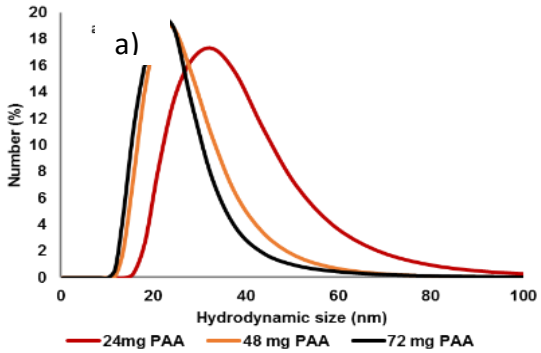

b)

Sample	Number	PDI
24 mg PAA	35±13 nm	0.226
48 mg PAA	25±9 nm	0.226
72 mg PAA	23±9 nm	0.45

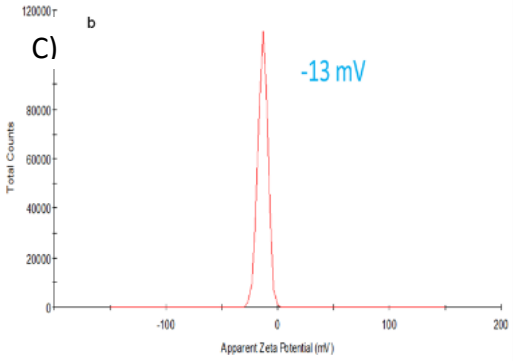

Figure 3.8. a) DLS plots and b) table, showing the trend of narrowing the size peak in DLS, when increasing the amount of PAA from, 24, 48 to 72 mg. c) the surface zeta potential value of water tarsferred PAA-NaGdF4 NPs with 48 mg of PAA.

It is worthy to mention that we also repeated the above reaction using 24 & 72 mg of PAA and realized, polymer increase was advantageous in improving/narrowing the size distribution as given in DLS peak of Figure 3.8a. As tabled in Figure 3.8b, DLS confirmed their aggregation free colloidal stability with a single narrow peaks and the hydrodynamic size range between 25±9 nm to 35±13 nm (PDI 0.226, presented in number %). According to our expectation, PAA coating offered surface negative charge (-13 mV) to the particles (Figure.3.8c) which explains why particles are stable in water which was mainly through respective electrostatic repulsions.

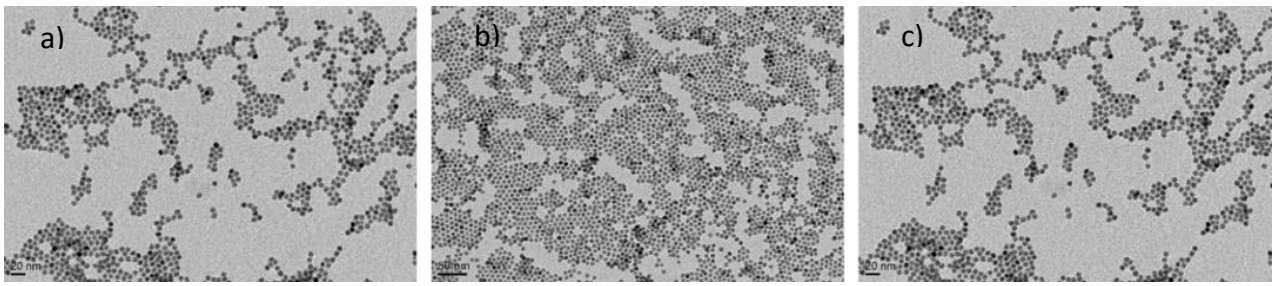

Figure 3.9. TEM images of PAA coated $NaGdF_4$ NPs, at different polymer amount; 24 mg (a), 48 mg(b) and, 72 mg (c) respectively. All scale bars in picture corresponds to 20 nm.

Despite very narrow changes in DLS data, no signs of difference have been seen among three samples, under TEM (Figure 3.9). Anyways, besides the reaction with 24 & 72 mg of PAA, the only reaction with 48 mg of PAA achieved 93 % yield as determined by ICP, while in first two cases it reduced to 60 %. Therefore, we decided to adopt protocol with 48 mg of polymer as ideal conditions for our purpose.

3.3.3 Layer-by-layer approach for decorating PAA-$NaGdF_4$ NPs on MNBs

After individually developing both the domains; the MNBs, (Figure 3.5) as core for heat production and also a source for T_2 in MRI and, PAA-$NaGdF_4$ NPs (Figure 3.7) for T_1 relaxation, the integration process was adopted from recently published work (electrostatic interaction inspired LBL methodology).[194]

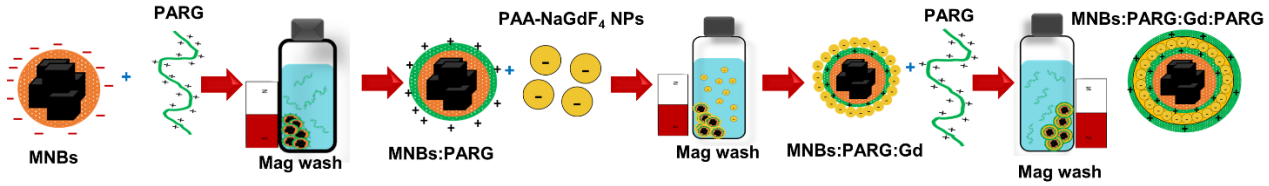

Figure 3.10. Scheme showing stepwise, layer-by-layer growth of degradable PARG and PAA-$NaGdF_4$ NPs on surface of magnetic nanobeads.

The entire method was schematized in Figure 3.10. For this, 1 mL of aqueous solution of MNBs of surface negative charge (0.5 mg_{Fe}/mL) was added dropwise, under sonication, into 1 mL of positive charge polymer, PARG (0.5 mg/mL in 50 mM NaCl, pH 7.6) in 8 mL glass vial. The addition under sonication is crucial to reduce high interacting behavior of MNBs, which was expected to prevent unwanted aggregations. Later, the 1h of incubation on orbital shaker, facilitated wrapping of PARG on MNBs. Hereafter this sample will be termed as "MNBs:PARG". Soon after, the MNBs:PARGs were collected by an external magnet (0.3 T) for 10 min, where upper clear solution that contains non-interactive and free PARG was extracted and preserved for further use. Three more subsequent magnetic washes assured the quality of MNBs:PARG (re-dissolved in 1 mL of water) that was free of non-interactive polymer.

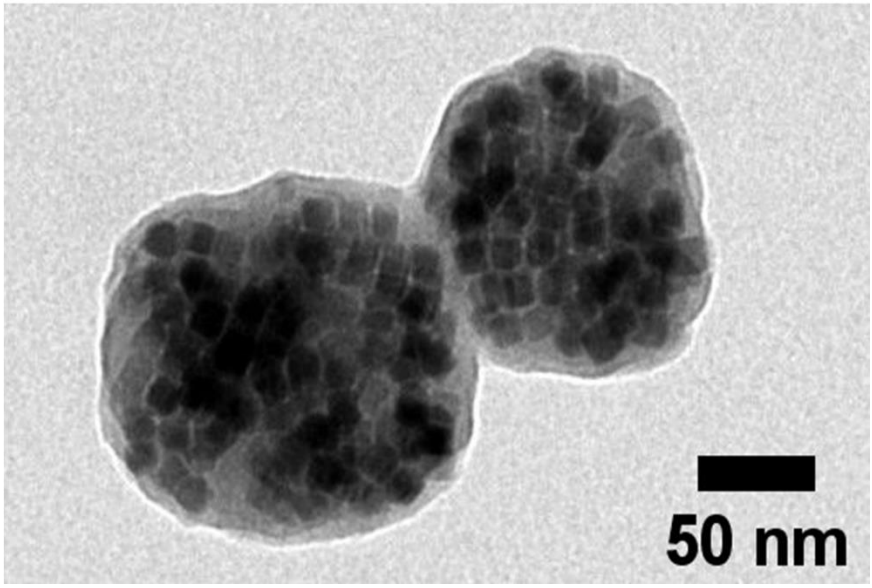

Figure 3.11. TEM image of the MNBs after first layer of PARG (MNBs:PARG).

As presented in Figure.3.11, the TEM image depicts that the morphology of MNBs:PARG was unaffected even after layering and nearly undistinguishable from initial MNBs in Figure. 3.5. Hereafter we will discuss the data in complement to DLS and zeta potential values that will give idea about success of the layering process.

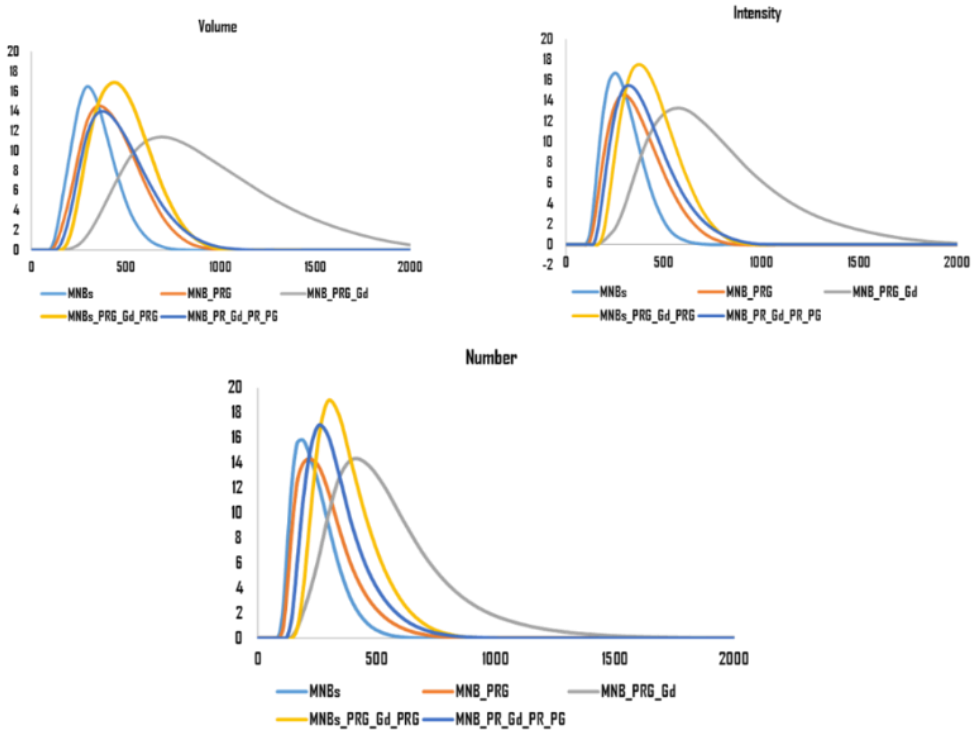

Sample	Number	Intensity	Volume	PDI
MNBs	213±9	267±8	300±17	0.1
MNB:PARG	248±6	322±9	375±18	0.141
MNB:PARG:Gd	466±20	738±76	1332±430	0.235
MNB:PARG:Gd:PARG	340±5	399±10	444±15	0.122

Figure 3.12. Hydrodynamic size values of structure at each stage of layering, explains the trend of structural size growth achieved owing to layering. The values derived from an average of three consequent measurement obtained from DLS peaks, represented in number, intensity and volume percentages respectively.

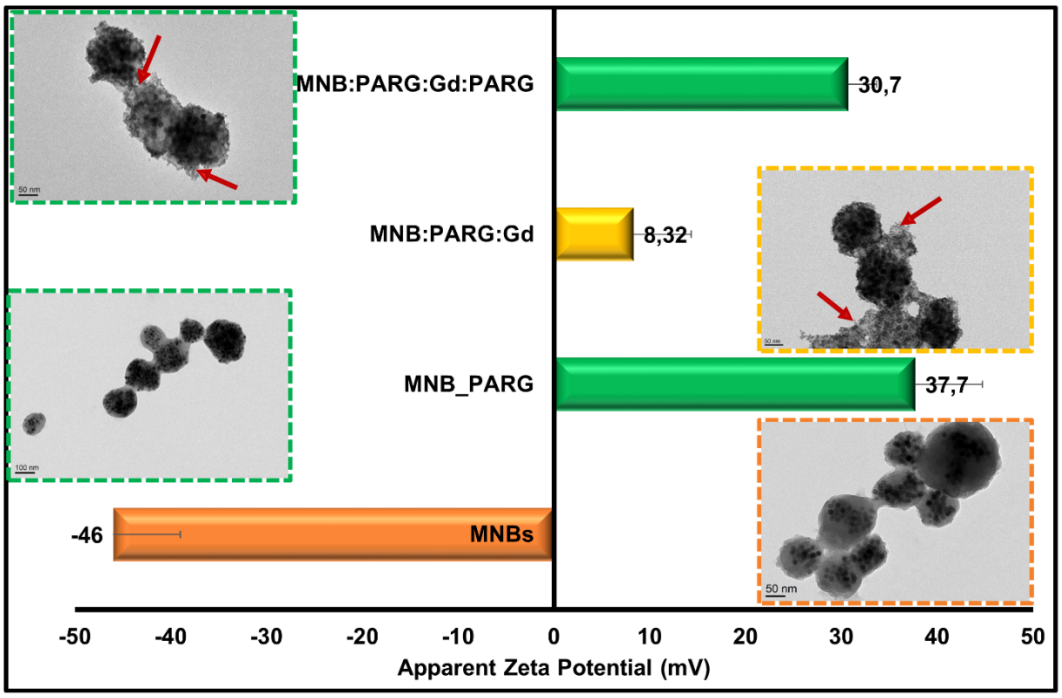

Figure 3. 13. Zeta potential values of structures at each stage of layering. Corresponding values define the trend of charge shift owing to material employed for layering. To offer structural view, respective TEM images were added as insets. Red colored arrows in images intend to highlight inclusion of PAA-$NaGdF_4$ NPs.

As presented in Figure. 3.12, an increase in hydrodynamic size from 213 ±9 nm (Size of MNBs) to 248 ±6 nm, confirms the success of layering; (here PARG thickness of PARG achieved was approximately 35 nm). Please also refer to the table in Figure 3.12 for values. In addition, shift of surface charge from negative (-46 mV of MNBs) to positive value (37.7 mV) that owes to the charge of PARG, also confirms layering; refer to Figure 3.13.

In the next step, the aqueous solution of MNBs:PARG that is now with positive charge was added dropwise into a 8 mL glass vial composed of PAA-$NAGdF_4$ NPs (1 mg/mL in 1 mL of water) of surface negative charge (-13 mV), performed under sonication and subsequently incubated for another 1h under vigorously shaking on orbital shaker of 1250 rpm. Similar to first layering, current incubation promoted gradual interaction of PAA-$NAGdF_4$ NPs to the surface of MNBs:PARG. At the end, the product was collected by a magnet and processed similar to that of first layering and, re-dispersed in 1 mL of water. Here onwards the sample will be termed as “MNBs:PARG:Gd”.

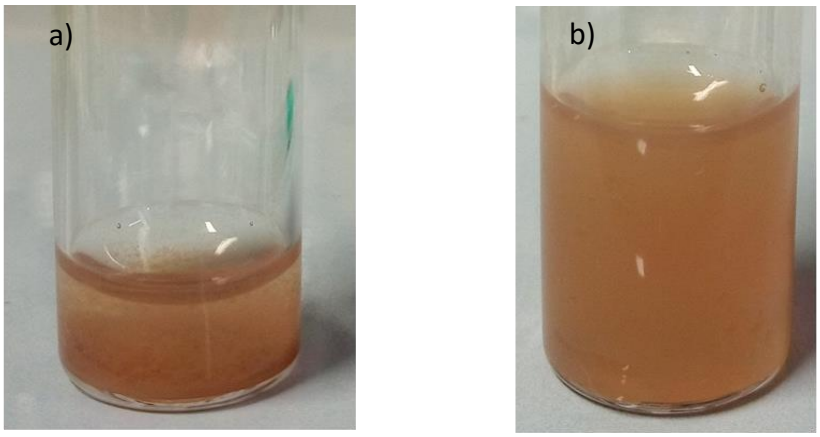

Figure 3.14. Photographs of Magnetic nanobeads, a) after been layered with PARG and gadolinium nanoparticles and b) after re-wrapping with another layer of PARG. The figure differentiate how sample regained the stability after last PARG coating.

As shown in the photograph of Figure 3.14a, the sample at this stage appeared precipitating. According to our hypothesis, gadolinium particles might have interacted enormously, as a result particles lost their stability.

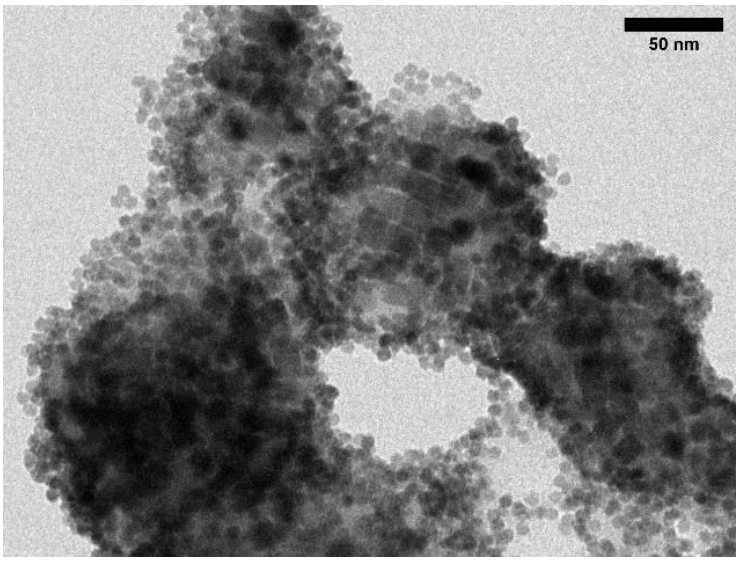

Figure 3. 15. TEM image of magnetic nanobeads layered with an alternative layer of PARG and PAA-$NaGdF_4$ NPs.

Indeed, we have confirmed the said phenomena from TEM imaging and DLS data. As given in Figure 3.15, a large population of particles were spotted hanging out on the surface of MNBs:PARG:Gd. Attributing to this observations, DLS peak corresponding MNBs:PARG:Gd was identified with large hydrodynamic size value of 466±20 nm, that is higher than the value of MNBs:PARG (248±6 nm, refer

to MNBs:PARG:Gd values in table of Figure 3.12). In addition, the zeta value determined by DLS evidenced, the shift of surface charge towards neutral point (8.3 mV) from high positivity (37.7 mV of MNBs:PARG); refer to Figure 3.13. All these explain why the structures were found to lose stability, mainly because, the poor surface charge might have promoted unintentional coalescence of structures. However, fortunately, these structures could regain their stability once after layering with another layer of PARG, the details we will be discussed hereon.

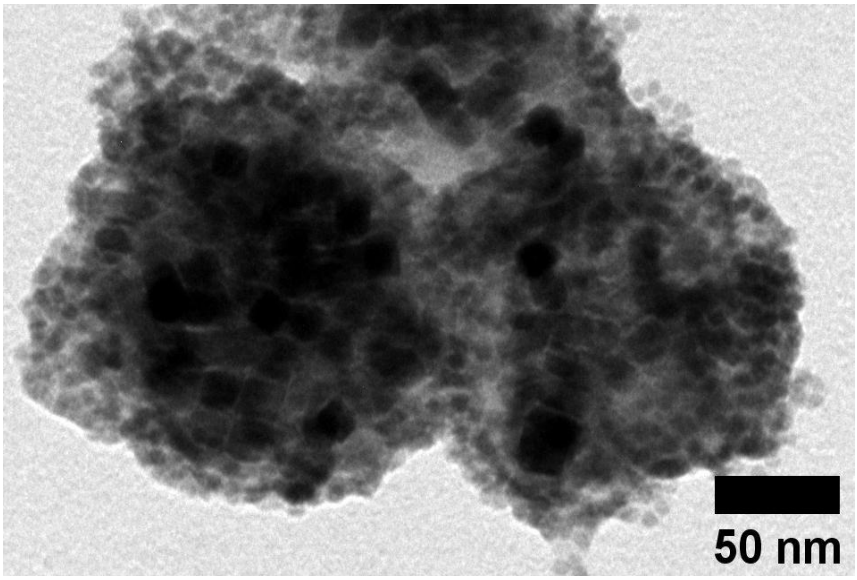

Figure 3.16. TEM images of magnetic nanobeads with three subsequent layers of, PARG, PAA-$NaGdF_4$ NPs and PARG respectively.

Next, the PARG supernatant that we preserved from first layering was re-utilized. The conditions and washing process practiced was exactly similar to that of first layering. We termed this product as "MNBs:PARG:Gd:PARG". Surprisingly, this structures regained their lost macroscopic stability in previous layering as picturized in Figure 3.14b. In fact, the hydrodynamic size was also declined to a lower value of 340±5 nm with narrow PDI value of 0.121, with respect to previous MNBs:PARG:Gd; refer to Figure 3.12. In line, their surface charge was also improved from neutral point (8.32 mV), where it re-shifted towards positive value (38 mV), whose value was similar to that of first PARG layer. In addition, TEM image in Figure 3.16, confirms successful layering, where the surface of MNBs:PARG:Gd:PARG appeared soft and enclosed and moreover no signs of particles leakage on grid were observed.

3.3.4 Magnetic hyperthermia properties

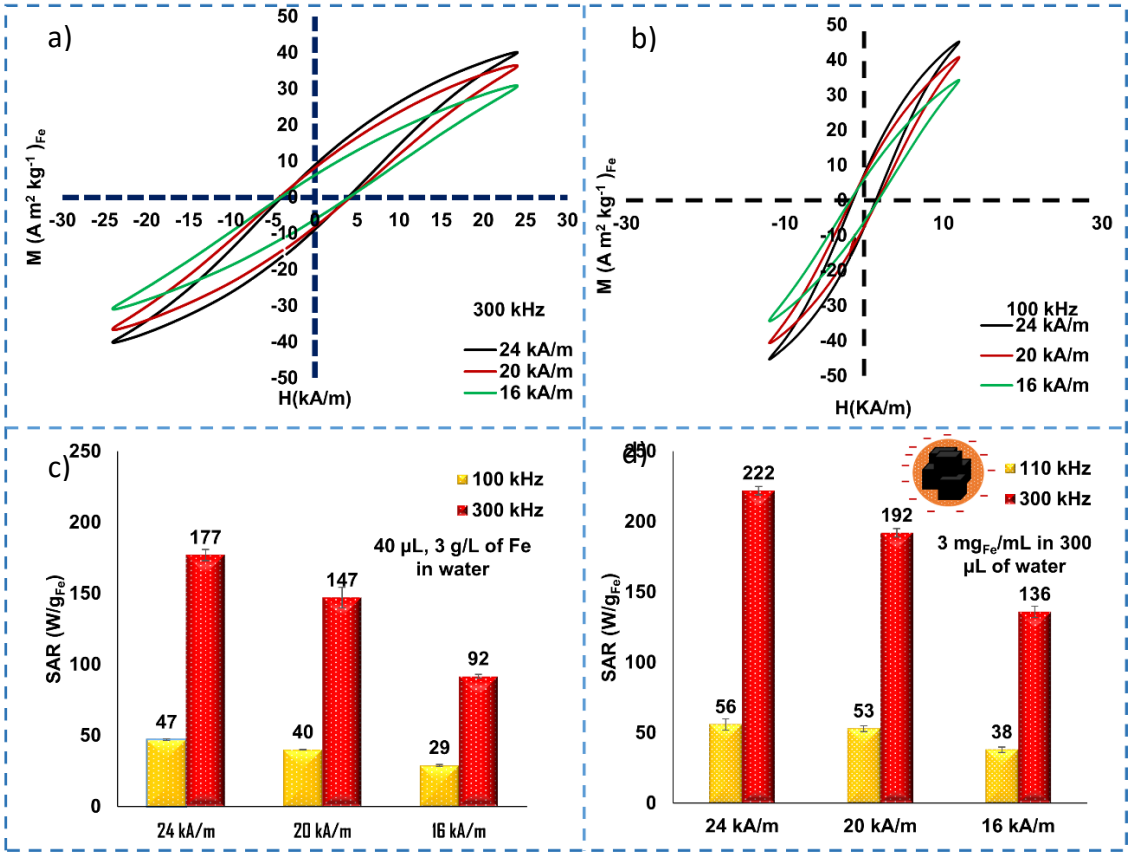

Figure 3.17. Magnetic hyperthermia/heating properties of magnetic nanobeads. a&b) The ac hysteresis loops area of MNBs derived under two distinct frequencies of 300 & 100 kHz and varied field ranges between (16-24 kA/m), measured at a concentration of 3 mg of Fe/mL and in a volume of 40 µL. c) SAR values calculated based on the hysteresis loop area (SAR= A.f). d) Plot elucidating the specific absorption rate values derived from calorimetric measurements, before layering, under two distinct frequencies of 300 & 110 kHz and varied field ranges between (16-24 kA/m), measured at a concentration of 3 mg of Fe/mL.

Prior to layering, the heating ability of aqueous dispersion of MNBs was assessed through two approaches; AC hysteresis and calorimetric measurements. All measurement were performed under two distinct frequencies of 300 & 110 kHz (100 kHz in AC hysteresis) respectively, over field strength that ranges between 16-24 kA/m, in a volume of 40 µL for AC hysteresis and 300 µL for calorimetric, both at a concentration of 3 mg_{Fe}/mL respectively.

As shown in Figure 3.17.a&b, despite the similar magnetization, the hysteresis loop area of MNBs at 300 kHz was obviously wider in comparison to that of 100 kHz loops. With respect to this, SAR values calculated according to SAR= A.*f*, (A represents area of the loop and *f*= frequency),[125] given highest

value of 177±4 W/g at 300 kHz and 24 kA/m, while it is reduced by~ 14 % (146±7.2 W/g) and 48 % (92.0±1.4 W/g) under 20 & 16 kA/m respectively (Figure 3.17.c). However, at 100 kHz, these derivatives were relatively poor and almost independent of fields that appeared to be saturated with a very narrow difference of SAR values (47.0±0.3, 40.0±0.3 and 29.2±0.7 W/g at 24, 20 & 16 kA/m respectively).

In addition, the calorimetric measurements also revealed the same trend of SAR as of AC hysteresis. As reported in Figure 3.17d, they exhibit remarkable SAR of 222±3 W/g at the highest AMF of 300 kHz and 24 kA/m and however this descends with the field strength; upto 14 % (SAR= 192±3 W/g) and 39 %(SAR= 136±4 W/g) at 20 and 16 kA/m respectively. Similar to the observations of SAR in AC hysteresis, the values remain within the range of 38-56 W/g at 110 kHz. Indeed the results what we have obtained are in agreement to similar beads that was published by our group in 2015.[64] Basically, heat losses in magnetic materials was a synergic contribution of two types of relaxation motions; Neel's (flip of internal magnetic moments) and Brownian (physical rotation of the structure).[45,195] Being an assembly of multiple particles, low frequencies may not be sufficient to induce a proper physical flip of MNBs, which consequently reduces the magnetic hysteresis loop area and thus the magnetic hyperthermia abilities.

However, to note, the SAR values obtained at biologically relevant magnetic excitation field strengths; for instance 300 kHz and 16 kA/m, were remarkably appreciable (Figure 3.17d) with respect to that of commercial/spherical iron oxide nanoparticles.[33]

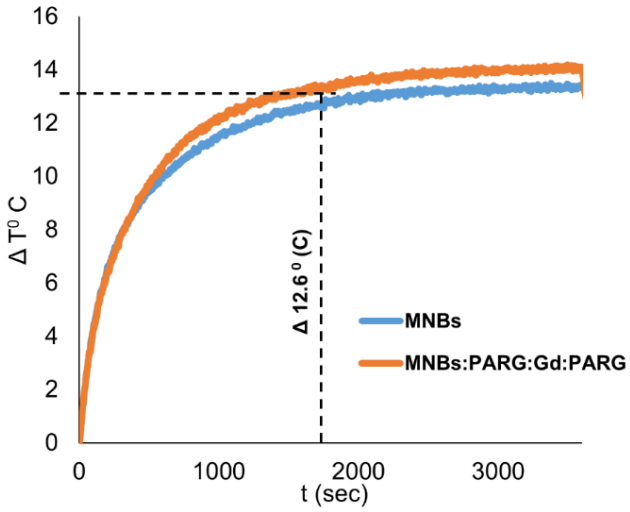

Figure 3. 18. Plots presents the maximum temperature difference MNBs and MNBs:PARG:Gd:PARG could achieve in a period of 1 hour on continues exposition to the AMF of 300 kHz and 16 kA/m, whose H_f factor was below the biological acceptable limit of 5×10^9 A m^{-1} s^{-1}.

In addition to the SAR measurements, the maximum temperature difference (ΔT˚C) that MNBs and MNBs:PARG:Gd:PARG could achieve in a given span of time was recorded as function of time, after their long-term exposition to AMF for 1 hour. For biological assumptions it is important to investigate their performance under biological relevance magnetic excitation fields and frequencies. Therefore, we have kept the magnetic excitation field conditions within this limit whose H*f* factor was less than 5 × 10^9 A $m^{-1}s^{-1}$;[52] that is H= 300 kHz and *f* =16 KA/m. As presented in Figure 3.18, MNBs and MNBs:PARG:Gd:PARG have a comparable heating profile (the narrow 1°C difference could be an experimental error), where both achieved a ΔT˚C of almost 13.93˚C in a span of 1 hour. It is important to highlight that the raise is much pronounced within first 30 min with almost ΔT˚= 12.83 °C and in next 30 min only 1.1 °C of raise and hereby, the sample appeared catching saturation. Importantly, despite of its increased hydrodynamic size (refer to Fig.3.12), attributed to multiple layers, their unaltered heating trend was absolutely remarkable. This could be explained by the fact that, already in the form of 3D cluster, the interparticlular spacing was frozen, thus the resulting Brownian motion was also saturated to certain extent. Hereafter, whatever the relaxation contributes to heat might have been coming from Neel's. Therefore any further increase in size may not have affected the heating behavior as it was explained in intentional aggregation induces AC hysteresis study on similar structures (3D-MNBs) in chapter 1, section 1.3.6. We can claim this to be a key feature for biological application, because we can overcome the negative heating behavior which was happening after internalization to

cells, due to uncontrolled aggregation lead by complex environment. However, we have to confirm the statement with much more additional experiment that will be planned in the future.

3.3.5 Relaxivity profiles

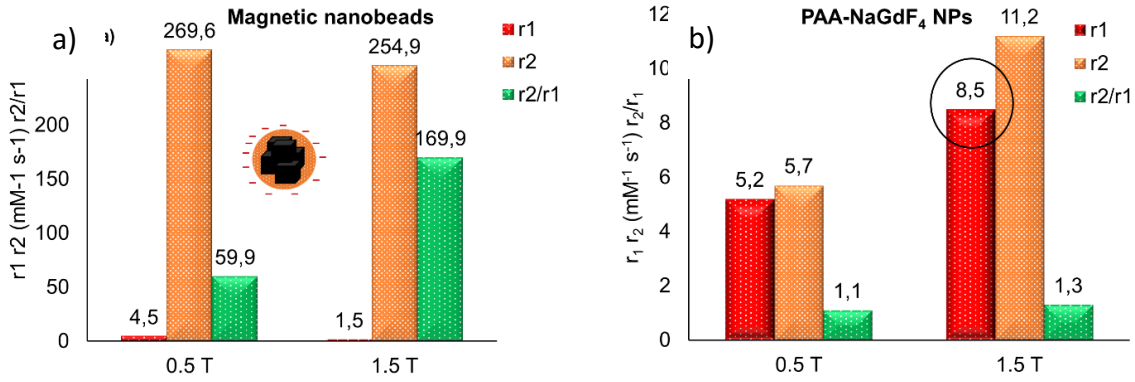

Figure 3.19. Relaxivity profile of magnetic nanostructure before and after layering. a) The chart showing the r_1 and r_2 relaxation rate and corresponding r_2:r_1 ratio of magnetic nanobeads measured under 0.5 & 1.5 T of static magnetic fields, b) Similar results from PAA-NaGdF$_4$ NPs.

Firstly, the relaxivity of MNBs and PAA-NaGdF4 NPs was studied separately before analyzing hybrid structure (MNBs:PARG:Gd:PARG). Measurements were performed on water dispersed samples under two distinct static magnetic fields of 0.5T and 1.5T at 40°C, whose concentration ranges between 0.01 to 1 mM and subsequently recorded relaxation times. The corresponding data was presented as relaxation constants; longitudinal (r_1) and transverse constant (r_2).

As presented in Figure 3.19a, the MNBs exhibited very well pronounced r_2 rates, 269.6 and 254.9 $mM^{-1}.s^{-1}$ under a static field of 0.5T and 1.5T respectively. On the other side, r_1 rates are significantly poor; for instance, at 0.5T they have only 4.5 mM^{-1} s^{-1} and that reduced to 1.5 mM^{-1} s^{-1} by shifting to 1.5T. Because, iron oxide nanocubes in this size range have typical superparamagnetic behavior, eventually the resulted magnetic susceptibility could induce a significant transverse relaxation motion of water proton as reported by many studies.[178] Importantly, at 1.5 T, our MNBs have very high relaxation ratio; r_2:r_1 = 169.9 mM^{-1} s^{-1}, a peculiar sign for being an efficient T_2 agent.[196,197] Normally, in individual forms of IONCs this ratio remains relatively lower than their assemblies, as reported in work of Materia, M. E. *et al.*,[64] hence clusters are advantageous for reducing the signal to noise ratio. The outcome explains the fact that, magnetic moments of each particles in cluster synergistically contributes to create a great magnetic inhomogeneity to shorten transverse magnetic relaxation of water proton.[198]

Secondly, Figure 3.19b explains key T_1 relaxing abilities of PAA-$NaGdF_4$ NPs. These particles have one order of magnitude high r_1 relaxivity constant (r_1= 8.54 mM^{-1} s^{-1}) at 1.5 T than most commercial available gadolinium chelates.[199]. However, its r_1 reduces to 5.12 mM^{-1} s^{-1} under 0.5 T. In fact these values were matching with recent work on $NaGdF_4$ NPs of similar size.[179] Of note, using Gd^{3+} chelates associate to nephron toxicity, which mainly limited their wide application.[200] In our case, the Gd^{3+} ions embedded in the form of inorganic nanoparticles, advantageous for preventing molecular leaking, thus to reduce the toxicity.[201,202] When we derived the relaxation ratios (r_2:r_1), excitingly, our PAA-$NaGdF_4$ exhibited values less than 2 $mM^{-1}s^{-1}$ under both static field conditions; 1.1 and 1.34 mM^{-1} s^{-1} respectively. Its been reported, when ratio remains below 2 mM^{-1} s^{-1} , the material can be considered as an efficient T_1 contrast agent and if it is above 10 mM^{-1} s^{-1}, comes under category of T_2 relaxers. Within this, our intention of employing PAA-$NaGdF_4$ NPs and MNBs as T_1 and T_2 agents has been justified.[196,197]

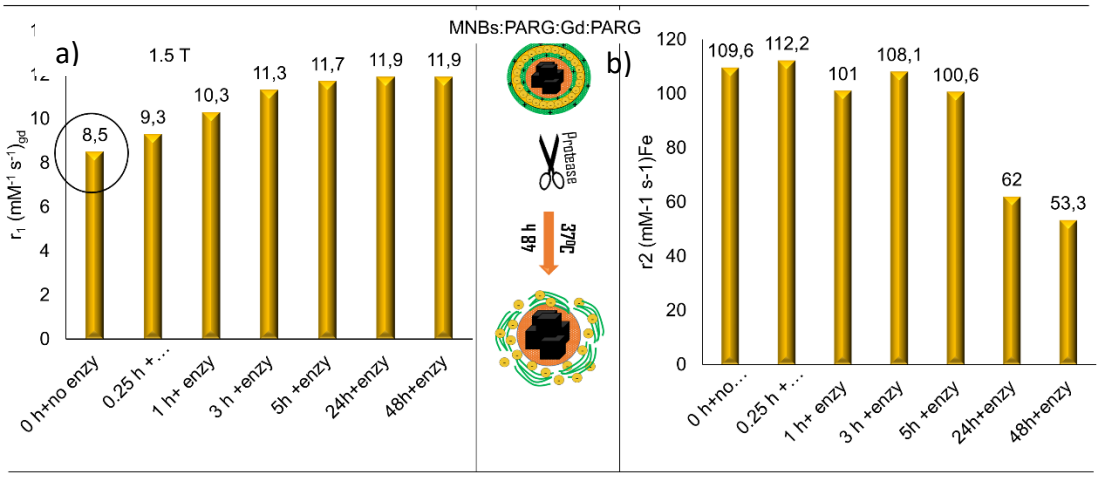

Figure 3.20. a) The longitudinal relaxation (r_1) profile of MNBs:PARG:Gd:PARG plotted based on the gadolinium concentrations. The plot extrapolates the evolution r_1 rates over a period of 48 h, after exposing to the protease enzyme under biological temperature of 37 °C. b) The transverse relaxation rate (r_1) of MNBs:PARG:Gd:PARG plotted based on the iron concentrations. Chart represent the r_2 relaxation rate of hybrid structure, exposed to the protease enzyme incubated at 37 °C as function of the time.

Later, after the LBL process, the relaxivity of MNBs:PARG:Gd:PARG was measured, this time only at 1.5T. It is worty to mention, merging of both modilities into single structure have conceptual contradition for ploting the data.[203] To explain, gadolinum being a paramagntic compound will have neglible impact on T_2 relaxation property of iron. While, on contrary the iron oxide, because of its

superparamagnetic behavior can create magnetic suspetibility even at proximity that may affect T_1 relaxation of gadolinium on surface. However, it is not a right approximation to consider Fe while ploting T_1 relaxation because, the Fe concentration in our system is approximately four times higher than gadolinium; in terms of molar concentration (1.5 mM: 6.3 mM, Gd:Fe ratio). Hence to avoid ambiguity, we have given the data independently; r_1 and r_2 based on Gd and Fe respectively, like it has been done in other studies.[182,204]

Our hybrid structure; MNBs:PARG:Gd:PARG preserves its r_1 rates (Figure 3.20a, point 0h no enzyme) coming from PAA-$NaGdF_4$ NPs (Figure 3.19b), while the r_2 rates of magnetic moiety (i.e. MNBs) almost shrinks by 57 % (109.5 $mM^{-1}s^{-1}$) as given in Figure 3.20b; point 0h no enzyme. If T_1 relaxer remains in close aid to magnetic domain, there is a chance of losing its properties due to magnetic susceptibility created from iron. In our case, the intermediate PARG layer protects Gd^{3+} ion from negative impact of Fe core, thus it saves their initial r_1 values after merging

The PARG used in our layering process have a unique property of degrading in presence of protease enzyme that is rich in tumor microenvironment.[192] Henceforth, we investigated the structural and relaxation changes by exposing our MNBs:PARG:Gd:PARG to protease enzyme incubated for 48h at 37°C. At first glance (Figure 3.20a), we can notice the r_1 rates of structures eventually increased from non-enzymatic condition (8.5 $mM^{-1}s^{-1}$) upto to 24h and reaches saturation value of r_1= 11.9 $mM^{-1}s^{-1}$. While in contrary, the trend in Figure 3.20b explains, the r_2 rates remain constant upto 5h of incubation even with enzyme and that later decreased approximately by half. Evidence in improving r_1 relaxation in response to enzyme was depicted in Figure 3.21, where the relaxation ratios were declined over a period of time from 50 mM^{-1} s^{-1} to 17 mM^{-1} s^{-1}.

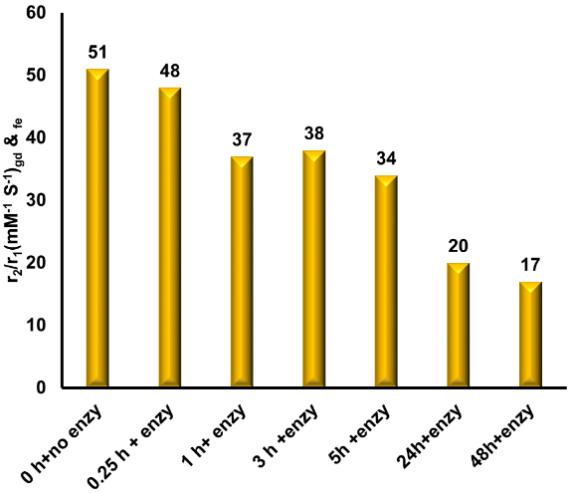

Figure 3.21. Bar chart showing r_2: r_1 relaxation ratios after enzyme exposition. The values derived based on Gd and Fe content.

3.3.6 Tracking morphological changes of MNBs:PARG:Gd:PARG in response to protease

Parallely, we captured morphologies under TEM at respective time points of 0.25 min, 1 h, 3h, 5h, 24h and 48h, while in incubation with protease enzyme at 37°C; given in Figure 3.22.

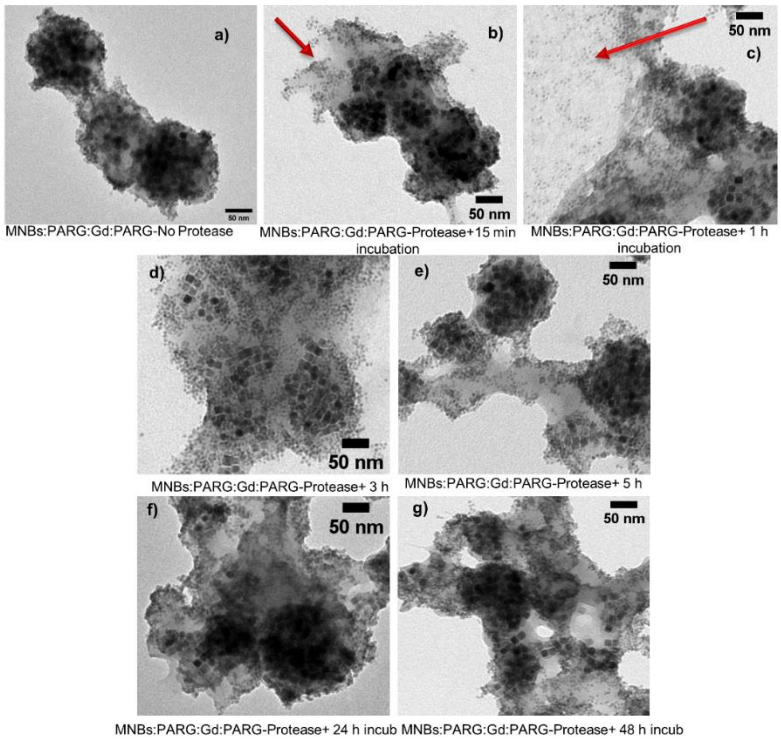

Figure 3. 22. Micrographs of the magnetic nanostructures, imaged before and after exposing to protease enzyme, at various time point of incubation starting form no enzyme to 0.25, 1, 3, 5, 24 and 48 hours of incubation with protease at 37 ˚C.

As we can see in the micrographs with respect to non-enzyme state, (Figure 3.22a), the wall of structure after 15 min on exposing to enzyme appeared rupturing, consequently the PAA-$NaGdF_4$ NPs were leaching (highlighted in red arrows in Figure 3.22b). Interestingly after 1h, the gadolinum particles started distributing freely on the TEM grid. In compliance to our observations, the r_1 relaxation rate at this points; 0.25 and 1h increased because, the Gd^{3+} domain disassembled were gradually re-enwrapping in PARG which was disposed from surface of MNBs in response to enzyme, as a result it retains more water molecules close to the Gd^{3+} domains and this is one of the crucial factor for better T_1 relaxation.[181] On further incubation, PAA-$NaGdF_4$ NPs particles dettached from beads surface appeared re-grouping into large assemblies, that was associated with further improvement of r_1 relaxation and that continued upto 24 h point and then saturated. Besides, these structural changes have'nt affected T_2 response upto 5h, however attributing to enormous groups (Figure 3.22.f&g), which can be considered as partial aggregation, the rates reduced by half as said before.

3.4 Conclusions

In this project, with clear intention of developing multifunctional tool having theranostic properties; MH and MRI imaging (T_1 and T_2 dual imaging abilities), we have prepared magnetic domains named as "magnetic nanobeads (with surface negative charge)" from IONCs of edgelength 14±2 nm (produced at IIT by Dr.Helena) for MH and T_2 relaxation. Secondly, we water transferred the hydrophobic $NaGdF_4$ NPs (produced at IIT by Dr. Emille) using polyacrylic acid (with surface negative charge) as a T_1 relaxation agent for MRI. The morphologies and colloidal stability of both the domains was confirmed under TEM and DLS. Magnetic nanobeads have given efficient heat properties with maximum reachable temperature difference (from baseline) of 13.93˚C in 1h on exposition to the alternative magnetic fields of biological relevance that may be sufficient to induce thermo-toxicity. Relaxation efficiencies of MNBs (r_2:r_1= 169 $mM^{-1}s^{-1}$ for T_2) and PAA-$NaGdF_4$ NPs (r_2:r_1= 1.34 $mM^{-1}s^{-1}$) at 1.5 T were remarkable, which justified our choice for respective properties. Indeed, these results were at least one order magnitude higher than those of most commercial products. Later, we achieved our goal in combining both the domains systematically through electrostatic inspired LBL process where a protease degradable spacer PARG separates domains alternatively (MNBs:PARG:Gd:PARG). Interestingly, despite of increase in size that owes to layering, our hybrid structure preserved temperature raise profile similar to that of initial MNBs. Though the T_2 properties of iron domain were

reduced by half on combination, but still the values are comparible to most commercial available T_2 agents. While on the other side, the T_1 properties of PAA-$NaGdF_4$ NPs were well preserved. In addition, when exposed to protease (rich in tumor environment) under biological temperature, interestingly, the T_1 relaxivity based on Gd^{3+} (for image brightening abilities) improved further over a period of 48 h from 8.5 $mM^{-1}s^{-1}$ to 11.9 $mM^{-1}s^{-1}$. Our hybrid structure with combined magnetic hyperthermia and MRI (dual model T_1 & T_2), responsive to tumorous enzymes were expected to be advantageous to induce thermo-therapy and simultaneously, artifact-free diagnosis, that is not necessary to inject additional materials. In future, we would explore heating and imaging abilities of our hybrid structures in *in vitro* models.

Bibliography

1. Kruis, F. E., Fissan, H. & Peled, A. Synthesis of nanoparticles in the gas phase for electronic, optical and magnetic applications - A review. *Journal of Aerosol Science* (1998). doi:10.1016/S0021-8502(97)10032-5

2. Ambashta, R. D. & Sillanpää, M. Water purification using magnetic assistance: A review. *Journal of Hazardous Materials* (2010). doi:10.1016/j.jhazmat.2010.04.105

3. Surendhiran, D., Sirajunnisa, A. & Tamilselvam, K. Silver–magnetic nanocomposites for water purification. *Environmental Chemistry Letters* (2017). doi:10.1007/s10311-017-0635-1

4. Masunga, N., Mmelesi, O. K., Kefeni, K. K. & Mamba, B. B. Recent advances in copper ferrite nanoparticles and nanocomposites synthesis, magnetic properties and application in water treatment: Review. *Journal of Environmental Chemical Engineering* (2019). doi:10.1016/j.jece.2019.103179

5. Pankhurst, Q. A., Connolly, J., Jones, S. K. & Dobson, J. Applications of magnetic nanoparticles in biomedicine. *Journal of Physics D: Applied Physics* (2003). doi:10.1088/0022-3727/36/13/201

6. Bárcena, C., Sra, A. K. & Gao, J. Applications of magnetic nanoparticles in biomedicine. in *Nanoscale Magnetic Materials and Applications* (2009). doi:10.1007/978-0-387-85600-1_20

7. Akbarzadeh, A., Samiei, M. & Davaran, S. Magnetic nanoparticles: Preparation, physical properties, and applications in biomedicine. *Nanoscale Res. Lett.* (2012). doi:10.1186/1556-276X-7-144

8. Na, H. Bin, Song, I. C. & Hyeon, T. Inorganic nanoparticles for MRI contrast agents. *Adv. Mater.* (2009). doi:10.1002/adma.200802366

9. Sun, C., Lee, J. S. H. & Zhang, M. Magnetic nanoparticles in MR imaging and drug delivery. *Advanced Drug Delivery Reviews* (2008). doi:10.1016/j.addr.2008.03.018

10. Babes, L., Denizot, B., Tanguy, G., Le Jeune, J. J. & Jallet, P. Synthesis of iron oxide nanoparticles used as MRI contrast agents: A parametric study. *J. Colloid Interface Sci.* (1999). doi:10.1006/jcis.1998.6053

11. Fathy, M. M., Fahmy, H. M., Balah, A. M. M., Mohamed, F. F. & Elshemey, W. M. Magnetic nanoparticles-loaded liposomes as a novel treatment agent for iron deficiency anemia: In vivo study. *Life Sci.* (2019). doi:10.1016/j.lfs.2019.116787

12. Shin, T. H., Choi, Y., Kim, S. & Cheon, J. Recent advances in magnetic nanoparticle-based multi-modal imaging. *Chemical Society Reviews* (2015). doi:10.1039/c4cs00345d

13. Ferguson, R. M., Khandhar, A. P. & Krishnan, K. M. Tracer design for magnetic particle imaging (invited). in *Journal of Applied Physics* (2012). doi:10.1063/1.3676053

14. Du, Y., Lai, P. T., Leung, C. H. & Pong, P. W. T. Design of superparamagnetic nanoparticles for magnetic particle imaging (MPI). *International Journal of Molecular Sciences* **14**, 18682–18710 (2013).

15. Saritas, E. U. *et al.* Magnetic particle imaging (MPI) for NMR and MRI researchers. *J. Magn. Reson.* (2013). doi:10.1016/j.jmr.2012.11.029

16. Gao, Y., Liu, Y. & Xu, C. Magnetic nanoparticles for biomedical applications: From diagnosis to treatment to regeneration. in *Engineering in Translational Medicine* (2014). doi:10.1007/978-1-4471-4372-7_21

17. Hubert, V. *et al.* MRI coupled with clinically-applicable iron oxide nanoparticles reveals choroid plexus involvement in a murine model of neuroinflammation. *Sci. Rep.* (2019). doi:10.1038/s41598-019-46566-1

18. Chang, D. *et al.* Biologically targeted magnetic hyperthermia: Potential and limitations. *Frontiers in Pharmacology* (2018). doi:10.3389/fphar.2018.00831

19. Gas, P. Essential facts on the history of hyperthermia and their connections with electromedicine. *Przeglad Elektrotechniczny* (2011).

20. Elming, P. B. *et al.* Hyperthermia: The optimal treatment to overcome radiation resistant hypoxia. *Cancers* (2019). doi:10.3390/cancers11010060

21. Kok, H. P. *et al.* Current state of the art of regional hyperthermia treatment planning: A review. *Radiation Oncology* (2015). doi:10.1186/s13014-015-0503-8

22. Habash, R. W. Y., Bansal, R., Krewski, D. & Alhafid, H. T. Thermal therapy, Part 2: Hyperthermia techniques. *Critical Reviews in Biomedical Engineering* (2006). doi:10.1615/CritRevBiomedEng.v34.i6.30

23. Beik, J. *et al.* Nanotechnology in hyperthermia cancer therapy: From fundamental principles to advanced applications. *Journal of Controlled Release* (2016). doi:10.1016/j.jconrel.2016.05.062

24. Bañobre-López, M., Teijeiro, A. & Rivas, J. Magnetic nanoparticle-based hyperthermia for cancer treatment. *Reports of Practical Oncology and Radiotherapy* **18**, 397–400 (2013).

25. GIUSTINI, A. J. *et al.* MAGNETIC NANOPARTICLE HYPERTHERMIA IN CANCER TREATMENT. *Nano Life* (2010). doi:10.1142/s1793984410000067

26. Kozissnik, B., Bohorquez, A. C., Dobson, J. & Rinaldi, C. Magnetic fluid hyperthermia: Advances, challenges, and opportunity. *International Journal of Hyperthermia* (2013). doi:10.3109/02656736.2013.837200

27. GILCHRIST, R. K. *et al.* Selective inductive heating of lymph nodes. *Ann. Surg.* (1957). doi:10.1097/00000658-195710000-00007

28. Mahmoudi, K., Bouras, A., Bozec, D., Ivkov, R. & Hadjipanayis, C. Magnetic hyperthermia therapy for the treatment of glioblastoma: a review of the therapy's history, efficacy and application in humans. *International Journal of Hyperthermia* (2018). doi:10.1080/02656736.2018.1430867

29. Abenojar, E. C., Wickramasinghe, S., Bas-Concepcion, J. & Samia, A. C. S. Structural effects on the magnetic hyperthermia properties of iron oxide nanoparticles. *Prog. Nat. Sci. Mater. Int.* (2016). doi:10.1016/j.pnsc.2016.09.004

30. Maier-Hauff, K. *et al.* Efficacy and safety of intratumoral thermotherapy using magnetic iron-oxide nanoparticles combined with external beam radiotherapy on patients with recurrent glioblastoma multiforme. *J. Neurooncol.* (2011). doi:10.1007/s11060-010-0389-0

31. Silva, A. C. *et al.* Application of hyperthermia induced by superparamagnetic iron oxide nanoparticles in glioma treatment. *International journal of nanomedicine* (2011). doi:10.2147/IJN.S14737

32. Lee, J. H. *et al.* Exchange-coupled magnetic nanoparticles for efficient heat induction. *Nat. Nanotechnol.* (2011). doi:10.1038/nnano.2011.95

33. Bae, K. H. *et al.* Chitosan oligosaccharide-stabilized ferrimagnetic iron oxide nanocubes for magnetically modulated cancer hyperthermia. *ACS Nano* (2012). doi:10.1021/nn301046w

34. Materia, M. E. *et al.* Multifunctional Magnetic and Upconverting Nanobeads as Dual Modal Imaging Tools. *Bioconjug. Chem.* **28**, 2707–2714 (2017).

35. Ortega, D. & Pankhurst, Q. A. Magnetic hyperthermia. in (2012). doi:10.1039/9781849734844-00060

36. Gupta, A. K. & Gupta, M. Synthesis and surface engineering of iron oxide nanoparticles for biomedical applications. *Biomaterials* (2005). doi:10.1016/j.biomaterials.2004.10.012

37. Krishnan, K. M. Biomedical nanomagnetics: A spin through possibilities in imaging, diagnostics, and therapy. *IEEE Trans. Magn.* (2010). doi:10.1109/TMAG.2010.2046907

38. Dunlop, D. J. & West, G. F. An experimental evaluation of single domain theories. *Reviews of Geophysics* (1969). doi:10.1029/RG007i004p00709

39. Carrey, J., Mehdaoui, B. & Respaud, M. Simple models for dynamic hysteresis loop calculations of magnetic single-domain nanoparticles: Application to magnetic hyperthermia optimization. *J. Appl. Phys.* (2011). doi:10.1063/1.3551582

40. Chuev, M. A. & Hesse, J. Nanomagnetism: Extension of the Stoner-Wohlfarth model within Néel's ideas and useful plots. *J. Phys. Condens. Matter* (2007). doi:10.1088/0953-8984/19/50/506201

41. Kok Titz, R., Weitschies, W., Trahms, L. & Semmler, W. Investigation of Brownian and NeH el

relaxation in magnetic #uids. *J. Magn. Magn. Mater.* (1999).

42. Hervault, A. & Thanh, N. T. K. Magnetic nanoparticle-based therapeutic agents for thermo-chemotherapy treatment of cancer. *Nanoscale* (2014). doi:10.1039/c4nr03482a

43. Reeves, D. B. & Weaver, J. B. Approaches for modeling magnetic nanoparticle dynamics. *Crit. Rev. Biomed. Eng.* (2014). doi:10.1615/CritRevBiomedEng.2014010845

44. Hergt, R. & Dutz, S. Magnetic particle hyperthermia-biophysical limitations of a visionary tumour therapy. *J. Magn. Magn. Mater.* (2007). doi:10.1016/j.jmmm.2006.10.1156

45. Rosensweig, R. E. Heating magnetic fluid with alternating magnetic field. *J. Magn. Magn. Mater.* (2002). doi:10.1016/S0304-8853(02)00706-0

46. Lacroix, L. M. *et al.* Magnetic hyperthermia in single-domain monodisperse FeCo nanoparticles: Evidences for Stoner-Wohlfarth behavior and large losses. *J. Appl. Phys.* (2009). doi:10.1063/1.3068195

47. Lemal, P., Geers, C., Rothen-Rutishauser, B., Lattuada, M. & Petri-Fink, A. Measuring the heating power of magnetic nanoparticles: An overview of currently used methods. in *Materials Today: Proceedings* (2017). doi:10.1016/j.matpr.2017.09.175

48. Andreu, I. & Natividad, E. Accuracy of available methods for quantifying the heat power generation of nanoparticles for magnetic hyperthermia. *International Journal of Hyperthermia* (2013). doi:10.3109/02656736.2013.826825

49. Wildeboer, R. R., Southern, P. & Pankhurst, Q. A. On the reliable measurement of specific absorption rates and intrinsic loss parameters in magnetic hyperthermia materials. *J. Phys. D. Appl. Phys.* (2014). doi:10.1088/0022-3727/47/49/495003

50. Jordan, A. Hyperthermia classic commentary: 'Inductive heating of ferrimagnetic particles and magnetic fluids: Physical evaluation of their potential for hyperthermia' by Andreas Jordan et al., International Journal of Hyperthermia, 1993;9:5168. *Int. J. Hyperth.* (2009). doi:10.3109/02656730903183445

51. Atkinson, W. J., Brezovich, I. A. & Chakraborty, D. P. Usable Frequencies in Hyperthermia with Thermal Seeds. *IEEE Trans. Biomed. Eng.* (1984). doi:10.1109/TBME.1984.325372

52. Hergt, R., Dutz, S., Müller, R. & Zeisberger, M. Magnetic particle hyperthermia: Nanoparticle magnetism and materials development for cancer therapy. *J. Phys. Condens. Matter* (2006). doi:10.1088/0953-8984/18/38/S26

53. Mamiya, H. Recent advances in understanding magnetic nanoparticles in ac magnetic fields and optimal design for targeted hyperthermia. *J. Nanomater.* (2013). doi:10.1155/2013/752973

54. Guardia, P. *et al.* Water-soluble iron oxide nanocubes with high values of specific absorption rate for cancer cell hyperthermia treatment. *ACS Nano* (2012). doi:10.1021/nn2048137

55. Kolosnjaj-Tabi, J. *et al.* Heat-generating iron oxide nanocubes: Subtle 'destructurators' of the tumoral microenvironment. *ACS Nano* (2014). doi:10.1021/nn405356r

56. Noh, S. H. *et al.* Nanoscale magnetism control via surface and exchange anisotropy for optimized ferrimagnetic hysteresis. *Nano Lett.* (2012). doi:10.1021/nl301499u

57. Espinosa, A. *et al.* Magnetic (Hyper)Thermia or Photothermia? Progressive Comparison of Iron Oxide and Gold Nanoparticles Heating in Water, in Cells, and In Vivo. *Adv. Funct. Mater.* (2018). doi:10.1002/adfm.201803660

58. Cabrera, D. *et al.* Dynamical Magnetic Response of Iron Oxide Nanoparticles Inside Live Cells. *ACS Nano* acsnano.7b08995 (2018). doi:10.1021/acsnano.7b08995

59. Plan Sangnier, A. *et al.* Targeted thermal therapy with genetically engineered magnetite magnetosomes@RGD: Photothermia is far more efficient than magnetic hyperthermia. *J. Control. Release* (2018). doi:10.1016/j.jconrel.2018.04.036

60. Martinez-Boubeta, C. *et al.* Adjustable hyperthermia response of self-assembled ferromagnetic Fe-MgO core-shell nanoparticles by tuning dipole-dipole interactions. *Adv. Funct. Mater.* (2012). doi:10.1002/adfm.201200307

61. Martinez-Boubeta, C. *et al.* Learning from nature to improve the heat generation of iron-oxide nanoparticles for magnetic hyperthermia applications. *Sci. Rep.* (2013). doi:10.1038/srep01652

62. Coral, D. F. *et al.* Effect of Nanoclustering and Dipolar Interactions in Heat Generation for Magnetic Hyperthermia. *Langmuir* **32**, 1201–1213 (2016).

63. Salas, G. *et al.* Modulation of magnetic heating via dipolar magnetic interactions in monodisperse and crystalline iron oxide nanoparticles. *J. Phys. Chem. C* (2014). doi:10.1021/jp5041234

64. Materia, M. E. *et al.* Mesoscale assemblies of iron oxide nanocubes as heat mediators and image contrast agents. *Langmuir* (2015). doi:10.1021/la503930s

65. Guibert, C., Dupuis, V., Peyre, V. & Fresnais, J. Hyperthermia of Magnetic Nanoparticles: Experimental Study of the Role of Aggregation. *J. Phys. Chem. C* (2015). doi:10.1021/acs.jpcc.5b07796

66. Nakata, K., Hu, Y., Uzun, O., Bakr, O. & Stellacci, F. Chains of superparamagnetic nanoparticles. *Adv. Mater.* (2008). doi:10.1002/adma.200800022

67. Fu, R., Yan, Y., Roberts, C., Liu, Z. & Chen, Y. The role of dipole interactions in hyperthermia heating colloidal clusters of densely-packed superparamagnetic nanoparticles. *Sci. Rep.* **8**, 4704 (2018).

68. Serantes, D. *et al.* Multiplying magnetic hyperthermia response by nanoparticle assembling. *J. Phys. Chem. C* (2014). doi:10.1021/jp410717m

69. Saville, S. L. *et al.* The formation of linear aggregates in magnetic hyperthermia: Implications on specific absorption rate and magnetic anisotropy. *J. Colloid Interface Sci.* (2014). doi:10.1016/j.jcis.2014.03.007

70. Mehdaoui, B. *et al.* Increase of magnetic hyperthermia efficiency due to dipolar interactions in low-anisotropy magnetic nanoparticles: Theoretical and experimental results. *Phys. Rev. B - Condens. Matter Mater. Phys.* (2013). doi:10.1103/PhysRevB.87.174419

71. Alphandéry, E. *et al.* Heat production by bacterial magnetosomes exposed to an oscillating magnetic field. *J. Phys. Chem. C* (2011). doi:10.1021/jp104580t

72. Alphandéry, E., Chebbi, I., Guyot, F. & Durand-Dubief, M. Use of bacterial magnetosomes in the magnetic hyperthermia treatment of tumours: A review. *International Journal of Hyperthermia* (2013). doi:10.3109/02656736.2013.821527

73. Martinez-Boubeta, C. *et al.* Learning from nature to improve the heat generation of iron-oxide nanoparticles for magnetic hyperthermia applications. *Sci. Rep.* (2013). doi:10.1038/srep01652

74. Fu, R., Yan, Y. Y. & Roberts, C. Study of the effect of dipole interactions on hyperthermia heating

the cluster composed of superparamagnetic nanoparticles. *AIP Adv.* (2015). doi:10.1063/1.4939514

75. Corr, S. A. *et al.* Linear assemblies of magnetic nanoparticles as MRI contrast agents. *J. Am. Chem. Soc.* (2008). doi:10.1021/ja710172z

76. Bukharov, A. A., Ovchinnikov, A. S., Baranov, N. V. & Inoue, K. Magnetic hysteresis and domain wall dynamics in single chain magnets with antiferromagnetic interchain coupling. *J. Phys. Condens. Matter* (2010). doi:10.1088/0953-8984/22/43/436003

77. Andreu, I., Natividad, E., Solozábal, L. & Roubeau, O. Nano-objects for addressing the control of nanoparticle arrangement and performance in magnetic hyperthermia. *ACS Nano* (2015). doi:10.1021/nn505781f

78. Calero-Diaz Del Castillo, V. L. & Rinaldi, C. Effect of sample concentration on the determination of the anisotropy constant of magnetic nanoparticles. *IEEE Trans. Magn.* (2010). doi:10.1109/TMAG.2009.2032240

79. Varón, M. *et al.* Dipolar magnetism in ordered and disordered low-dimensional nanoparticle assemblies. *Sci. Rep.* (2013). doi:10.1038/srep01234

80. Myrovali, E. *et al.* Arrangement at the nanoscale: Effect on magnetic particle hyperthermia. *Sci. Rep.* (2016). doi:10.1038/srep37934

81. Lee, Y., Lee, H., Messersmith, P. B. & Park, T. G. A bioinspired polymeric template for 1D assembly of metallic nanoparticles, semiconductor quantum dots, and magnetic nanoparticles. *Macromol. Rapid Commun.* **31**, 2109–2114 (2010).

82. Serantes, D. *et al.* Multiplying magnetic hyperthermia response by nanoparticle assembling. *J. Phys. Chem. C* (2014). doi:10.1021/jp410717m

83. Materia, M. E. *et al.* Mesoscale assemblies of iron oxide nanocubes as heat mediators and image contrast agents. *Langmuir* **31**, 808–816 (2015).

84. Ovejero, J. G. *et al.* Effects of inter- and intra-aggregate magnetic dipolar interactions on the magnetic heating efficiency of iron oxide nanoparticles. *Phys. Chem. Chem. Phys.* (2016). doi:10.1039/c6cp00468g

85. Andreu, I., Natividad, E., Solozábal, L. & Roubeau, O. Nano-objects for addressing the control of nanoparticle arrangement and performance in magnetic hyperthermia. *ACS Nano* (2015). doi:10.1021/nn505781f

86. Niculaes, D. *et al.* Asymmetric Assembling of Iron Oxide Nanocubes for Improving Magnetic Hyperthermia Performance. *ACS Nano* (2017). doi:10.1021/acsnano.7b05182

87. Lombardo, D., Kiselev, M. A., Magazù, S. & Calandra, P. Amphiphiles self-assembly: Basic concepts and future perspectives of supramolecular approaches. *Advances in Condensed Matter Physics* (2015). doi:10.1155/2015/151683

88. Niculaes, D. *et al.* Asymmetric Assembling of Iron Oxide Nanocubes for Improving Magnetic Hyperthermia Performance. *ACS Nano* (2017). doi:10.1021/acsnano.7b05182

89. Di Corato, R. *et al.* Magnetic-fluorescent colloidal nanobeads: Preparation and exploitation in cell separation experiments. *Macromol. Biosci.* (2009). doi:10.1002/mabi.200900154

90. Albarqi, H. A. *et al.* Biocompatible Nanoclusters with High Heating Efficiency for Systemically Delivered Magnetic Hyperthermia. *ACS Nano* (2019). doi:10.1021/acsnano.8b06542

91. Thomas, C. R. *et al.* Noninvasive remote-controlled release of drug molecules in vitro using magnetic actuation of mechanized nanoparticles. *J. Am. Chem. Soc.* (2010). doi:10.1021/ja1022267

92. Ortgies, D. H. *et al.* Optomagnetic Nanoplatforms for In Situ Controlled Hyperthermia. *Adv. Funct. Mater.* (2018). doi:10.1002/adfm.201704434

93. Acharya, S., Hill, J. P. & Ariga, K. Soft langmuir-blodgett technique for hard nanomaterials. *Advanced Materials* (2009). doi:10.1002/adma.200802648

94. Pauly, M. *et al.* Size dependent dipolar interactions in iron oxide nanoparticle monolayer and multilayer Langmuir-Blodgett films. *J. Mater. Chem.* (2012). doi:10.1039/c2jm15797g

95. Bellido, E., Domingo, N., Ojea-Jiménez, I. & Ruiz-Molina, D. Structuration and integration of magnetic nanoparticles on surfaces and devices. *Small* (2012). doi:10.1002/smll.201101456

96. Ahniyaz, A., Sakamoto, Y. & Bergstrom, L. Magnetic field-induced assembly of oriented superlattices from maghemite nanocubes. *Proc. Natl. Acad. Sci.* (2007). doi:10.1073/pnas.0704210104

97. Toulemon, D. *et al.* Enhanced Collective Magnetic Properties in 2D Monolayers of Iron Oxide Nanoparticles Favored by Local Order and Local 1D Shape Anisotropy. *Langmuir* (2016). doi:10.1021/acs.langmuir.5b04145

98. Pichon, B. P. *et al.* 2D assembling of magnetic iron oxide nanoparticles promoted by SAMs used as well-addressed surfaces. *J. Phys. Chem. C* (2010). doi:10.1021/jp101872u

99. Singamaneni, S., Bliznyuk, V. N., Binek, C. & Tsymbal, E. Y. Magnetic nanoparticles: Recent advances in synthesis, self-assembly and applications. *J. Mater. Chem.* (2011). doi:10.1039/c1jm11845e

100. Srivastava, S. & Kotov, N. A. Nanoparticle assembly for 1D and 2D ordered structures. *Soft Matter* (2009). doi:10.1039/b812115j

101. Zhang, J., Liu, Y., Ke, Y. & Yan, H. Periodic square-like gold nanoparticle arrays templated by self-assembled 2D DNA nanogrids on a surface. *Nano Lett.* (2006). doi:10.1021/nl052210l

102. Andreu, I., Natividad, E., Solozábal, L. & Roubeau, O. Nano-objects for addressing the control of nanoparticle arrangement and performance in magnetic hyperthermia. *ACS Nano* **9**, 1408–1419 (2015).

103. Guardia, P. *et al.* One pot synthesis of monodisperse water soluble iron oxide nanocrystals with high values of the specific absorption rate. *J. Mater. Chem. B* **2**, 4426 (2014).

104. Liotta, L. A. & Kohn, E. C. The microenvironment of the tumour - Host interface. *Nature* (2001). doi:10.1038/35077241

105. Kaur, G. Strategies for Large-scale Production of Polyhydroxyalkanoates. *Chem. Biochem. Eng. Q.* (2015). doi:10.15255/CABEQ.2014.2255

106. Rai, R., Keshavarz, T., Roether, J. A., Boccaccini, A. R. & Roy, I. Medium chain length polyhydroxyalkanoates, promising new biomedical materials for the future. *Mater. Sci. Eng. R Reports* (2011). doi:10.1016/j.mser.2010.11.002

107. Alejandra, R. C., Margarita, C. M. & María Soledad, M. C. Enzymatic degradation of poly(3-hydroxybutyrate) by a commercial lipase. *Polym. Degrad. Stab.* (2012).

doi:10.1016/j.polymdegradstab.2012.07.042

108. Kaihara, S. *et al.* Enzymatic transformation of bacterial polyhydroxyalkanoates into repolymerizable oligomers directed towards chemical recycling. *Macromol. Biosci.* (2005). doi:10.1002/mabi.200500030

109. Chen, G. Q. & Wu, Q. The application of polyhydroxyalkanoates as tissue engineering materials. *Biomaterials* (2005). doi:10.1016/j.biomaterials.2005.04.036

110. Bagdadi, A. V. *et al.* Poly(3-hydroxyoctanoate), a promising new material for cardiac tissue engineering. *J. Tissue Eng. Regen. Med.* (2018). doi:10.1002/term.2318

111. Lukasiewicz, B. *et al.* Binary polyhydroxyalkanoate systems for soft tissue engineering. *Acta Biomater.* (2018). doi:10.1016/j.actbio.2018.02.027

112. Hazer, B. Amphiphilic poly(3-hydroxy alkanoate)s: Potential candidates for medical applications. *Int. J. Polym. Sci.* **2010**, (2010).

113. Pouton, C. W. & Akhtar, S. Biosynthetic polyhydroxyalkanoates and their potential in drug delivery. *Advanced Drug Delivery Reviews* (1996). doi:10.1016/0169-409X(95)00092-L

114. Francis, L. *et al.* Controlled delivery of gentamicin using poly(3-hydroxybutyrate) microspheres. *Int. J. Mol. Sci.* (2011). doi:10.3390/ijms12074294

115. Manuscript, A. Europe PMC Funders Group Poly (hydroxy alkanoate) s in Medical Applications. **29**, 287–297 (2017).

116. Li, Z. & Loh, X. J. Water soluble polyhydroxyalkanoates: Future materials for therapeutic applications. *Chem. Soc. Rev.* **44**, 2865–2879 (2015).

117. Akaraonye, E. *et al.* P(3HB) Based Magnetic Nanocomposites: Smart Materials for Bone Tissue Engineering. *J. Nanomater.* (2016). doi:10.1155/2016/3897592

118. Rai, R. *et al.* Highly elastomeric poly(3-hydroxyoctanoate) based natural polymer composite for enhanced keratinocyte regeneration. *Int. J. Polym. Mater. Polym. Biomater.* (2017). doi:10.1080/00914037.2016.1217530

119. Amandeep Girdhar, Mayuri Bhatia, Sunil Nagpal, A. K. and A. T. Process Parameters for Influencing Polyhydroxyalkanoate Producing Bacterial Factories: An Overview. *J. Pet. Environ. Biotechnol.* (2013). doi:10.4172/2157-7463.100015

120. Di Corato, R. *et al.* Magnetic-fluorescent colloidal nanobeads: Preparation and exploitation in cell separation experiments. *Macromol. Biosci.* (2009). doi:10.1002/mabi.200900154

121. Bigall, N. C. *et al.* Colloidal ordered assemblies in a polymer shell - A novel type of magnetic nanobeads for theranostic applications. *Chem. Mater.* (2013). doi:10.1021/cm3036746

122. Niculaes, D. *et al.* Asymmetric Assembling of Iron Oxide Nanocubes for Improving Magnetic Hyperthermia Performance. *ACS Nano* **11**, 12121–12133 (2017).

123. Fu, R., Yan, Y., Roberts, C., Liu, Z. & Chen, Y. The role of dipole interactions in hyperthermia heating colloidal clusters of densely-packed superparamagnetic nanoparticles. *Sci. Rep.* (2018). doi:10.1038/s41598-018-23225-5

124. Basnett, P. *et al.* Biosynthesis and characterization of a novel, biocompatible medium chain length polyhydroxyalkanoate by Pseudomonas mendocina CH50 using coconut oil as the carbon source. *J. Mater. Sci. Mater. Med.* **29**, 179 (2018).

125. Avugadda, S. K. *et al.* Esterase Cleavable 2D Assemblies of Magnetic Iron Oxide Nanocubes: Exploiting Enzymatic Polymer Disassembling to Improve Magnetic Hyperthermia Heat Losses. *Chem. Mater.* (2019). doi:10.1021/acs.chemmater.9b00728

126. Gomes, J., Grunau, A., Lawrence, A. K., Eberl, L. & Gademann, K. Bioinspired, releasable quorum sensing modulators. *Chem. Commun.* (2013). doi:10.1039/c2cc37287h

127. Gillich, T. *et al.* PEG-stabilized core-shell nanoparticles: Impact of linear versus dendritic polymer shell architecture on colloidal properties and the reversibility of temperature-induced aggregation. *ACS Nano* (2013). doi:10.1021/nn304045q

128. Kremer, J. R., Mastronarde, D. N. & McIntosh, J. R. Computer visualization of three-dimensional image data using IMOD. *J. Struct. Biol.* (1996). doi:10.1006/jsbi.1996.0013

129. Spirou, S., Basini, M., Lascialfari, A., Sangregorio, C. & Innocenti, C. Magnetic Hyperthermia and

Radiation Therapy: Radiobiological Principles and Current Practice †. *Nanomaterials* **8**, 401 (2018).

130. Connord, V., Mehdaoui, B., Tan, R. P., Carrey, J. & Respaud, M. An air-cooled Litz wire coil for measuring the high frequency hysteresis loops of magnetic samples - A useful setup for magnetic hyperthermia applications. *Rev. Sci. Instrum.* (2014). doi:10.1063/1.4895656

131. Mehdaoui, B. *et al.* Influence of a transverse static magnetic field on the magnetic hyperthermia properties and high-frequency hysteresis loops of ferromagnetic FeCo nanoparticles. *Appl. Phys. Lett.* (2012). doi:10.1063/1.3681361

132. Wetterskog, E., Tai, C. W., Grins, J., Bergström, L. & Salazar-Alvarez, G. Anomalous magnetic properties of nanoparticles arising from defect structures: Topotaxial oxidation of Fe1- xO|Fe 3-δO4 core|shell nanocubes to single-phase particles. *ACS Nano* (2013). doi:10.1021/nn402487q

133. Walter, A. *et al.* Mastering the shape and composition of dendronized iron oxide nanoparticles to tailor magnetic resonance imaging and hyperthermia. *Chem. Mater.* (2014). doi:10.1021/cm5019025

134. Materia, M. E. *et al.* Mesoscale assemblies of iron oxide nanocubes as heat mediators and image contrast agents. *Langmuir* (2015). doi:10.1021/la503930s

135. Cho, M. *et al.* Assembly of Iron Oxide Nanocubes for Enhanced Cancer Hyperthermia and Magnetic Resonance Imaging. *Nanomaterials* **7**, 72 (2017).

136. Raza, Z. A., Riaz, S. & Banat, I. M. Polyhydroxyalkanoates: Properties and chemical modification approaches for their functionalization. *Biotechnol. Prog.* **34**, 29–41 (2018).

137. Zhang, N. *et al.* From 1D Polymers to 2D Polymers: Preparation of Free-Standing Single-Monomer-Thick Two-Dimensional Conjugated Polymers in Water. *ACS Nano* (2017). doi:10.1021/acsnano.7b03109

138. Ovejero, J. G. *et al.* Effects of inter- and intra-aggregate magnetic dipolar interactions on the magnetic heating efficiency of iron oxide nanoparticles. *Phys. Chem. Chem. Phys.* **18**, 10954–10963 (2016).

139. Di Corato, R. *et al.* Magnetic hyperthermia efficiency in the cellular environment fordifferent nanoparticle designs. *Biomaterials* **35**, 6400–6411 (2014).

140. Soukup, D., Moise, S., Céspedes, E., Dobson, J. & Telling, N. D. In situ measurement of magnetization relaxation of internalized nanoparticles in live cells. *ACS Nano* **9**, 231–240 (2015).

141. Therapy, F. C., Flandrin, B. & Anbiophy-fre, L. Chains of Magnetosomes Extracted from AMB-1 Magnetotactic Bacteria for Application in Alternative Magnetic. 6279–6296 (2011).

142. Lima, E. *et al.* Heat generation in agglomerated ferrite nanoparticles in an alternating magnetic field. *J. Phys. D. Appl. Phys.* **46**, (2013).

143. Dong, H., Pang, L., Cong, H., Shen, Y. & Yu, B. Application and design of esterase-responsive nanoparticles for cancer therapy. *Drug Deliv.* **26**, 416–432 (2019).

144. McGoldrick, C. A. *et al.* Identification of oxidized protein hydrolase as a potential prodrug target in prostate cancer. *BMC Cancer* (2014). doi:10.1186/1471-2407-14-77

145. Shubayev, V. I., Pisanic, T. R. & Jin, S. Magnetic nanoparticles for theragnostics. *Advanced Drug Delivery Reviews* (2009). doi:10.1016/j.addr.2009.03.007

146. Panagiotopoulos, N. *et al.* Magnetic particle imaging: Current developments and future directions. *Int. J. Nanomedicine* (2015). doi:10.2147/IJN.S70488

147. Cao, Y., Xu, L., Kuang, Y., Xiong, D. & Pei, R. Gadolinium-based nanoscale MRI contrast agents for tumor imaging. *Journal of Materials Chemistry B* (2017). doi:10.1039/c7tb00382j

148. Grover, V. P. B. *et al.* Magnetic Resonance Imaging: Principles and Techniques: Lessons for Clinicians. *Journal of Clinical and Experimental Hepatology* (2015). doi:10.1016/j.jceh.2015.08.001

149. Mori, S. Diffusion magnetic resonance imaging: Its principle and applications. *Anat. Rec.* (1999). doi:10.1002/(SICI)1097-0185(19990615)257:3<102::AID-AR7>3.0.CO;2-6

150. Nitz, W. R., Balzer, T., Grosu, D. S. & Allkemper, T. Principles of magnetic resonance. in *Clinical MR Imaging (Third Edition): A Practical Approach* (2010). doi:10.1007/978-3-540-74504-4_1

151. Arsalani, N., Fattahi, H. & Nazarpoor, M. Synthesis and characterization of PVP-functionalized superparamagnetic Fe 3O 4 nanoparticles as an MRI contrast agent. *Express Polym. Lett.* (2010). doi:10.3144/expresspolymlett.2010.42

152. Caravan, P., Ellison, J. J., McMurry, T. J. & Lauffer, R. B. Gadolinium(III) chelates as MRI contrast agents: Structure, dynamics, and applications. *Chem. Rev.* (1999). doi:10.1021/cr980440x

153. Telgmann, L., Sperling, M. & Karst, U. Determination of gadolinium-based MRI contrast agents in biological and environmental samples: A review. *Analytica Chimica Acta* (2013). doi:10.1016/j.aca.2012.12.007

154. Zhang, F. *et al.* Synergistic enhancement of iron oxide nanoparticle and gadolinium for dual-contrast MRI. *Biochem. Biophys. Res. Commun.* (2012). doi:10.1016/j.bbrc.2012.07.168

155. Zhuo, J. & Gullapalli, R. P. AAPM/RSNA physics tutorial for residents: MR artifacts, safety, and quality control. *Radiographics* (2006). doi:10.1148/rg.261055134

156. Yu, E. Y. *et al.* Magnetic Particle Imaging: A Novel in Vivo Imaging Platform for Cancer Detection. *Nano Lett.* (2017). doi:10.1021/acs.nanolett.6b04865

157. Bauer, L. M., Situ, S. F., Griswold, M. A. & Samia, A. C. S. High-performance iron oxide nanoparticles for magnetic particle imaging-guided hyperthermia (hMPI). *Nanoscale* (2016). doi:10.1039/c6nr01877g

158. Kraupner, A. *et al.* Bacterial magnetosomes-nature's powerful contribution to MPI tracer research. *Nanoscale* (2017). doi:10.1039/c7nr01530e

159. Franke, J. *et al.* System Characterization of a Highly Integrated Preclinical Hybrid MPI-MRI Scanner. *IEEE Trans. Med. Imaging* (2016). doi:10.1109/TMI.2016.2542041

160. Salamon, J. *et al.* Magnetic particle / magnetic resonance imaging: In-vitro MPI-guided real time catheter tracking and 4D angioplasty using a road map and blood pool tracer approach. *PLoS One* (2016). doi:10.1371/journal.pone.0156899

161. Kaul, M. G. *et al.* Combined preclinical magnetic particle imaging and magnetic resonance imaging: Initial results in mice. *RoFo Fortschritte auf dem Gebiet der Rontgenstrahlen und der Bildgeb. Verfahren* (2015). doi:10.1055/s-0034-1399344

162. Tay, Z. W. *et al.* Magnetic Particle Imaging-Guided Heating in Vivo Using Gradient Fields for Arbitrary Localization of Magnetic Hyperthermia Therapy. *ACS Nano* (2018).

doi:10.1021/acsnano.8b00893

163.Ferguson, R. M., Minard, K. R., Khandhar, A. P. & Krishnan, K. M. Optimizing magnetite nanoparticles for mass sensitivity in magnetic particle imaging. *Med. Phys.* (2011). doi:10.1118/1.3554646

164.Ferguson, R. M. *et al.* Size-dependent relaxation properties of monodisperse magnetite nanoparticles measured over seven decades of frequency by ac susceptometry. *IEEE Trans. Magn.* (2013). doi:10.1109/TMAG.2013.2239621

165.Goodwill, P. W. *et al.* Ferrohydrodynamic relaxometry for magnetic particle imaging. *Appl. Phys. Lett.* (2011). doi:10.1063/1.3604009

166.Gleich, B. & Weizenecker, J. Tomographic imaging using the nonlinear response of magnetic particles. *Nature* (2005). doi:10.1038/nature03808

167.Eberbeck, D., Wiekhorst, F., Wagner, S. & Trahms, L. How the size distribution of magnetic nanoparticles determines their magnetic particle imaging performance. *Appl. Phys. Lett.* (2011). doi:10.1063/1.3586776

168.Haegele, J. *et al.* Magnetic particle imaging: kinetics of the intravascular signal in vivo. *Int. J. Nanomedicine* (2014). doi:10.2147/IJN.S49976

169.Alphandéry, E., Chebbi, I., Guyot, F. & Durand-Dubief, M. Use of bacterial magnetosomes in the magnetic hyperthermia treatment of tumours: A review. *International Journal of Hyperthermia* (2013). doi:10.3109/02656736.2013.821527

170.Gutiérrez, L. *et al.* Aggregation effects on the magnetic properties of iron oxide colloids. *Nanotechnology* (2019). doi:10.1088/1361-6528/aafbff

171.Hilger, I. & Kaiser, W. A. Iron oxide-based nanostructures for MRI and magnetic hyperthermia. *Nanomedicine* (2012). doi:10.2217/nnm.12.112

172.Rohrer, M., Bauer, H., Mintorovitch, J., Requardt, M. & Weinmann, H. J. Comparison of magnetic properties of MRI contrast media solutions at different magnetic field strengths. *Invest. Radiol.* (2005). doi:10.1097/01.rli.0000184756.66360.d3

173.Xu, F., Cheng, C., Chen, D. X. & Gu, H. Magnetite nanocrystal clusters with ultra-high sensitivity in magnetic resonance imaging. *ChemPhysChem* (2012). doi:10.1002/cphc.201100548

174.Qin, J. *et al.* A high-performance magnetic resonance imaging T2 contrast agent. *Adv. Mater.* (2007). doi:10.1002/adma.200602326

175.Cabral, H., Nishiyama, N. & Kataoka, K. Supramolecular nanodevices: From design validation to theranostic nanomedicine. *Acc. Chem. Res.* (2011). doi:10.1021/ar200094a

176.Vargas-Osorio, Z. *et al.* Novel synthetic routes of large-pore magnetic mesoporous nanocomposites (SBA-15/Fe3O4) as potential multifunctional theranostic nanodevices. *J. Mater. Chem. B* (2017). doi:10.1039/c7tb01963g

177.Patitsa, M. *et al.* Magnetic nanoparticles coated with polyarabic acid demonstrate enhanced drug delivery and imaging properties for cancer theranostic applications. *Sci. Rep.* (2017). doi:10.1038/s41598-017-00836-y

178.Santra, S. *et al.* Gadolinium-encapsulating iron oxide nanoprobe as activatable NMR/MRI contrast agent. *ACS Nano* **6**, 7281–7294 (2012).

179.Liu, N. *et al.* Cubic: Versus hexagonal-effect of host crystallinity on the T 1 shortening behaviour of NaGdF 4 nanoparticles. *Nanoscale* (2019). doi:10.1039/c9nr00241c

180.Dong, L. *et al.* PEGylated GdF_3 :Fe Nanoparticles as Multimodal T_1 / T_2 -Weighted MRI and X-ray CT Imaging Contrast Agents. *ACS Appl. Mater. Interfaces* **9**, 20426–20434 (2017).

181.Shin, T. H. *et al.* T 1 and T 2 dual-mode MRI contrast agent for enhancing accuracy by engineered nanomaterials. *ACS Nano* (2014). doi:10.1021/nn405977t

182.Wang, K., An, L., Tian, Q., Lin, J. & Yang, S. Gadolinium-labelled iron/iron oxide core/shell nanoparticles as T1-T2 contrast agent for magnetic resonance imaging. *RSC Adv.* **8**, 26764–26770 (2018).

183.Yang, M. *et al.* Characterization of Fe3O4/SiO2/Gd2O(CO3)2core/shell/shell nanoparticles as T1 and T2 dual mode MRI contrast agent. *Talanta* **131**, 661–665 (2015).

184.Choi, J. W. & Moon, W. J. Gadolinium deposition in the brain: Current updates. *Korean Journal of*

Radiology (2019). doi:10.3348/kjr.2018.0356

185.Garcia, J., Liu, S. Z. & Louie, A. Y. Biological effects of MRI contrast agents: gadolinium retention, potential mechanisms and a role for phosphorus. *Philosophical Transactions of the Royal Society A: Mathematical, Physical and Engineering Sciences* (2017). doi:10.1098/rsta.2017.0180

186.Esser, L. *et al.* Gadolinium-functionalized nanoparticles for application as magnetic resonance imaging contrast agents via polymerization-induced self-assembly. *Polym. Chem.* **7**, 7325–7337 (2016).

187.Biju, S. *et al.* A Magnetic Chameleon: Biocompatible Lanthanide Fluoride Nanoparticles with Magnetic Field Dependent Tunable Contrast Properties as a Versatile Contrast Agent for Low to Ultrahigh Field MRI and Optical Imaging in Biological Window. *Chem. - A Eur. J.* (2018). doi:10.1002/chem.201800283

188.Gao, Z. *et al.* Small is Smarter: Nano MRI Contrast Agents - Advantages and Recent Achievements. *Small* (2016). doi:10.1002/smll.201502309

189.Yoo, B., Raam, M. S., Rosenblum, R. M. & Pagel, M. D. Enzyme-responsive PARACEST MRI contrast agents: A new biomedical imaging approach for studies of the proteasome. *Contrast Media Mol. Imaging* (2007). doi:10.1002/cmmi.145

190.Shin, T. H. *et al.* T(1) and T(2) dual-mode MRI contrast agent for enhancing accuracy by engineered nanomaterials. *ACS Nano* (2014). doi:10.1021/nn405977t

191.Quarta, A. *et al.* Multilayered Magnetic Nanobeads for the Delivery of Peptides Molecules Triggered by Intracellular Proteases. (2017). doi:10.1021/acsami.7b05709

192.Vandooren, J., Opdenakker, G., Loadman, P. M. & Edwards, D. R. Proteases in cancer drug delivery. *Advanced Drug Delivery Reviews* (2016). doi:10.1016/j.addr.2015.12.020

193.Quarta, A. *et al.* Multilayered Magnetic Nanobeads for the Delivery of Peptides Molecules Triggered by Intracellular Proteases. *ACS Appl. Mater. Interfaces* **9**, 35095–35104 (2017).

194.Quarta, A. *et al.* Multilayered Magnetic Nanobeads for the Delivery of Peptides Molecules Triggered by Intracellular Proteases. *ACS Appl. Mater. Interfaces* (2017). doi:10.1021/acsami.7b05709

195.Coffey, W. T. & Kalmykov, Y. P. Thermal fluctuations of magnetic nanoparticles: Fifty years after

Brown. *Journal of Applied Physics* (2012). doi:10.1063/1.4754272

196. Estelrich, J., Sánchez-Martín, M. J. & Busquets, M. A. Nanoparticles in magnetic resonance imaging: From simple to dual contrast agents. *Int. J. Nanomedicine* (2015). doi:10.2147/IJN.S76501

197. Ni, D., Bu, W., Ehlerding, E. B., Cai, W. & Shi, J. Engineering of inorganic nanoparticles as magnetic resonance imaging contrast agents. *Chem. Soc. Rev.* **46**, 7438–7468 (2017).

198. Hu, F., Joshi, H. M., Dravid, V. P. & Meade, T. J. High-performance nanostructured MR contrast probes. *Nanoscale* (2010). doi:10.1039/c0nr00173b

199. Rohrer, M., Bauer, H., Mintorovitch, J., Requardt, M. & Weinmann, H. J. Comparison of magnetic properties of MRI contrast media solutions at different magnetic field strengths. *Invest. Radiol.* (2005). doi:10.1097/01.rli.0000184756.66360.d3

200. De Leõn-Rodríguez, L. M., Martins, A. F., Pinho, M. C., Rofsky, N. M. & Sherry, A. D. Basic MR relaxation mechanisms and contrast agent design. *J. Magn. Reson. Imaging* (2015). doi:10.1002/jmri.24787

201. Johnson, N. J. J., Oakden, W., Stanisz, G. J., Scott Prosser, R. & Van Veggel, F. C. J. M. Size-tunable, ultrasmall NaGdF4 nanoparticles: Insights into their T1 MRI contrast enhancement. *Chem. Mater.* (2011). doi:10.1021/cm201297x

202. Yang, M. *et al.* Ultra-small and size tunable PVP-NaGdF 4 :Dy nanoparticles with high biocompatibility for multimodal tumor imaging. *RSC Adv.* (2016). doi:10.1039/c6ra18780c

203. Keasberry, N. A. *et al.* Tuning the relaxation rates of dual-mode T1/T2 nanoparticle contrast agents: a study into the ideal system. *Nanoscale* **7**, 16119–16128 (2015).

204. Zhou, Z. *et al.* A synergistically enhanced T 1 -T 2 dual-modal contrast agent. *Adv. Mater.* (2012). doi:10.1002/adma.201203169

Overall Summary of Thesis

In last three years of my PhD, Phd cycle XXXII (2016-2019) in the Department of Nano chemistry at istituto italiano di technologia, under supervision of Dr. Teresa Pellegrino and Prof. Orietta Monticelli (University of Genova) my focus was mainly on developing colloidal stable nanoclusters of various geometries produced from benchmark iron oxide nanocubes, aiming their potential theranostic features; Magnetic hyperthermia (MH), Magnetic resonance imaging (MRI) and Magnetic nanoparticles imaging properties (MRI) as illustrated in Figure 1.

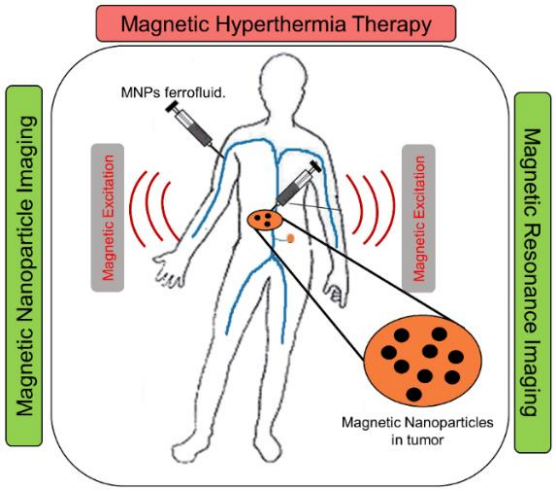

Figure 1. Scheme illustrating over all aim of my thesis.

The iron oxide nanoparticles (IONPs) were approved by U.S food and drug administration for biomedical applications such as for treatment and diagnosis purpose[17,18] because of biocompatibly and nontoxic properties. Since the work performed by *Gilchrist RK* in 1957 to cure lymph nodes cancer,[27] MNPs caught deep scientific interest for MH application due to their characteristic feature of heat dissipation, remotely (temperature between 40-45 °C), upon exposure to alternative magnetic fields (AMF) to thermally ablate the cancerous cells locally[19], rather than interrupting the surrounding healthy tissues.[26] The heat generating efficiency of MNPs can be expressed in the terms of specific absorption rates (SAR), which means the energy absorbed per mass of iron on exposing to the electromagnetic fields, units given as watts per gram (W/g). Indeed, this non-invasive MH was clinically approved in Europe to treat glioblastoma multiforme, an aggressive brain tumour[28] and for other solid tumors as well.[29,30] Despite of its efficiency, MNPs currently in clinical practice have poor heating

performance,[30] under biological limits of AMF, hence need high dose injections to achieve desired therapeutic temperature (42-45°C), which impairs the application of MRI; a common diagnosis for brain tumors.[31] Since last decade, substantial efforts were dedicated to tune the size, shape, crystallinity and composition of MNPs, through several synthetic routes for optimizing their heating performance.[32,33]

For instance, iron oxide nanoparticles (IONPs) with cubic morphologies have stood significantly the best in terms of their SAR values, which were reportedly presenting 10 to 20 times higher SAR than those of spherical IONPs.[54,55] Besides tuning anisotropy of individual magnetic nanocrystals, a strategies of assembling them into a permanent, optimized anisomeric geometries, with colloidal stability, can be implemented to find exceeding the heat properties of same MNPs.[33,73,80–84]

The properties of MNPs profoundly varies under high concentrations due to dipolar coupling, which makes hyperthermia properties to differ in comparison with well-dispersed MNPs.[60–62] However, this heating property vary either positively or negatively based on the orientation of MNPs in the cluster and consequent dipole interaction. For example, MNPs highly concentrated inside the cells, tends to aggregate randomly, shrink their MH efficiency by 70-90 %.[57–59] Similarly, a mesoscale 3D assembly of iron oxide nanocubes have reducing SAR values in comparison to same well dispersed particles due to randomly orientation of cubes.[64] In such dense pack of MNPs, magnetic dipoles interacts very strongly, in return interrupts the relaxation of individual magnetic momentums of the nanocrystals in the cluster, thus demagnetizes and suppresses the heating abilities.[65,66] Instead, if MNPs assembled in 1D-array or linear configuration, due to uniaxial magnetic dipolar coupling, magnetic spin behaves as a single elongated entity,[72] consequently responds quickly to the magnetic field excitations, thus the higher SAR, as it was proven by many experimental and theoretical studies.[70,71]

While several studies have been reported for three-dimensional magnetic beads (3D-MNBs),[33,83,92] only few attempts of producing a 2D-assembly of MNPs have been successful, however some of them were following solid substrate based deposition methods such as the Langmuir-Blodget technique,[93,94] a chemically assisted self-assembly technique,[95] or a magnetic field-induced assembly technique,[96] which are in micrometer size and not suitable for bio applications. Till date, very few studies on colloidal stable 2D assemblies of MNPs are known, one of this kind, is the work of Andreau *et al*.[102] Although this paper has pioneered the work on MNPs arrangements in magnetic hyperthermia, the choice of the

initial particles with poor heat performances was not impressive.[102] In this work, we aim to cluster MNPs into a 2D assembly of mesoscale range, using our benchmark high performing iron oxide nanocubes (IONCs)[103] enwrapped with a bacteria extracted,[105,106] biodegradable and biocompatible aliphatic polyesters, Polyhydroxyalkanoate (PHA) produced by the group of Dr. Ipsita Roy, West Minister Collage London, that is susceptible to biocatalytic cleavage on exposure to enzymes such as esterases and lipases.[107,108] Comparing magnetic heat properties of the 2D assemblies (2D-MNBs) to three dimensional centro-symmetrical assemblies (3D-MNBs) or single iron oxide nanocubes (Single NCs) from same batch of cubes, emphasize that heat losses of 2D-MNBs are advanced than the 3D-MNBs, but worse respect to Single NCs. Such effect of clustering on the SAR can be understood in terms of their varied magnetic dipolar interactions.[122,134] In 2D-MNB, the spatial order of IONCs into the cluster and the constant interparticle distance minimize magnetic dipolar interactions, resulting in SAR values that are closer to that of single IONCs. While in case of 3D-MNBs the IONCs within cluster are randomly oriented and closely packed which causes significant demagnetization effects, that directly reduce the SAR performance.[83,84,138] Remarkably, our 2D-MNBs haven't exhibit any variations in heat performance even after inducing an intentional aggregations. This feature is extremely important because most of the reported nanoclusters exhibited significant shrink in their magnetic losses which drastically caused reduction in magnetic heat performances, if the aggregation increases, thus limiting their application for MH performance in a cellular environment.[58,140] Interestingly, this heat abilities of 2D-MNBs progressively increased when incubated in presence of esterase enzyme at 37°C, whose SAR values were almost doubled after 2 hours of incubation, that was surprisingly higher than Single NCs as extrapolated in Figure 2.i below. Such an increase corresponds due to the fact of disassembling of 2D-MNBs into short chain like clusters of few nanocubes, as a result of the uniaxial magnetic dipolar coupling, behave as an elongated entities with a single and large magnetic momentum, whose magnetic easy axis was expected to respond quickly to magnetic fields. Magnetophoresis studies suggest faster response of 3D and 2D clusters to external magnets (0.3T) than that of single crystals. This ideal feature is crucial for external magnetic field gradient mediated physical accumulation of magnetic materials. We have also performed a complimentary work of assembling core-shell iron oxide nanocubes (Cs-IONCs, less interacting) into Dimer/trimer (short chains), centrosymmetric (BCs) and individual cubes (SCs), by using one specific amphiphilic polymer, poly(styrene-comaleic anhydride), cumene-terminated as templet. Interestingly, by exploiting the amount of polymer to nanoparticle

surface ratio, the Cs-IONCs can be modulated into distinct geometries. Also in this case, short chains like Dimer/trimer composed of few cubes given an pronounced SAR (Figure 2.ii), whose appearance is similar to that of disassembled short chains of 2D-MNBs. In an overview this entire study reveals the significance of particle arrangements and consequent dipolar interaction on their intrinsic properties, consequently on heating performances. To best of our knowledge, this is first example of a nanoplatform, which is having an ability to split into short chainlike assemblies in response to lytic enzymes that with a clear enhancement of the magnetic heat losses.

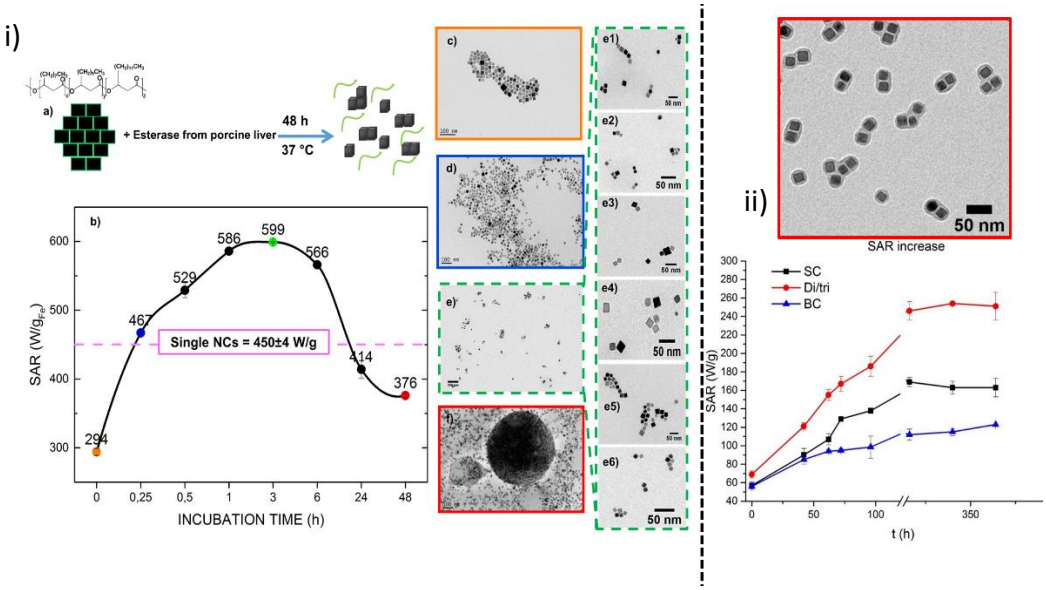

Figure 2.I) a) Panel in left emphasize how SAR of 2D-MNBs progressively increase with incubation time upon exposure to the esterase enzyme, that corresponds to disassembling of 2D-MNBs into the short chain configured structures. ii) The right panel illustrates enhanced SAR of Dimer/trimeric nanoclusters with respect to SCs and BCs, that complementing results of short chains resulted for 2D-MNBs.

The iron oxide nanoparticles (IONPs), despite of their promising performance for MH, were also researched and applied widely as magnetic tracers in high resolution imaging techniques that includes MRI[9,145] and recently emerging MPI imaging[146], with an aim of improving diagnostic accuracy. MRI works on the same principle of nuclear magnetic resonance (NMR).[148] It detects the magnetic moment of water proton (H^1). The relaxation times of proton can be shortened to enhance contrast of tissue by administrating contrasting agents;[8] for instance by using iron oxide nanoparticles (T_2) for dark contrast which induces transverse relaxation[151] or gadolinium based molecules (T_1) for bright signal which induces longitudinal relaxation.[152,153] The efficiency of this colloidal contrast agents (MNPs/Gd) can be estimated in terms of relaxivity rate values, r_1 (longitudinal rate) and r_2 (transverse rate) which is

calculated from the linear slope fitting obtained by inverse of the relaxation time (T_1 or T_2) as function of elemental concentration.[64] Instead, the MPI is a quantitative real time advanced tomography technique whose signal intensity is directly proportional to the concentration of the magnetic tracer, because a receiving coil in the setup directly detects the electronic transition (harmonics) of the magnetic tracer under magnetic excitations.[146,156,157] In fact, unlike the MRI, MPI directly detects the magnetic moments of magnetic tracers located at target site. In comparison to momentum of proton, the IONPs have momentum 8 order of magnitude stronger, therefore consequent detection of magnetization strength can be 22 million times predominant than MRI.[15,158] Hence it's been claimed, with respect to MRI, that MPI was very competitive for its resolution and tracer sensitivity. In addition, this noninvasive technique was operated at the low magnetic excitation fields, that detects signal only from the nanoparticles with no features of background single/interference from diamagnetic biological tissue,[146] thus lowers the chance of artifacts. However, combination of advanced MPI imaging with conventional MRI as a multimodal imaging modality was advantageous to increase the diagnostic accuracy with more anatomical details.[12,159–161] Since this MPI works on the same principle of MH, where MNPs are excited by applying AMF of certain field and frequency, the strategy of exciting same particles for heat generation can be implemented without affecting vital organs as performed elsewhere[157,162] and this method is also termed as magnetic nanoparticles imaging guided hyperthermia or hMPI. Indeed, similar to MH, the signal intensity in MPI depends on relaxation rate of MNPs (Neels or Brownian), in response to AC magnetic fields.[163–165] Since the current science of developing tracers for MPI/hMPI was still in the early stage of research, in this project we will shortly discuss MPI and MRI properties of our nanostructures, the one already with efficient MH properties as discussed above; that are 2D-MNBs prepared from high interacting IONCs and Dimers/trimer, individual cubes and bigger clusters produced from same Cs-IONCs. The 2D-MNBs exhibit poor MPI signal than that of standard Resovist. However, this signal underwent a progressive increase upon incubation with esterase enzyme at 37°C starting from their initial state, which is attributed to the splitting of 2D beads into small chain like configuration (refer to the Figure 3, left panel), similar to the enzyme triggered increase of heat performance, as mentioned above. Moreover, this 2D-MNBs have given a remarkable transverse relaxation rate (r_2), indicative to be an efficient negative contrast agent for MRI, however this value reduced by half upon exposure to lytic enzyme, but still in the decent range of most commercial T_2 MRI contrast agents. On the otherside, among the nanoclusters based on core-

shell IONCs that are single cubes, Dimers/Trimers and centrosymmetric structures, Dimers/Trimers exhibit a very remarkable MPI signal, that even higher than the most adopted standard; the Resovist (refer to the Figure 3, right panel). The signal dominance in short chains like assemblies corresponds to their short uniaxial dipolar coupling. In addition, Dimers/Trimers have given a very significant transverse relaxation rate (r_2) than many other superparamagnetic iron oxide nanoparticles. This kind of nanovectors with multifunctional theranostic features of MRI, MPI and MH are beneficious to improve treatment planning of cancerous tissues with simultaneous image mapping and thermo-therapy.

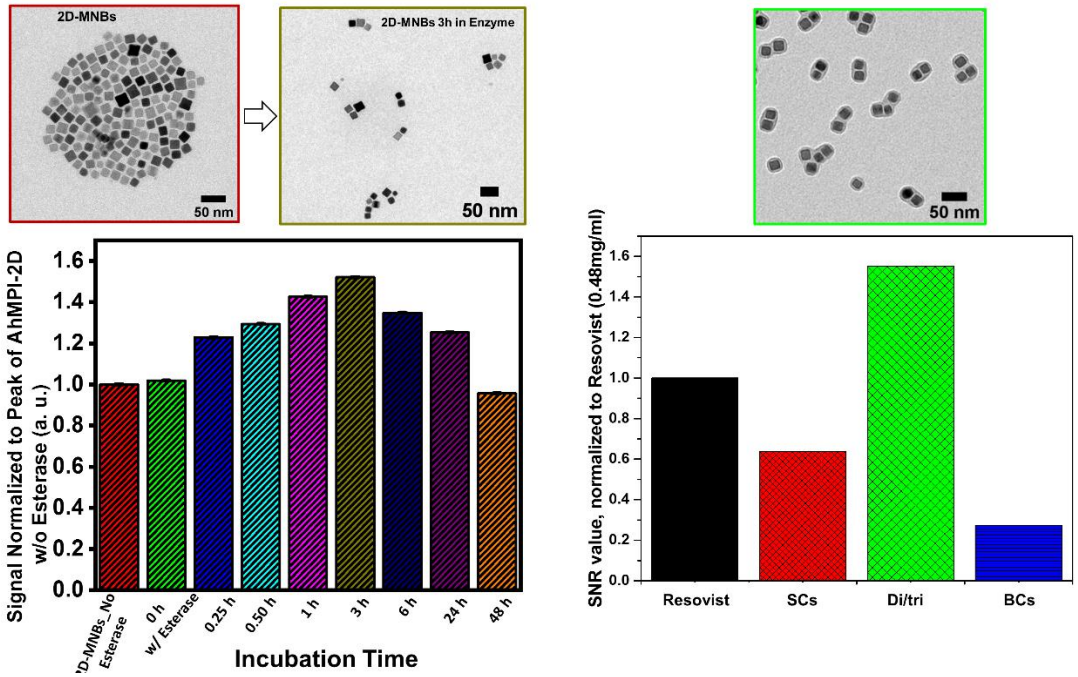

Figure 3. a) Panel in left emphasize how MPI signal of 2D-MNBs progressively increase with incubation time upon exposure to the esterase enzyme, that corresponds to disaasembling of 2D-MNBs into the short chain configured structures. b) The right panel illustrates enhanced MPI signal of Dimer/trimeric nanoclusters with respect to SCs and BCs, that complementing results of short chains resulted for 2D-MNBs.

Despite of the efficiencies of iron oxide nanocubes for MRI, their sole use as T_2 contrasting agent, especially at concentrations of MH associate with few ambiguities.[2] Basically, superparamagnetic compounds like IONCs at high concentration could create huge magnetic susceptibility out of accumulated site at proximities, thus notoriously darkens even the surrounding health tissue, creates confusion in identifying/differentiating normal tissue from the diseased site.[10] For reducing such artifacts, many proposed dual image modalities, like merging T_1 and T_2 properties in single probe that

facilitates in switching between contrasts of our choice.[180–182] For instance yang *et al*., developed such $Fe_3O_4/SiO_2/Gd_2O(CO_3)_2$ core-shell structures with dual contrast abilities (T_1 -T_2 properties).[183] Besides, so far none reported combining hyperthermia as a treatment source in such nanoprobes with artifact filtering T_1-T_2 dual MRI imaging abilities. We initiated a work in constructing a theranostic nanoplatform composed of magnetic IONC as the main and efficient material for MH , a T_2 contrast agent for MRI [83103], and gadolinium-based nanoparticles as a paramagnetic shell for T_1 relaxation. Rather using Gd^{3+} ions in chelate forms, embedding in a rigid matrix such as in inorganic nanoparticles, could be a right strategy of designing, not only for better T_1 performance and increasing circulation time[187] , but also to reduce the toxicity concerns by preventing the free leakage[188]. It is important to note, merging of both the particles in an unorganized way, suppose, if both the modalities are in very close contact, it is much likely to cause the quenching of T_1 abilities of Gd^{3+} ions, because of magnetic susceptibility coming from IONCs.[190] Therefore, as a novel route, we adopted our recently published layer-by-layer (LbL) approach[191] to synthesize composite structures of IONCs embedded in a polymeric bead as core (MNBs), on which negatively charged, water soluble polyacrylic acid (PAA) coated $NaGdF_4$ NPs (PAA-$NaGdF_4$ NPs) were packed using intracellular protease[192] degradable polymer spacers Poly-L-arginine hydrochloride (PARG), through electrostatic interaction: Intended structure illustrated in Figure 4 below.

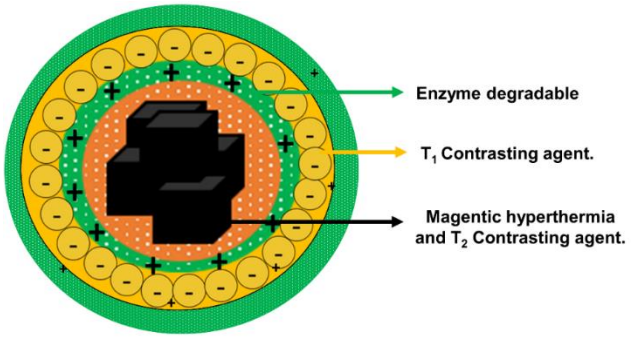

Figure 4. The scheme of multifunctional nanoprobe with theranostic properties, prepared in this project.

For this purpose, we synthesize composite structures starting from IONCs embedded in a polymeric bead with a surface negative charge (MNB) and decorated with PAA coated $NaGdF_4$ NPs, placed in between enzyme-degradable polymer spacers. Our hybrid structure achieved desired heating abilities under alternative magnetic field of biological relevance; H= 300 kHz and f =16 KA/m, where it achieved

a temperature difference (ΔT°) of almost 13.93°C in a span of 1 hour. In spite of prominent T_2 properties coming from magnetic core (MNBs), the degradation of PARG and consequent detaching of $NaGdF_4$ NPs from the surface of the MNBs upon exposure to enzyme, in return increased corresponding T_1 signal with incubation time; from 8.5 $mM^{-1}s^{-1}$ to 11.9 $mM^{-1}s^{-1}$ due to improved water accessibility to $NaGdF_4$ NPs. Evidence in improving T_1 relaxation in response to enzyme was confirmed by the reduction of relaxation ratios from 50 mM^{-1} s^{-1} to 17 mM^{-1} s^{-1}.

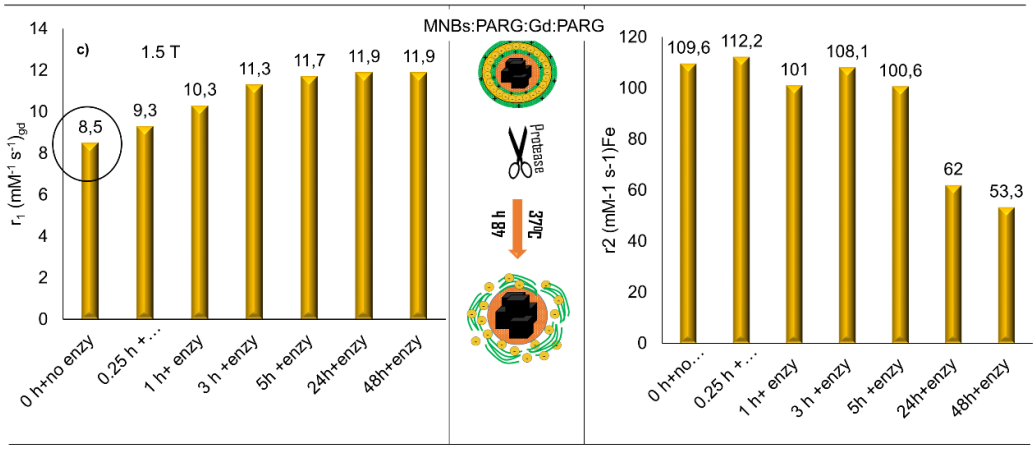

Figure 5. The longitudinal relaxation (r_1) profile of MNBs:PARG:Gd:PARG plotted based on the gadolinium concentrations. The plot extrapolates the evolution r1 rates over a period of 48 h, after exposing to the protease enzyme under biological temperature of 37 °C. b) The transverse relaxation rate (r1) of MNBs:PARG:Gd:PARG plotted based on the iron concentrations. Chart represent the r2 relaxation rate of hybrid structure, exposed to the protease enzyme incubated at 37 °C as function of the time.

The integration of diagnostic tools to benchmark therapeutic probes could be a smart approach that enables to track the nanoparticle accumulation through artifact free diagnosis and improve the heat efficiency of the magnetic hyperthermia treatment at the tumor sites.

Appendix: List of Publications, Conference Communications and Awards

Scientific Publications

Avugadda, S. K. et al. Esterase-Cleavable 2D Assemblies of Magnetic Iron Oxide Nanocubes: Exploiting Enzymatic Polymer Disassembling To Improve Magnetic Hyperthermia Heat Losses. Chem. Mater. (2019). doi:10.1021/acs.chemmater.9b00728.

Dina Niculaes, Aidin Lak, George C. Anyfantis, Sergio Marras, Oliver Laslett, Sahitya K. Avugadda, Marco Cassani, David Serantes , Ondrej Hovorka, Roy Chantrell, and Teresa Pellegrino Asymmetric Assembling of Iron Oxide Nanocubes for Improving Magnetic Hyperthermia Performance. ACS Nano 11, 12121–12133 (2017).

Materia, M. E., Leal, M. P., Scotto, M., Balakrishnan, P. B., Avugadda, S. K., Garc, L., … Pellegrino, T. (2017). Multifunctional Magnetic and Upconverting Nanobeads as Dual 2 Modal Imaging Tools 1. https://doi.org/10.1021/acs.bioconjchem.7b00432.

Conferences communications

Oral: Sahitya K. Avugadda, Dina Niculaes, Maria Elena Materia, Aidin Lak , Francisco J. Teran, Ipsita Roy and Teresa Pellegrino "Assemblies of highly efficient iron oxide nanocubes for magnetic (fluid) hyperthermia to treat tumors". International Conference On Nanomedicine And Nanobiotechnology – ICONAN 2019, Munich, October 16th-18th, Germany.

Poster: Sahitya Kumar Avugadda, Niculaes, D., Lak, A. Controlled clustering of iron oxide nanocubes for magnetic fluid hyperthermia treatment. "Abstract Book of "16th International Conference of Nanosciences and Nanotechnologies (ICNN19) and 13th International summer school of nanoscience & Nanotechnologies 2019, Thessaloniki, Greece.

Poster: Barbara Salis, Sahitya Kumar Avugadda, Amira El Merhie, Teresa Pellegrino, Alberto Diaspro, Silvia Dante. "Interaction of nanoparticles with cellular and model membranes: influence of surface charge, size and membrane potential". International Conference on Nanomedicine and Nanobiotechnology 2018, Sept 26-28, Rome, Italy.

Awards & Honors

"YOUNG RESEARCHER AWARD" for best poster presentation at "13th International summer school of nanoscience & Nanotechnologies 2019", Thessaloniki Greece.

Research Period Abroad

In framework of European Compass project, I have spent 3 months period (15/06/2018 to 15/09/2018) abroad at Molecular foundry, Lawrence Berkley National laboratory, USA, on the project named. "Automatized synthesis of magnetic mixed ferrites nanocubes and anisotropic assemblies of nanocubes for magnetic hyperthermia."

Acknowledgements

First and foremost, I would thank my supervisor Dr.Teresa Pellegrino for her advice, guidance and continuous motivation during my PhD life. I would also thank, our nanochemistry director Dr. Liberato Manna for hosting me to carry out my acivities in laboratory. Likewise, I would like to thank co-supervisor Prof. Orietta Monticelli; from university of Genova. I profoundly express my great gratitude to our lab technicians; Simone Nitti, Giammarino Pugliese, Filippo Drago, Gabriele la Rosa and at the same time I would like to acknowledge my colleagues from department of NABM for their collaboration, thoughtful criticism and motivation in enhancing my research. A special appreciation to Maria Elena Materia and Marco Cassai for suggestion to resolve some of my scientific issues in during lab activities. Also, I would love to extend my wholehearted gratitude to my parents Appala Naidu Avugadda and Satyavathi Avugadda for believing in me and my abilities and encouraged me to fulfill my doctorate goal. This acknowledgment is incomplete without thanking my Brother-in-law and Sister; Suman Naidu Potala and Dr. A.B.M Sirisha, who always stood behind me as hidden motivators and continuesly loading confidence in me and I truly appreciate their unconditional support. In one single sentence I would not be in this PhD path without their existence. My indebtedness goes to my dear and lovely wife, Harshita Kurasa for her unconditional love and care. I would appreciate her patience in proof reading my thesis. I would also thank Prof. Andrea Massimo Atrei, Prof. Agnese Magnani and Prof. Allesandro Donati from university of Siena, Italy who directed me to pursue my career in research.

Curriculum

Sahitya kumar Avugadda was born in a very remote rural village, Marepalli, in state of Andhrapradeh India, on August 28 1989. He was brought up by attending the primary school, Kairali English medium residential high school upto his tenth grade. Later, he moved to near by city visakhaptnam for his intermediate board studies (Sri Chaitanya junior collage). In the period of 2006-2009, he obtained his Bachelor degree from Andhra Univeristy, Visakhapatnam in the field of Biotechnology, Biochemistry and Chemistry. From period of 2009 to 2012 her persued his Masters in Cinical Research Management from Prist university. Later he spent his time working in well reputated company Merck Sereno, as Clinical Research Associate in the clinical trail department for 1.5 years. With a deep interest in research, he moved to Italy in 2014 for Advanced Masters in Chemistry and awarded with degree in 2016, as Master in Chemistry from University of Siena, Italy. In Novermeber 2016, he started his PhD under supervision of Dr.Teresa Pellegrino and co-supervisor Prof. Orietta Monticelli (University of Genova), at istituto italiano di technologia, Genova Italy under affliation to University of Genova, working mainly on Assemblies of inorganic nanoparticles for theranostic application.